THE UNIVERSITY OF NEWCASTLE

www.newcastle.edu.au

‘EXPERIMENTAL DETERMINATION OF DEFORMATION AND CUTTING ENERGY FACTOR FOR WEAR PREDICTION OF PNEUMATIC CONVEYING PIPELINE’

MASTER THESIS OF:	KIM SUN PANG
	(CALLAGHAN CAMPUS,
	NEWCASTLE 2308)
SUPERVISORS:	Professor Dr. Mark G. Jones, Dr. Williams Kenneth, Dr. Ahmed Cenna
Conducted at:	The University of Newcastle, Australia
	Centre of Bulk Solids and Particulate Technologies

Newcastle, 19.03.2011

Preface

This dissertation is submitted for the degree of Master of Philosophy in Material Wear Research at the University of Newcastle. The research described herein was conducted under the supervision of Prof. Mark Jones, Dr. K.Williams, and Dr. A. Cenna, in the Department of Mechanical Engineering, Newcastle, between March 2008 and June 2010. Except where acknowledgement and reference is made to previous work, this work is, to the best of my knowledge, original. Neither this, nor any substantially similar dissertation has been, or is being, submitted for any other degree, diploma or other qualification at any other university.

Kim Sun Pang

CERTIFICATE

I hereby certify that this work embodied in this master thesis has been done at the Faculty of Engineering and Built Environment at the University of Newcastle, Australia 2010. This work has been independently developed and has not been submitted for a higher degree at any other University or Institute.

Date Signed

Acknowledgements

I would like to extend my gratitude to all people who have provided me with assistance in my effort towards achieving my goal for this research. First of all, I gratefully acknowledge my academic supervisors, Professor Mark Jones, Dr. W. Kenneth and Dr. A. Cenna for their guidance, inspiration and support as well as for giving the opportunity to utilise the laboratory facilities in the department of Mechanical Engineering at the University of Newcastle.

I gratefully acknowledge the financial support from the CRC for Integrated Engineering Asset Management (CIEAM) for this research.

My special thanks to the laboratory technicians of TUNRA Bulk Solids for their help and assistance with my test equipment and other necessary setups. Appreciation for help is extended to David Phelan of EM/W-ray unit at the University of Newcastle for examining the erosion surfaces using SEM.

Abstract

The erosion behaviors of aluminum and mild steel at different impact angles and velocities have been studied using a micro-sandblaster. The wear rates for different parameters and as well as surface characteristics have been the subject of this research.

A mathematical model has been used for analyzing the experimental wear rates together with the dominant wear mechanisms present on the surface. The model has been developed based on the particle kinetic energy and the energy required removing a unit amount of material from the surface. These energy factors were determined from the experimental results based on the understanding of the cutting and deformation mechanisms of ductile materials.

Optical microscopes as well as scanning electron microscope (SEM) have been used to study the surface characteristics and wear mechanism. The characteristics of the eroded surface and the wear mechanisms have been discussed in detail to relate the rate of wear on the surface. It was found that erosion at an incident angle of 30^{o} and a velocity of 60 m/s is dominated by the cutting mechanism while at 30 m/s at the same impact angle, the wear rate is dominated by the deformation mechanism.

The present work emphasizes the effect of erodent variables on the erosion performance of ductile materials. The steady state mass loss curve has been plotted in order to study the variation of wear rate as a function of impact angle. Wear rates for different angles of impact and particle impact velocities have been plotted for a better understanding on the wear behavior of ductile materials for two different erodent particles.

A technique for determining energy required to remove a unit mass of material is presented in this study. The behavior of the unit energy with respect to the impact velocity and impact angle in an erosion process is also discussed.

It appears that the absorbed energy increases with increasing particle size demonstrated by the increased wear rates. It is suggested that the absorbed energy increases with increasing particle size due to its inertial stress. It was also demonstrated that the angular particle, ilmenite, can transfer more energy to the surface due to its shape (higher angularity).

Finally the energy factors determined in the experimental program have been applied into a predictive model for determining service life of a pneumatic conveying pipeline. The difference between the predicted and measured data also been discussed.

CONTENTS

Preface……			ii
Certificate……..			iii
Acknowledgements..……..			iv
Abstract……			v
TABLE OF CONTENT……..			vii
LIST OF TABLES……			xi
LIST OF FIGURES……..			xii
NOMENCLATURE AND ABBREVATIONS AND SYMBOLS……			xvi
CHAPTER	1	THEORETICAL BACKGROUND OF WEAR.	1
	1.1	WEAR IN PNEUMATIC CONVEYING PIPELINE……..	1
	1.2	AIM OF THIS STUDY…….	5
	1.3	THESIS OVERVIEW……...	7
CHAPTER	2	LITERATURE REVIEW……..	8
	2.1	INTRODUCTION…….	8
	2.2	WEAR…….	8
	2.3	CLASSIFICATION OF WEAR…….	10
	2.3.1	EROSIVE WEAR……..	10
	2.3.2	ABRASIVE WEAR……	13
	2.3.3	ABRASIVE WEAR IN BRITTLE MATERIALS……...	15
	2.4	FORMATION OF RIPPLE…….	16
	2.5	PARTICLE CHARACTERISTICS…….	18

	2.6	EXPERIMENTAL WORK……	23
	2.7	SURFACE MORPHOLOGY…….	29
	2.8	MODELING……	33
	2.8.1	MICRO-MACHINING MODEL…….	33
	2.8.2	DEFORMATION MODEL……..	36
	2.8.3	CUTTING MODEL.....	38
	2.8.4	MODEL FOR PARTICLE DISTRIBUTION IN AIR STREAM……..	40
	2.8.5	FORMATION OF CRATERS DUE TO NORMAL IMPACT…….	43
	2.9	SURFACE BEHAVIOUR RELATED TO EROSION PROCESS……..	47
	2.10	MODELING FOR PRESENT STUDY……..	48
	2.11	ENERGY FACTOR…….	49
	2.11.1	DEFORMATION ENERGY FACTOR……..	50
	2.11.2	CUTTING ENERGY FACTOR……..	50
CHAPTER	3	EXPERIMENTAL METHODOLOGY……..	51
	3.1	INTRODUCTION……	51
	3.2	EXPERIMENTAL SETUP……..	51
	3.3	TEST MATERIALS AND ERODENT…….....	54
	3.4	MEASUREMENT OF THE PARTICLE VELOCITY IN GAS STREAM……...	55
	3.4.1	EXPERIMENTAL METHOD FOR MEASURING PARTICLE VELOCITY…….	55
	3.4.2	ANALYSIS OF THE ERODENT PARTICLES.	59
	3.5	TEST PROCEDURE……	63

	3.6	DETERMINE THE STEADY STATE EROSION RATE…….	64
CHAPTER	4	EXPERIMENTAL RESULT……	67
	4.1	INTRODUCTION……	67
	4.2	DETERMINATION OF STEADY STATE WEAR RATES OF DUCTILE MATERIALS…	67
	4.3	EFFECT OF IMPACT ANGLE ON EROSION RATE……	74
	4.4	OBSERVATION MORPHOLOGY OF ERODED SURFACE……...	76
	4.4.1	ALUMINA SURFACES ERODED BY ALUMINA AND ILMENITE…….	77
	4.4.2	MILD STEEL SURFACES ERODED BY ALUMINA AND ILMENITE…….	81
	4.5	ANALYSIS OF SURFACES MICROGRAPHS OF ERODED SURFACES……..	85
	4.6	CONCLUSION……	99
CHAPTER	5	ENERGY FACTOR…….	100
	5.1	INTRODUCTION……	100
	5.2	ENERGY FACTOR…….	100
	5.3	CALCULATUIN OF ENERGY FACTORS FOR ALUMINIUM AND MILD STEEL..……..…	103
	5.3.1	DEFORMATION ENERGY FACTOR……..	104
	5.3.2	CUTTING ENERGY FACTOR…….…….	106
	5.4	EFFECT OF IMPACT ANGLE ON ENERGY FACTORS..……	107
	5.5	CALCULATION STEADY STATE EROSION RATE……	110
	5.6	METHOD FOR DETERMINATION OF CUTTING ENERGY FACTOR FOR WEAR	111

		MODEL……	
	5.7	APPLICATION OF THE ENERGY FACTORS IN PREDICTIVE MODELS……	113
	5.8	PROCESSES IN EROSION ENERGY FACTOR……..……...	115
	5.8.1	EROSIVE ENERGY OF PARTICLE…….	116
	5.9	CONCLUSION……	119
CHAPTER	6	CONCLUSION AND FUTURE WORK…….	120
	6.1	CONCLUSION…….	120
	6.2	THE FUTURE WORK……	122
REFERENCES…….			124

LIST OF TABLES

TABLE NUMBER		PAGE NUMBER
2-1	MATERIAL TESTED BY TILLY	26
3-1	EROSION CONDITION OF EROSION EXPERIMENT	51
3-2	MECHANICAL PROPERTIES AND EROSION PARAMETER	63

LIST OF FIGURES

FIGURE NUMBER		PAGE NUMBER
1-1	The mechanical arrangement from a gas-solid two phase flowing pipeline. (From CIEAM report, 2006).	2
1-2	Illustration of (a) erosion, (b) two-body abrasion & (c) three-body abrasion.	3
1-3	Schematic of sections through impact craters, the impact direction was from left to right. (a) Ploughing deformation by a sphere; (b) Type I cutting by an angular particle, rotating forwards during impact; (c) Type II cutting by an angular particle, rotating backwards during impact.	4
2-1	The damage eroded by the transporting particles.	9
2-2	The wear produced by abrasive and erosive wear at the same time	9
2-3	The wear caused by the 400 grit silicon carbide abrasive paper on the surface of AISI 1020.	10
2-4	Proposed sequence of erosion of a copper-plated steel specimen.	11
2-5	Section through impact craters formed by hard particles on a ductile metal, showing typical shapes. The impact direction was from left to right. (a) Ploughing deformation by a sphere; (b) Type I cutting by an angular particle, rotating forwards during impact; (c) Type II cutting by an angular particle, rotating backwards during impact.	12
2-6	SEM picture of 0.8% C steel worn surface	14
2-7	Diagram of crack formation in a brittle material by a quasi-static indenter	15
2-8	(a) Shows the weight loss of pure Al and Al-12Si vs. particle weight of 406 μm Al_2O_3 erodent particles at 30^o, travelling at 70 m/s. (b) Shows the eroded surface after: (a) 8g; (b) 16g; (c) 32g of particle[16].	17
2-9	(a) Weight loss of pure aluminium vs. accumulated weight (g) for glass beads impacting at 30^o. (b) Surface ripples after impacting (a) 5g; (b) 15g; (c) 30g of particle[16].	18
2-10	Angularity of abrasive; gb=glass bead ss=silica sand g=Garnet q=Quartz sic=silicon carbide al=alumina[18].	19
2-11	SEM micrograph of embedded debris of abrasive in worn brass (a) Glass beads (b) Silica sand (c) Garnet (d) Quartz and (e) Silicon carbide[18].	20
2-12	Average wear rate of (a) Mild steel (b) High Cr white cast iron plate under the influence of angularity of abrasive in slurry[18].	21
2-13	Morrison and Scattergood [19] showed the determination of erosion rate. From left to right, 45^o, 60^o, 90^o.	24
2-14	The erosion rate of 304 stainless steel at different impact angle, β, by alumina at particle velocity of 100 m/s[19].	25
2-15	Effect of particle size on erosion rate of 304 stainless steel at 100 m/s for angles of 30^o to 90^o from top to bottom [19].	26

2-16	(a) Mass loss of aluminum at 90 degree and 40 degree of impact angle for different impinged mass; (b) Mass loss of type 66 Nylon, carbon reinforced nylon and Polypropylene at 90 degree [21].	27
2-17	Variation of erosion rate with increasing temperature for different surface materials as noted on the graph [21].	28
2-18	Erosion rate of 1020 steel as a function of Vickers hardness [22].	29
2-19	Surface eroded by (a) Sand (SiO) Er=3.0 x 10^{-4} gg^{-1} (b) alumina Er=2.6 x 10^{-4} gg^{-1} (c) silicon carbide Er=3.3 x 10^{-4} gg^{-1} at 80 m/s; Er = erosion rate [22].	30
2-20	Particle characteristics before and after impact of 180-250 μm alumina (a) Before impact (b) After impact at 30^{o} on AISI 1020 steel V=80 m/s (c) After impact at 90^{o} on AISI 1020 steel; V=80 m/s [22].	31
2-21	Particle characteristics before and after impact of 180-250 μm silicon carbide (a) Before impact (b) After impact at 30^{o} on AISI 1020 steel V=80 m/s (c) After impact at 90^{o} on AISI 1020 steel; V=80 m/s [22].	31
2-22	Erosion characteristics of AISI steel eroded by (a) Apatite particle (180um) and (b) Alumina particle (250um) at V=80m/s, $\alpha=90^{o}$ and $T=25^{o}C$ [22].	32
2-23	Idealized picture of abrasive particle striking a surface and removing material. Initial velocity of the particle's centre of gravity makes an angle, α, with the surface[23].	33
2-24	Predicted and experimental rate of volume removal with angle for different ductile materials. The data point: square – SAE 1020 steel, triangle – copper, circle – aluminum [23].	35
3-1	Photograph of the micro-sandblaster model "MV-2 SWAM-BLASTER" from Crystal Mark, Inc.	52
3-2	The schematic diagram of the solid particle erosion testing equipment (not to scale).	53
3-3	Arrangement for measuring the particle velocity in gas stream.	55
3-4	Schematic of double disc method for measuring particle impact velocity.	57
3-5	The Disc chamber for measurement of particle velocity in a gas stream.	58
3-6	The relationship between the compressed air pressure and impact velocity of solid particles at a distance of 23 mm from exit of accelerating nozzle within the mass flow rate range of 0.1 and 0.2 gm./sec.	59
3-7	SEM observation of size and shape of alumina (a) x100 (b) x1600; of Ilmenite (c) x100 (d) x1600.	61
3-8	The measured size distribution of particles, tested by Malvern Mastersizer wet laser particle analyzer, used in the erosion test (a) Alumina and (b) Ilmenite.	62
3-9	Schematic of the particle impacts arrangement (a) Normal impact (b) Oblique impacts.	64
4-1	Variation of mass loss with time and impinged mass of alumina with 60 m/s for aluminum under 90^{o} impact. (a) Mass loss variation with time (sec) and (b) Mass loss variation with particle	68

	mass.	
4-2	Variation of mass loss mild steel impacted by impinged at 60 m/s at 90^o (a) Variation with time, (b) Variation with mass of erodent.	69
4-3	Steady state erosion rate of (a) Aluminum and (b) Mild steel	70
4-4	(a) Erosion-time curve for aluminum impinged by ilmenite with 60 m/s at 90^o, (b) Variation of mass loss with mass of ilmenite with 60 m/s for aluminum under 90^o impact.	71
4-5	(a) Erosion-time curve for mild steel impacted by ilmenite, (b) Variation of mass loss with mass of ilmenite.	72
4-6	Steady state erosion for (a) Aluminum (b) Mild steel at different impact velocity of ilmenite	73
4-7	Variation of steady state erosion rate for (a) Aluminum, (b) Mild steel impinged by solid particle with 60 m/s at different impact angle.	75
4-8	Steady state erosion rate for (a) Aluminum, and (b) Mild steel after impinged by solid particles with 50 m/s at different angles.	75
4-9	Steady state erosion rate for (a) Aluminium, and (b) Mild steel after impinged by solid particles with 30 m/s at different angles.	76
4-10	Aluminium eroded by alumina with 30 m/s at (a) 90^o, Er = 6.28×10^{-07} kg/kg (b) 45^o, Er = 1.67×10^{-06} kg/kg (c) 30^o, Er = 5.3×10^{-06} kg/kg, with 60 m/s at (d) 90^o, Er = 3.4×10^{-06} kg/kg (e) 45^o, Er = 1.41×10^{-05} kg/kg (f) 30^o, Er = 3.36×10^{-05} kg/kg ; Symbol: Er, steady state erosion rate.	78
4-11	Surfaces of aluminium eroded by ilmenite particles with 30 m/s at (a) 90^o, Er=1.56×10^{-05} kg/kg (b) 45^o, Er= 2.38×10^{-05} kg/kg (c) 30^o Er=3.18×10^{-05} kg/kg, and at 60 m/s at (d) 90^o, Er=4.6×10^{-05} kg/kg (e) 45^o, Er=6.5×10^{-05} kg/kg; (f)30^o Er=1.11×10^{-04} kg/kg; Symbol: Er, steady state erosion rate.	80
4-12	Surfaces of mild steel eroded by alumina particles with 30 m/s at (a) 90^o, Er=2.8×10^{-07} kg/kg (b) 45^o, Er=6.02×10^{-07} kg/kg (c) 30^o Er=2.04×10^{-06} kg/kg; with 60 m/s at (d) 90^o, Er=1.6×10^{-06} kg/kg; (e) 45^o, Er=5.75×10^{-06} kg/kg (f)30^o Er=1.79×10^{-05} kg/kg.; Symbol: Er, steady state erosion rate.	82
4-13	Comparison between surfaces of mild steel eroded by ilmenite particles with 30 m/s at (a) 90^o, Er=1.1×10^{-5} kg/kg (b) 45^o, Er= 2.64×10^{-5} kg/kg (c) 30^o, Er=3.6×10^{-5} kg/kg, and with 60 m/s at (d) 90^o, Er=3.89×10^{-5} kg/kg;; (e) 45^o, Er=6.37×10^{-5} kg/kg (f)30^o Er=1.08×10^{-04} kg/kg.; Symbol: Er, steady state erosion rate.	83
4-14	Morphology at centre of eroded surface of aluminium impinged at 90 degree by alumina at magnification of (a) x100 (b) x4000; by ilmenite at magnification of (c) x100 (d) x4000.	86
4-15	Morphology of centre of eroded surface of mild steel impinged at 90^o; by alumina at magnification of (a) x100 (b) x4000; by ilmenite at magnification of (c) x100 (b) x4000.	88
4-16	Centre Morphology of aluminium eroded surface impinged at 30^o ; by alumina at magnification of (a) x100 (b) x4000; by ilmenite at magnification of (c) x100 (d) x4000.	90
4-17	Centre Morphology of eroded mild steel surface impinged at 30^o	91

	;by alumina at magnification of (a) x100 (b) x4000; by ilmenite at magnification of (c) x100 (d) x4000;	
4-18	Material removal mechanisms in ductile materials in oblique angle (30^0 cutting angle, 30 m/s on mild steel, ilmenite particle flow from top to bottom).	93
4-19	Aluminium and mild steel surfaces eroded by ilmenite at oblique angle with magnification of (a) Aluminium surface x4000 (b) Mild steel surface at x4000 (c) Aluminium surface at x1000.	94
4-20	(a) Eroded surface of aluminium impacted by alumina at an angle of 90^o with an impact velocity of 30 m/s. (b) Eroded surface of mild steel impacted by alumina at an angle of 90^o with impact velocity of 30 m/s.	96
4-21	SEM images of eroded surface impacted by ilmenite at normal incidence and 30 m/s particle velocity (a) Aluminium (b) Mild steel.	97
5-1	Deformation energy factor for (a) Aluminum (b) Mild steel.	105
5-2	Cutting energy factor at different velocity for (a) Aluminum and (b) Mild steel.	106
5-3	Energy absorption of aluminium due to different impact angle of (a) Alumina (b) Ilmenite.	108
5-4	Energy absorption of mild steel due to different impact angle of (a) Alumina (b) Ilmenite.	109
5-5	Steady erosion rate was calculated from determined energy factor above for (a) Aluminium (b) Mild steel.	110
5-6	Calculated erosion rate at different angle energy factor for (a) Aluminium (b) Mild steel.	111
5-7	Determined erosion rate from estimated energy factor for (a) Aluminium (b) Mild steel after eroded by alumina.	112
5-8	Determined erosion rate from estimated energy factor for (a) Aluminium (b) Mild steel eroded by ilmenite.	113
5-9	(a) Rate of thickness loss and cumulative thickness loss from the bend wear (b) Incremental thickness loss and cumulative thickness loss from the bend compared with model output.	114
5-10	Deformation energy factor for different particles and size from literature data [45, 87, 22, 2323] and present experimental data of (a) Aluminium, and (b) Mild steel.	117
5-11	Cutting energy factor of 30 degree for (a) Aluminium [4, 86] (b) Mild steel.	118

NOMENCLATURE AND ABBREVATIONS AND SYMBOLS

E_{kin}	kinetic energy of single solid particle at an average velocity in a gas-solid particle stream	kg-m^2/s^2
m	Mass of a solid particle	kg
v	Average velocity of solid particles	m/s
Q_{rel}	Dimensionless Relative volume of material removed	-
α	Impact angle of single solid particle	degree
k	Dimensionless constant ratio of vertical component of particle face to horizontal component	-
p	Constant plastic flow stress	kg/cm^2
ψ	Dimensionless ratio of depth of contact to depth of cut	-
Q_p	The amount of energy required for the formation of permanent indentation	gfcm
Q	The initial kinetic energy of particle	gfcm
Q_e	The elastic deformation energy	gfcm
K	Vertical component of impact velocity at which elastic limit is reached	cm/s
W_D	Unit Mass loss from surface material	kg
M	Cumulative mass of impacting solid particles	kg
V	Average impact velocity of solid particles	m/s
ε	Deformation energy factor	J/mm^3
W_{c1}	Unit volume of material removed when residual horizontal component of velocity as leaving surface is not zero	cm^3

W_{c2}	Unit volume of material removed when residual horizontal component of velocity as leaving surface is zero	cm^3
$V_{\|}$	Initial particle velocity component horizontal to the surface	cm/sec
$v_{\|}$	Particle velocity component horizontal to the surface	cm/sec
C	Material and mechanical properties of erodent constant	$cm^{3/2}sec^{1/2}gf^{-1}$
ø	Cutting energy factor	$gfcm/mm^3$
K_1	Surface restore elastic energy constant as particle leaving	$(cm/sec)^{1/2}$
r	Radius of eroded area	mm
h	Standoff distance	mm
β	Dimensionless Focus coefficient	-
Q_{crit}	Mass of impinged particles per unit area	g/mm^2
L	Average distance between particles	mm
U	Mean velocity of particles	m/s
r_n	Radius of nozzle	mm
Q_o	Mass flow rate	g/min
d	Density of solid particle	$gfsec^2/cm^4$
y_{el}	Maximum elastic limit load	gf/cm^2
q_1	Dimensionless Poisson's ratio of sphere	-
q_2	Dimensionless Poisson's ratio of flat body	-
E_1	Young's modulus of sphere	gf/cm^2
E_2	Young's modulus of flat body	gf/cm^2
E	Dimensionless overall steady state erosion rate	kg/kg
a	Erosion constant	-
v_o	Incident impact velocity	m/s

γ	Dimensionless Velocity index	-
p_H	Dynamic hardness of crater	$kgfmm^{-2}$
l_c	Depth of crater	mm
r_p	Radius of crater	mm
d_c	Diameter of crater	mm
m_e	Mass loss of material eroded	mg
b	Constant	-
β_c	Constant	-
N_i	Number of impact	-
N_o	Threshold number of impact	-
E	Steady state erosion rate	gm/mg
α_r	Contact radius	mm
p_d	Dynamic contact pressure during the loading	GPa
D_p	Diameter of particle	μm
v_p	Residual horizontal component velocity of solid particle	m/s
R	Radial distance of the marks on the disc B	m
ω	Rotation rate of disc B	rev/sec
L	Two disc separating distance	m
S	Linear distance between two marks	m
E_{Def}	Deformation Steady state erosion rate	kg/kg
E_{cut}	Cutting steady state erosion rate	kg/kg
SPQ	Spike parameter–quadratic fit	-

Chapter 1

THEORETICAL BACKGROUND OF WEAR

1.1 Wear in Pneumatic Conveying Pipeline

The application of high pressure gas to convey dry fine powder in a pipeline has interested conveying designers for a long period. The ability of conveying dry powders under the driving force of an expanding air stream provides the powders with accelerating velocity of transportation. One of the first pneumatic conveying systems was installed in England at the end of 19^{th} century and made use of the principles of vacuum for transportation of carriages for a railway tunnel. Later, 100 tonne per hour air vacuum conveyors were installed for unloading grain from ships. Pneumatic conveying has been adopted for transportation of minerals in the mining industries. The advantage of transportation of powder using pneumatic conveying pipeline is to prevent contaminating working environment. Other advantages of pneumatic conveying are their flexible routing and automation of the total system.

The principle of gas-particle-laden flow is that the solid particles under the drag force of the fluid medium flow along the profile of fluid stream. For pneumatic conveying pipeline, the conveying fluid is air which is usually inert to the conveying powder. The accelerated air flow provides the driving force on the solid particles and causes it to flow along the route of pipeline to reach destination.

Pneumatic conveying pipelines also have disadvantages. The common problem in a pneumatic conveying pipeline is the wear due to the impingement of solid particles on

the pipe wall as the conveying powder changes direction due to the routing of the pipeline.

The damage due to solid particle impingement against the pipeline wall usually occurs at bends. Figure 1-1 shows the visualization bend on an experimental pipeline to observe the flow characteristics in a bend. The erosive and abrasive nature of conveying powder causes different types of wear along pipeline, such as erosive wear and abrasive wear.

Figure 1-1: The mechanical arrangement from a gas-solid two phase flowing pipeline. (From CIEAM report, 2006) [1].

The erosive and abrasive wear mechanisms are illustrated in Figure 1-2 [2]. Erosive wear occurs due to the impingement of particles on a surface as in Figure 1-2(a). Abrasive wear occurs when the particle slides on the surface and damages the surface through cutting and deformation. Particle sliding (two body abrasion) and rolling (three body abrasion) are illustrated in Figure 1-2(b) and 1-2(c). In the case of two body

abrasion, the particle is attached to one surface and slides on the other. In the case of three body abrasion the particle is free to roll between the surfaces.

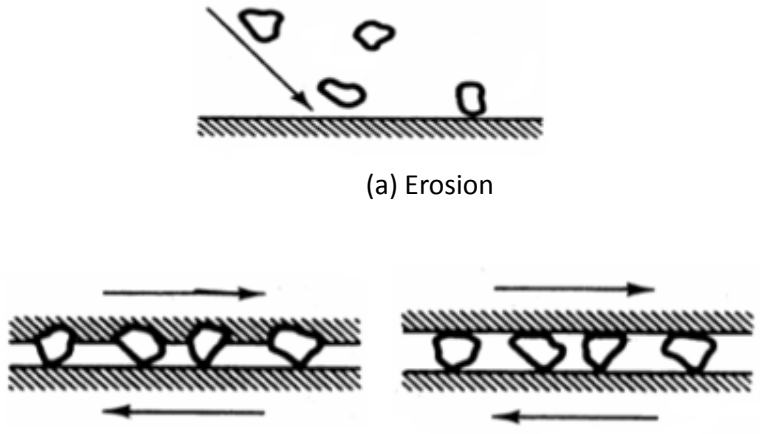

(a) Erosion

(b) Two-body abrasion (c) Three-body abrasion

Figure 1-2: Illustration of (a) erosion, (b) two-body abrasion & (c) three-body abrasion.

Erosive wear is a complex material degradation phenomenon. Erosive wear of materials occurs mainly by two different mechanisms, (a) deformation and (b) cutting by free moving particles. If a particle impinges on a surface at a relatively lower velocity, it penetrates into the surface to a depth of only a fraction of its own diameter due to elasto-plastic deformation. The concavity of the wear scar will have a radius of curvature similar to that of the particle as long as the particle does not disintegrate [1]. At considerably higher velocities craters can be formed having depth and diameter several times the diameter of particle. The high velocity collisions are often accompanied by a large heat effect [3].

Hutchings summarised the mechanisms of erosion in three different categories of plastic deformation and (or) micro-machining for ductile material [4]. The three basic types of impact damages are illustrated in Figure 1-3. Spherical particles usually deform the surface by ploughing (Figure 1-3 (a)), and displace materials to the sides and in front of the particle, normally without material loss.

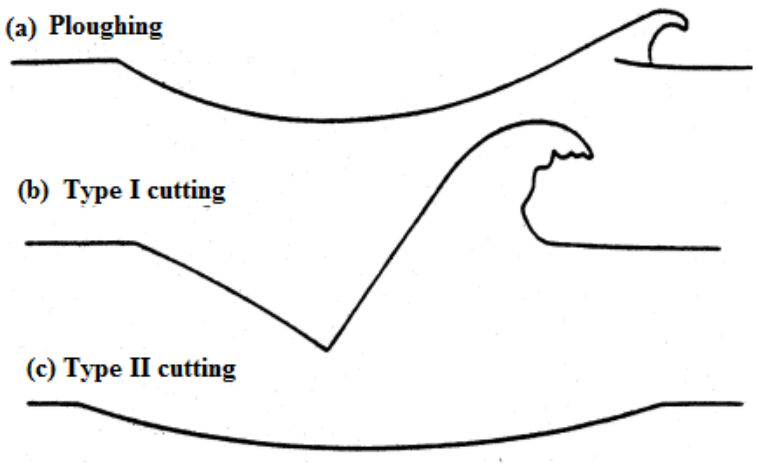

Figure 1-3: Schematic of sections through impact craters, the impact direction was from left to right. (a) Ploughing deformation by a sphere; (b) Type I cutting by an angular particle, rotating forwards during impact; (c) Type II cutting by an angular particle, rotating backwards during impact[4].

The deformation caused by an angular particle depends on the orientation of the particle as it strikes the surface, and on whether the particle rolls forwards or backwards during contact. Figure 1-3 (b) and (c) defined the type I cutting and type II cutting accompanied by deformation as the particle seem to roll forwards or backwards. Although material can be removed in a single impact type II cutting, multiple impact might be needed for type I impacts. In any case, the cutting efficiency caused by angular

particles is higher than those caused by spherical particles due to its micro-cutting machining.

The maintenance management pneumatic conveying pipelines and prediction of wear requires understanding of wear under different erosion conditions. The variety of wear appears on the entrance and exit of bend surfaces caused by conveyed product under different operating conditions. In power industries, the conveyed products, such as fly ash and coal as well as alumina in smelters are abrasive materials. In these industries, wear cannot be totally avoided even when the conveying velocity is decreased. Thus the prediction of wear on the critical areas of the conveying pipeline becomes the important criteria for maintenance management.

To predict wear in pneumatic conveying pipelines, a mathematical model based on wear mechanisms and conveying parameters has been considered in this study. The values of the physical parameters related to the phenomenon have been determined experimentally and analyzed for different wear situations.

1.2 Aim of This Study

Over the years, there have been substantial attempts to develop theoretical models to predict wear rate in particular wear environment. Enormous numbers of factors have been recognized to affect the material removal process. Nevertheless, not all the factors affect the process equally in different situations. Attempts were also made to classify the factors in groups or to determine dominant factors for particular wear situations.

Among the models, the energy based model developed by Nelson et. al. (1968) [5] on the basis of cutting and deformation mechanisms have been widely discussed and accepted for many applications [1]. According to this model energy required to remove a unit amount of material from the surface can be considered as the material property within a particular range of impact parameters. If the unit energy factors can be determined, it would be possible to determine the material removal rate in similar wear situations. It is one of the aims of this study to determine the energy factors for different combinations of particle and surfaces and relate them to the surface characteristics.

In addition, the project also focuses on the observation of morphology of the eroded surface. Characteristics of the surface morphology are related to the physical properties of the surface material and the solid particles, wear mechanism during erosion process, particle impact angle and velocity.

A detailed study of the erosion process is aimed for a better understanding of material removal processes and to determine the energy factors of predictive models for different combinations of surface and erodent particles. This will lead the way for the development of a generalized predictive model for wear of materials in any applications. The study analyses the effects of the following erosion parameters on the wear behaviour of ductile materials.

(i) Impact velocity

(ii) Impact angle

(iii) Energy factor

(iv) Surface properties

Two ductile materials have been studied: a) aluminium and b) mild steel.

1.3 Thesis Overview

Chapter 2 provides a detailed and systematic account of the developments in the field of wear and wear mechanisms, studies related to factors affecting wear and development of predictive models.

Chapter 3 describes the detail test rig, experimental procedure and methodology to determine particle velocity, impact angle and material loss from the test surfaces precisely. It also describes the calibration of the micro-sandblaster to develop the pressure-velocity relationship for the particles used in this study.

Chapter 4 describes the predictive model and its parameters. The test results are analysed quantitatively and the wear surfaces were analysed for dominant wear mechanisms using SEM.

Chapter 5 describes the procedure to determine the energy factors as well as analysed the factors with respect to materials and erosion parameters. The energy factors from the literature are also compared and discussed with respect to other experimental variables.

Finally, chapter 6 summarises the findings and concludes the discussion with future works.

Chapter 2

LITERATURE REVIEW

2.1 Introduction

In this chapter, the previous research has been discussed, which includes erosion mechanisms, formations of eroded surfaces as well as the texture and the texture formation process on the eroded surfaces. Furthermore the factors affecting the wear process in ductile and brittle materials are also discussed and summarized. Finally the wear models developed to predict the wear of materials are summarized and energy based models have been analyzed in detail.

2.2 Wear

Wear is the progressive removal of surface material due to the relative motion between solid particles and surfaces. The wear mechanism is the surface effect that is responsible for material removal from the surface. Wear is primarily divided into two categories, abrasive and erosive wear. Figures 2-1 and 2-2 show the damage of the inner surface of a pipeline transporting granular material in pneumatic conveying. The damage was caused by the impingement of conveyed product.

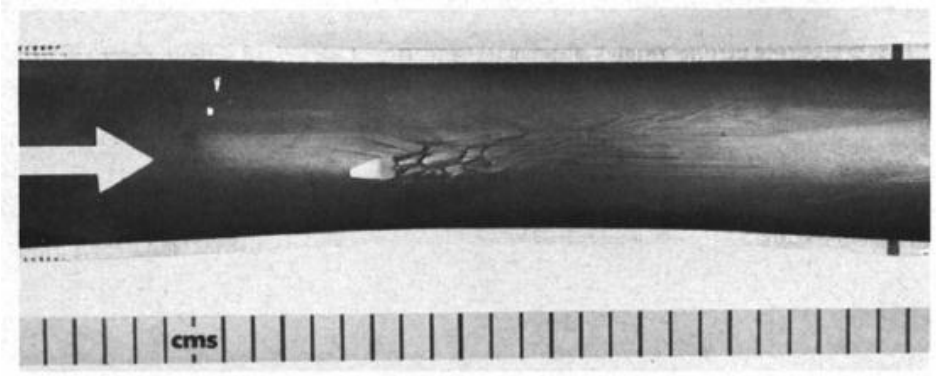

Figure 2-1: The damage eroded by the transporting particles [6].

Figure 2-2: The wear produced by abrasive and erosive wear at the same time [7].

Abrasive wear is the damage caused by the hard and angular solid particles sliding and scratching on the surface material. Usually, grooves are formed on the wear surface due to the abrading particles attached on one surface sliding on the other. Figure 2-3 shows the lines of ridges that are left on the surface due to the abrasion of the sand paper. The grooves are formed by abrasive particles of the sand paper. Ambrush et.al. [8] considered the abrasive wear produced in Figure 2-3 caused by the mechanical action of ploughing.

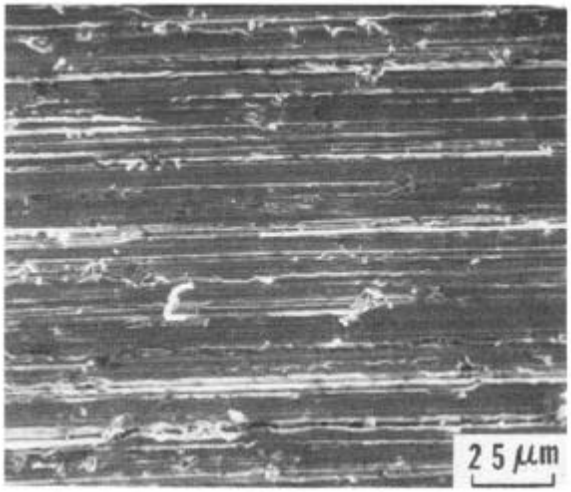

Figure 2-3: The wear caused by the 400 grit silicon carbide abrasive paper on the surface of AISI 1020 [8]

2.3 Classification of Wear

2.3.1 Erosive Wear

The erosive wear is the gradual damage of surface and removal of surface material caused by the impingement of a gas-entrained particle stream. Erosive wear is primarily caused by surface deformation and micro-cutting.

Deformation wear is the damage caused by the erosive particles of various sizes impinging on ductile surfaces. The impinged surface is plastically deformed due to the impacts. The highly deformed surface is then removed as metal platelets are extruded from the subsurface due to numerous surface impacts. Deformation wear is associated

with the plastic deformation and work-hardening and may show brittle failure of a surface under certain conditions [9].

A sketch of the sequence of surface effects due to particle impacts is shown in Figure 2-4. The lip of the platelet is extruded out of the crater in the initial stages of impact. The surface segment forms the lips of the platelets. The subsequent impact particles gradually forge the lip out. It shows the process of material removal in deformation by impinging particles.

+

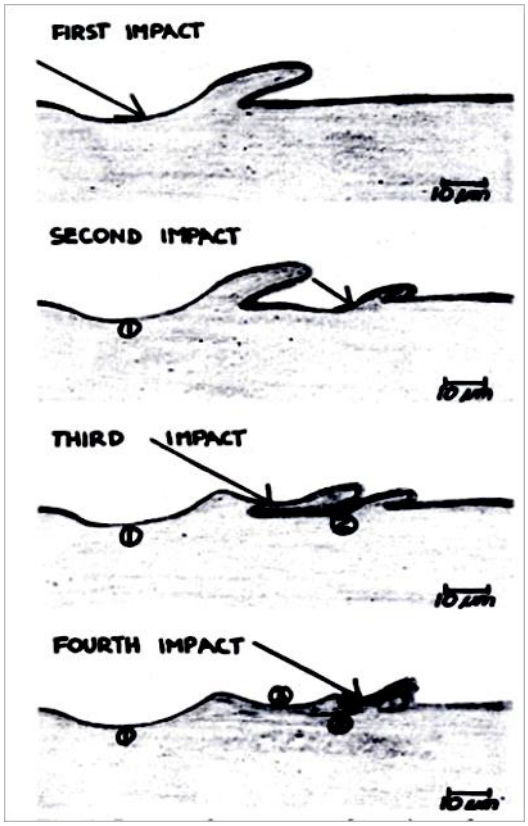

Figure 2-4: Proposed sequence of erosion of a copper-plated steel specimen [9].

Through observing eroded surfaces and detached chips, the evidence of ploughing and (or) cutting behaviour causing material removal were found [9]. The ploughing deformation predominates for spherical particles and probably a mixture of ploughing deformation and cutting occurs for angular particles [4]. The general conclusion is that erosion rates caused by angular particles are higher than those caused by spherical particles.

Cutting wear is the damage caused by the cutting action of an eroding particle. The removal of material can be different in ductile and brittle material. Hutchings et. al. believed that the mechanisms of erosion are plastic deformation and (or) micro-machining for ductile material. He proposed the three basic types of impact damage as illustrated in Figure 2-5. Spherical particles usually deform the surface by ploughing (Figure 2-5(a)), and displace material to the sides and in front of the particle, normally without material loss.

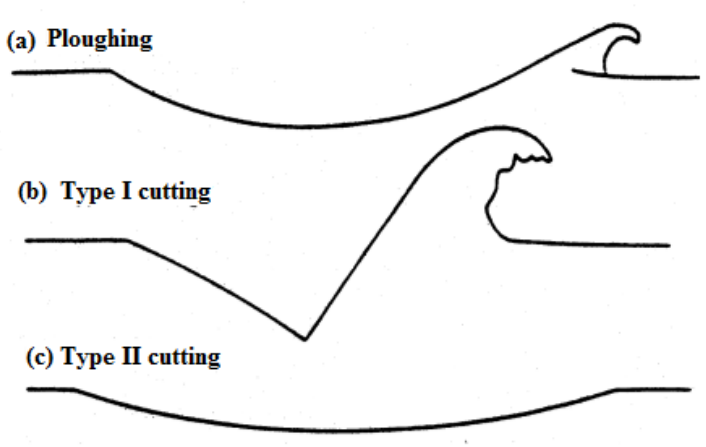

Figure 2-5: Section through impact craters formed by hard particles on a ductile metal, showing typical shapes. The impact direction was from left to right. (a) Ploughing deformation by a sphere; (b) Type I cutting by an angular particle,

rotating forwards during impact; (c) Type II cutting by an angular particle, rotating backwards during impact [4].

The deformation caused by angular particles depends on the orientation of the particle as it strikes the surface, and on whether the particle rolls forwards or backwards during contact. In type I cutting in Figure 2-5(b), the particle rolls forwards, indenting the surface and raising material into a prominent lip, which is vulnerable to be removed by subsequent nearby impacts. If the particle rolls backwards (Fig. 2-5(c)), a true machining action can occur, in which the sharp corner of the abrasive grain cuts a chip from the surface. Type II cutting occurs over only a narrow range of particle geometries and impact orientations. Each impact of type I displaces materials from eroded surfaces to form the lip and crater, but material removal does not occur until the lip and crater have experienced several cycles of plastic deformation and become severely work-hardened and breaking off.

2.3.2 Abrasive Wear

Abrasive wear is the damage of a surface caused by abrasive particles while moving along the surface. The mechanical motion of abrasive wear is sliding, rolling, and gouging. Abrasive wear is divided into two modes: two body abrasive and three body of abrasive wear.

Two-body abrasion is the damage caused by sliding abrasive particles on the surface of metal. Figure 2-3 shows the result of the two-body abrasion test where the abrasive particle is fixed on the surface of the sand paper and grinding on the surface of steel. Modi et. al. [10] measured the removed volume of surface material per unit sliding

distance as a function of the wear rate. The heat treated aluminum alloy shows higher abrasive resistance. The abrasive wear rate increased with the size of abrasive particle.

The three-body abrasive wear situation arises when a large amount of abrasive particles are trapped between two sliding surfaces. The material of each surface is removed by the cutting or deformation by free-moving abrasive particles. Wear rate in three-body abrasive wear increases with increasing size of abrasive particles. The wear rate is constant at larger size of abrasive particle [11]. The flow rate of abrasive particles has little influence on the wear rate of three-body abrasion.

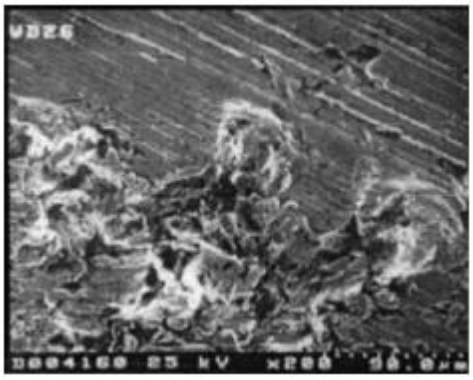

Figure 2-6: SEM picture of 0.8% C steel worn surface [12].

Liang Fang et. al. [12] conducted the three-body abrasive wear tests. The abrasive particle was silicon sand with an average particle size of 180μm in average and the surface material was 0.8% C steel. The Figure 2-6 shows the formation of craters. This shows the dominant mechanism is plastic deformation.

2.3.3 Abrasive Wear in Brittle Materials

The wear mechanisms in ductile materials have been presented in Figures of 2-5 & 2-6. Formation of cracks and fracture damage are the dominant mechanism in brittle material. The material removal from eroded materials is caused by the formation and intersection of lateral cracks in brittle materials.

A Quasi-static indenting method has been used to demonstrate the mechanisms of material removal by impacting particles [13] in brittle material. Through controlling the loading and subsequent unloading forces of the indenter, the plastic deformation and cracks in the elastic-plastic mode was observed. The loading and unloading cycle is illustrated in Figure 2-7. As the target surface is plastically deformed with increasing loading, median or normal cracks start to form. While the load is reduced, the median cracks close. On decreasing the load, the lateral cracks occur beneath the target surface. The residual stresses are responsible for the formation of these lateral cracks [14]. As the load is removed completely, the lateral cracks tend to propagate from subsurface to the surface.

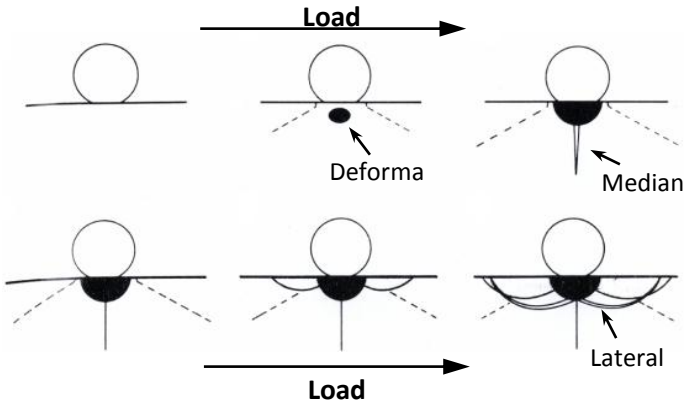

Figure 2-7: Diagram of crack formation in a brittle material by a quasi-static indenter.

A threshold value of the contact load determines whether lateral cracks can occur. Above the threshold load, lateral cracks are formed. Below this critical load, lateral cracks do not occur. For the impact particles in comparison with the quasi-static indenter, a threshold value of particle velocity is used instead of a critical load.

2.4 Formation of Ripple

Ripple is a surface texture which is formed in soft ductile material due to the particle impact angle at shallow angles [15]. The formation of a ripple is dependent on the particle impact angle and velocity. The wavelength and amplitude of ripple is dependent on the erosion rate. If the impact angle is large, the pattern becomes a more irregular wave form. If the erosion continues, the amplitude of ripple increases and the radius of curvature of the ripple (valley) decrease to match the size of the particle.

Finnie et. al. [15] conducted experiments to investigate the reason for ripple formation in ductile material which tend to disappear at high impact angles and the particle mass flow rate does not contribute to the formation of the ripple. Although he did not confirm the reason for the ripple formation in ductile material, he suggested that the ripples are developed from the random roughness gradually reformed to a regular pattern.

Talia et. al. (1996) and his co-worker [16] investigated the relationship between the ripple formation and erosion rate. They conducted the erosion tests by sand-blasting the accelerating particle stream of 304μm alumina on the flat surface of aluminium. Figure 2-8 presented the wear rate and ripples on the surface of pure aluminium eroded by 406μm angular alumina with the impact velocity of 70 m/s at 30 degree. They showed

that there was no change in erosion rate as the mass of erodent particles is increased. The ripple is developed as the mass of erodent particles is increased.

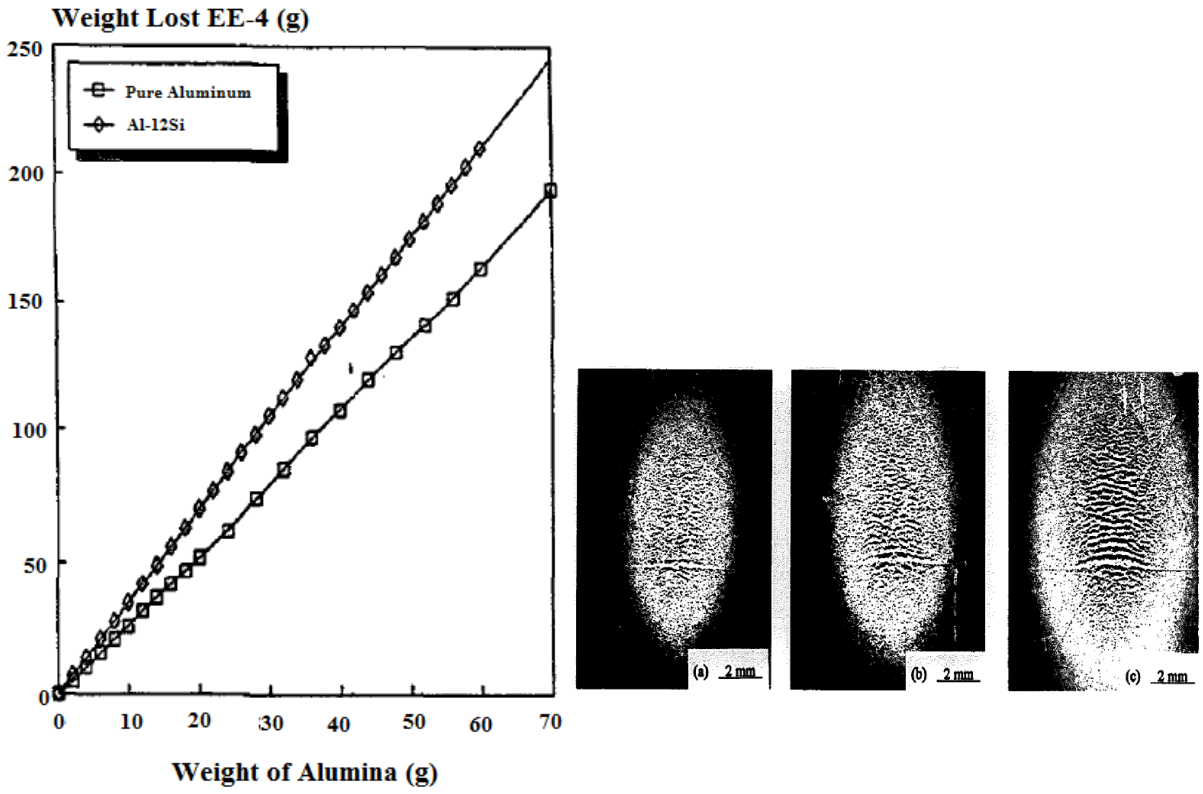

(a) **(b)**

Figure 2-8: (a) Shows the weight loss of pure Al and Al-12Si vs. particle weight of 406 µm Al_2O_3 erodent particles at 30°, travelling at 70 m/s. (b) Shows the eroded surface after: (a) 8g; (b) 16g; (c) 32g of particle [16].

In Figure 2-9, the pure aluminium was eroded by 400µm spherical glass beads. It shows no erosion for less than 15g of beads but the ripple starts to develop in this incubation period. This demonstrated that ripple formation is not necessarily associated with material removal from the surface. Talia et. al.(1996) observed that the removal of loose flake at the back of the ripple is the cause of erosion.

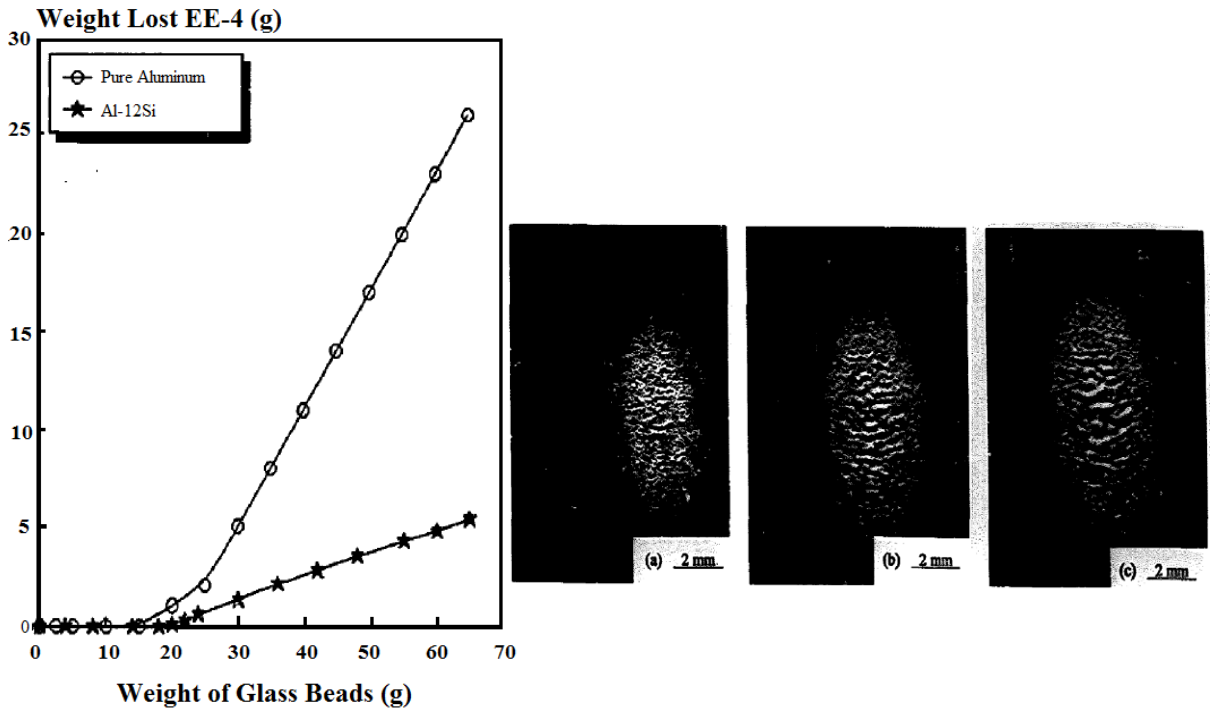

(a) **(b)**

Figure 2-9: (a) Weight loss of pure aluminium vs. accumulated weight (g) for glass beads impacting at 30^{o}. (b) Surface ripples after impacting (a) 5g; (b) 15g; (c) 30g of particle [16].

2.5 Particle Characteristics

In 1991, Liebhard et. al. [17] investigated the sensitivity of erosion rate under the influence of physical properties of erodent and performance of particle stream. They conducted the experiment at room temperature on 1018 steel using spherical glass beads and angular silicon carbide. They concluded that the angular particulate contributed more to the performance of erosion. The angular particulate has more ability to

penetrate into the surface than spherical particles as the angular particle impinging on surface have higher force intensity compared to spherical particles.

In 2001, Stachowiak el. al. [18] investigated the abrasive characteristics on three-body abrasive wear. The image of different wear particles are shown in figure 2-10.

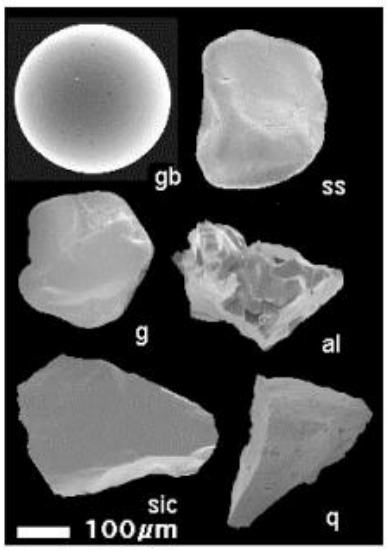

Figure 2-10: Angularity of abrasive; gb=glass bead ss=silica sand g=Garnet q=Quartz sic=silicon carbide al=alumina [18].

Stachowiak et. al. (2001) [18] examined that the quartz particles were fractured during testing. Since quartz and silicon carbide particles have a higher aspect ratio (length/width), the minor dimension orients them to the sliding direction. This shape may lead to less sharp edge engaging in abrasion. They also examined that the least embedded particles were recorded for glass bead. Sand and garnet produced four times more embedded debris. Silicon carbide has six times and quartz has eight times of embedded debris comparing to glass beads.

Figure 2-11 compared the surface characteristics with the material removal rates for the different particles, due to the varying angularity. In Figure 2-11 (a), the smooth and

round indents shows the plastic deformation leading to smallest material removal. In Figure 2-11 (b) & (c), the surface abraded by sand exhibit indents due to plastic deformation and garnet abraded by scratch due to ploughing and cutting. The higher mass loss of garnet is due to the higher value of SPQ (Spike parameter–quadratic fit), leading to higher amount of scratching. In Figures 2-11 (d) & (e), the worn surface show narrow and sharp scratch correlated to the angularity of quartz and silicon carbide.

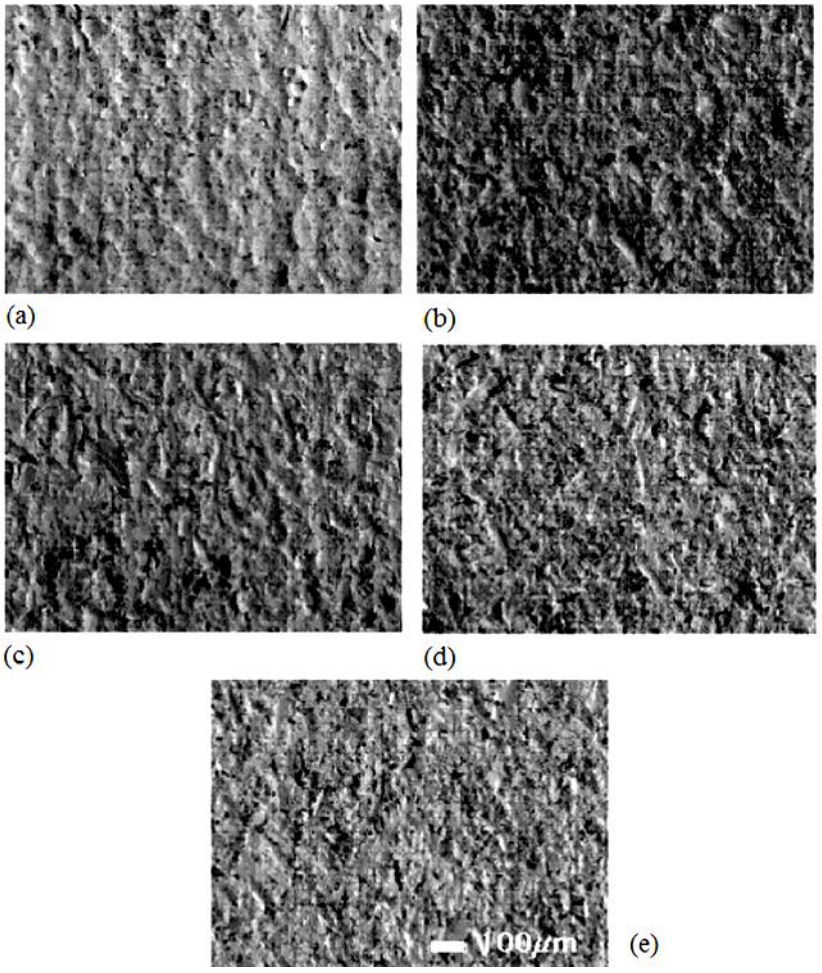

Figure 2-11: SEM micrograph of embedded debris of abrasive in worn brass (a) Glass beads (b) Silica sand (c) Garnet (d) Quartz and (e) Silicon carbide [18].

In Figure 2-12(a), Stachwiak et. al. [18] stated that alumina showed the steepest increase in wear rate followed by quartz and sand and, in Figure 2-12(b), the wear rate of cast iron was quite small for glass beads and sand but higher than mild steel for quartz and alumina.

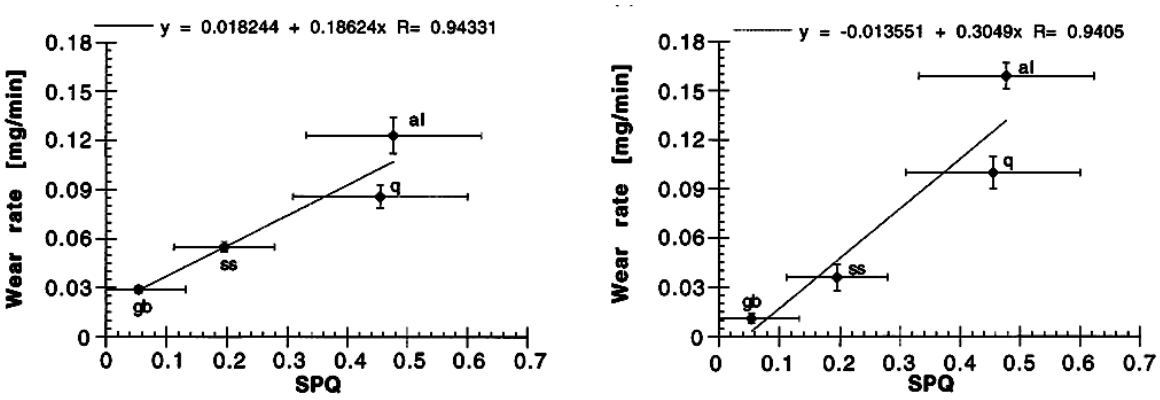

(a) **(b)**

Figure 2-12: Average wear rate of (a) Mild steel (b) High Cr white cast iron plate under the influence of angularity of abrasive in slurry [18].

As stated earlier, Liebhard et. al. [17] also demonstrated that the angularity of particulate material contributed to the performance of erosion. The angular particle has more ability to penetrate into the surface than spherical particle. Bitter [7] analysed that the corner of angular particle impacting on the surface has high energy density due to its small curvature.

Liebhard and Bitter [17, 7] also investigated the effect of spherical particle on mass loss of target material. The experiment involved erosion of 1018 steel at room temperature

and eroded by spherical glass beads. The mass loss of target material was dependent on the kinetic energy of the particle stream, ability of particle penetration, number of particles impacted on the surface as well as other impact parameters such as coefficient of restitution and particle-particle interactions. In their investigation, the kinetic energy was calculated by :

$$E_{kin} = ½mv^2 = \frac{volume \times density \times v^2}{2} = \frac{\left[\frac{diameter}{2}\right]^3 \times \pi \frac{4}{3} \times density \times v^2}{2}$$

(2-1)

Mass loss of 1018 steel impacted by 300μm glass beads at 60 m/s with a feeding rate of 0.6g min^{-1} was 25% higher compared with a feeding rate of 6 g min^{-1}. The higher erosion at lower solid loadings is due to less particle to particle interference and the random rebounding of particles.

Liebhard et. al. (1991) [17] found that, at impact velocity of 20 m/s, the mass loss of 1018 steel is proportional to the size of the silicon carbide particles within the size range up to 200μm. The result was explained as the increasing size of particulate increases the kinetic energy. For particles larger than 100 μm, the mass loss of 1018 steel is dependent on the following factors:

i) The particle size

ii) Number of particles striking the surface

iii) Kinetic energy

iv) Interference between incoming and rebounding particles

Solid loading is the mass of particles impacting on the surface of the target material per unit time. This is also defined as feeding rate and it is largely dependent on the size of particle. Liebhard et. al. (1991) [17] demonstrated that, for 250-300μm silicon carbide particles with a velocity of 60m/s, the mass loss of 1018 steel is higher for lower feed rate (0.6g/min) than that in higher feed rate (6g/min). It was also shown that the distance between the particles is three times higher at the lower feeding rate than that in the higher feeding rate and hence the particles have enough time to impinge on the surface of the target material and leave the area before next particle impacts at the same location.

2.6 Experimental Work

Morrison et. al. [19] showed a series of typical curves of mass loss of stainless steel versus accumulative mass of 130 μm alumina at an impact velocity of 100 m/s. The stainless steel was commercial grade cold-rolled 304 stainless steel plate. Figure 2-13 showed the experimental wear loss with respect to the erodent mass impacted. The slope of the curve is the steady state erosion rate.

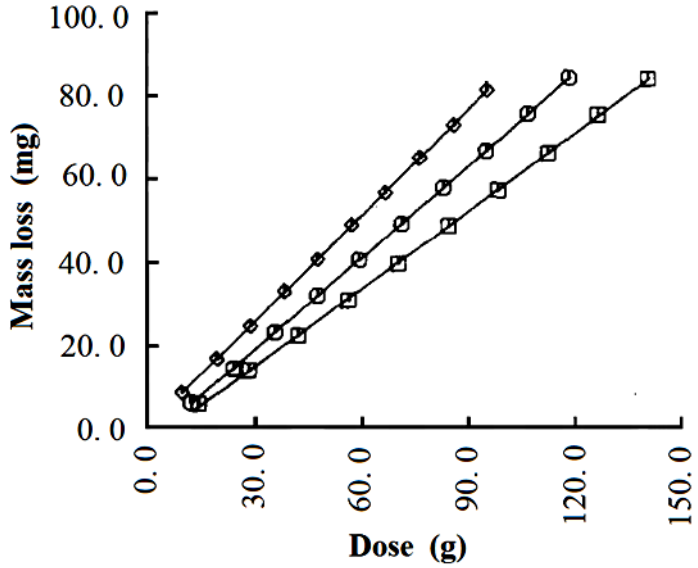

Figure 2-13: Morrison and Scattergood [19] showed the determination of erosion rate. From left to right, 45°, 60°, 90°.

Figure 2-14 showed the steady state erosion rates for ductile material (304 stainless steel) for 130 μm alumina with particle velocity of 100 m/s for different angles of impact from 0 to 90^0. It shows the maximum erosion rate occurs at low impact angles of about 15^o – 20^o.

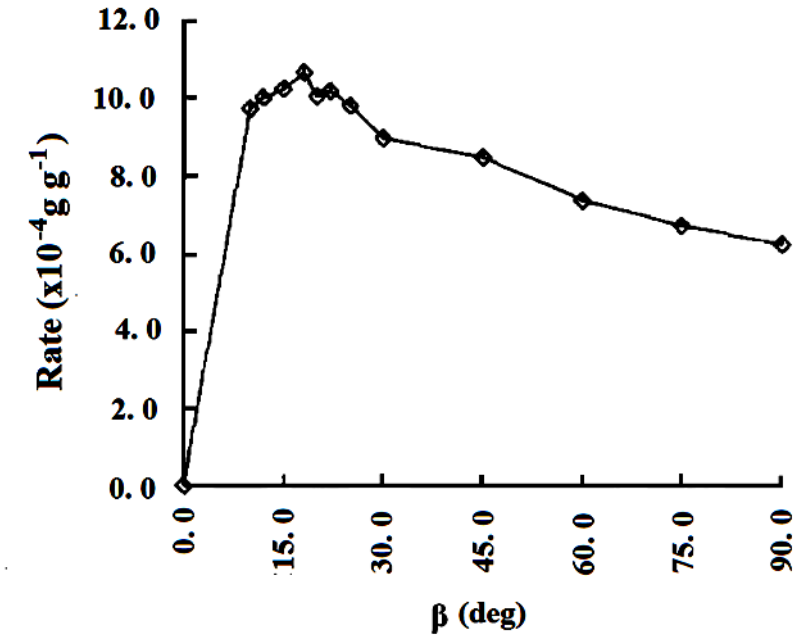

Figure 2-14: The erosion rate of 304 stainless steel at different impact angle, β, by alumina at particle velocity of 100 m/s [19].

Morrison and Scattergood [19] also conducted (Figure 2-15) the same experiment using a different size of erodent. They concluded that the erosion rate becomes saturate for the larger size of particles. They also concluded that the particle size dependence of erosion rate is the same at all impact angles.

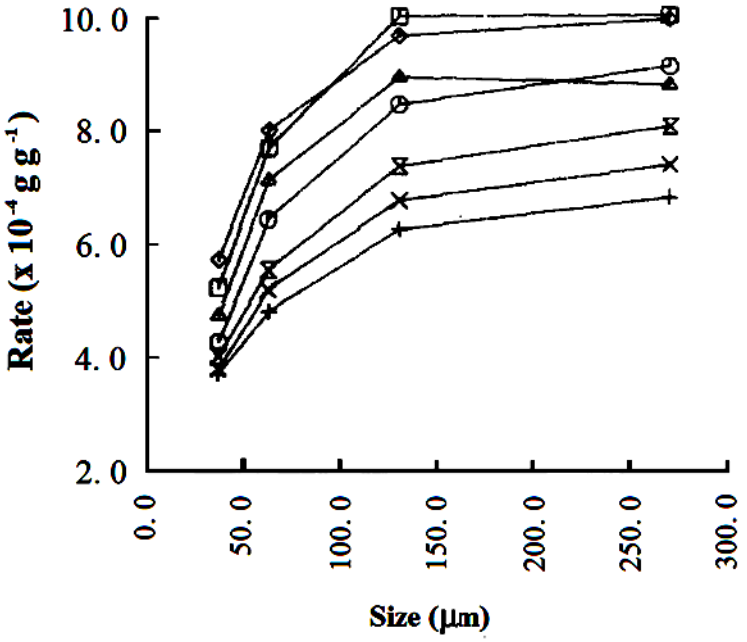

Figure 2-15: Effect of particle size on erosion rate of 304 stainless steel at 100 m/s for angles of 20° to 90° from top to bottom [19].

In 1969, Tilly et. al. [20, 21] investigated the surface characteristics of different types of material shown in the following Table 2-1 [21].

Table 2-1 Target materials of different composition tested by Tilly [21].

Material	Composition (wt. %)
11% chromium steel	11 Cr, 016 C, 0.7 Mn, 0.3 Si, 0.6 Mo, 0.25 Nb, 0.3 V, bal. Fe
Nickel alloy	20 Cr, 2.5 Ti, 1.5 Al, 20 Co, 5Fe, 1.5 Si, 1.0 Mn, bal. Ni
Titanium alloy	6 Al, 4 V, bal. Ti
Aluminium alloy	1.2 Ni, 0.1 Ti, 1.0 Fe, 1.5 Mn, 2.5 Co, bal. Al
Beryllium copper	2 Be, bal. Cu
Mild steel	0.0042 C
Flame plated tungsten carbide on steel	Flame sprayed carbide particle bonded by 15% cobalt cement
Glass	Annealed soda glass
Nylon	Type 66 nylon
Carbon-reinforced nylon	25% carbon fibres in type 66 nylon
Polypropylene	Compression moulded sheet
Fibreglass	78% glass fibres in epoxy resin
Polyvinylidene fluoride on steel	Dip-coated resin stoved for 5 min at 270°C for each layer

Tilly concluded that both glass and steel are not influenced by the nonlinearity of the erosion rate. In Figure 2-16(a), aluminium alloy has a significant incubation period of erosion at normal impact. The particles are initially embedded in the surface but these are subsequently removed and steady state erosion occurs.

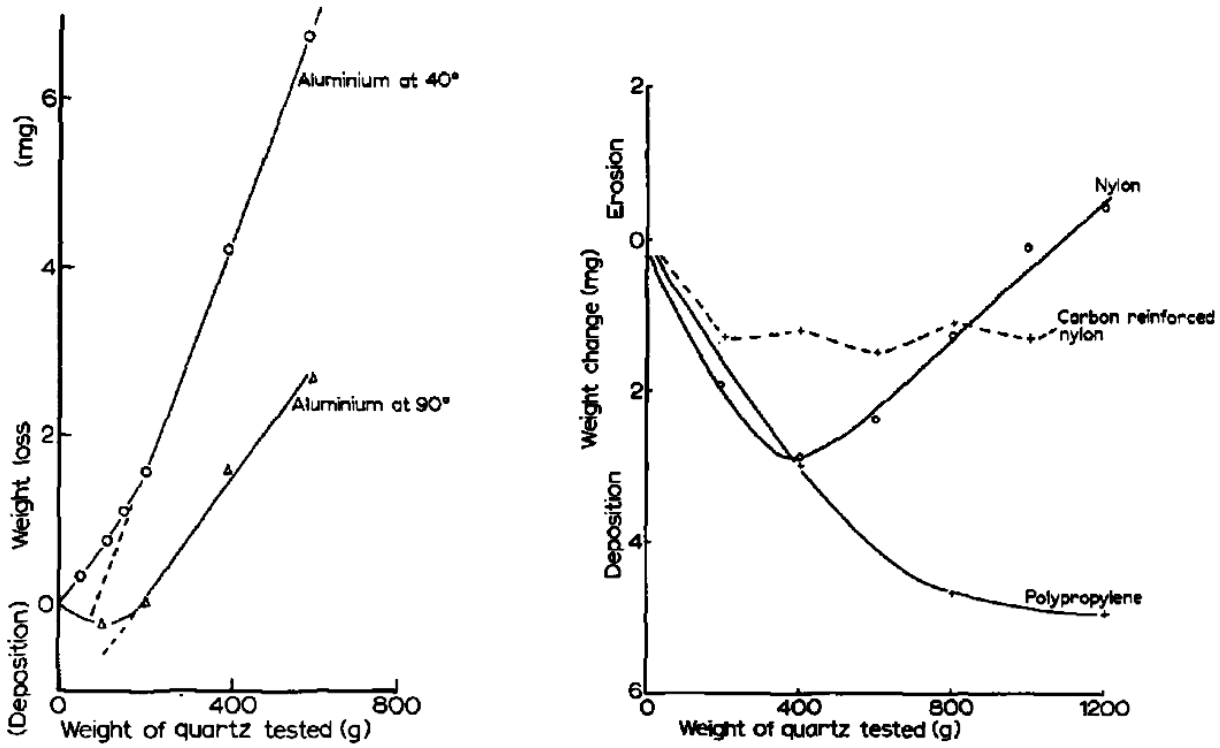

(a) (b)

Figure 2-16: (a) Mass loss of aluminium at 90 degree and 40 degree of impact angle for different impinged mass; (b) Mass loss of type 66 Nylon, carbon reinforced nylon and Polypropylene at 90 degree [21].

In Figure 2-16(b), Tilly et. al. showed that at normal impact, carbon reinforced nylon exhibits the characteristics of a ductile material and stabilises the weight gain before a steady state wear rate is achieved. Polypropylene exhibits a long incubation period of

erosion and behaved differently than nylon. The experimental data of aluminium, carbon-reinforced nylon, polypropylene and nylon demonstrate the deposition of abrasive into the surface as well as the comparative wear rates in these materials.

Tilly also conducted the erosion tests of selected materials from ambient temperature to 600^{o}C as shown in Figure 2-17. Tilly showed that the erosion of Nickel alloy at impact angle of 40^{o} increased about 50% at temperature of 600^{o}C. Titanium alloy exhibits a decrease of 50% at a temperature of about 600^{o}C. The general trend was that the erosion rate decreased with increasing temperature except for 11% Chromium which remained constant.

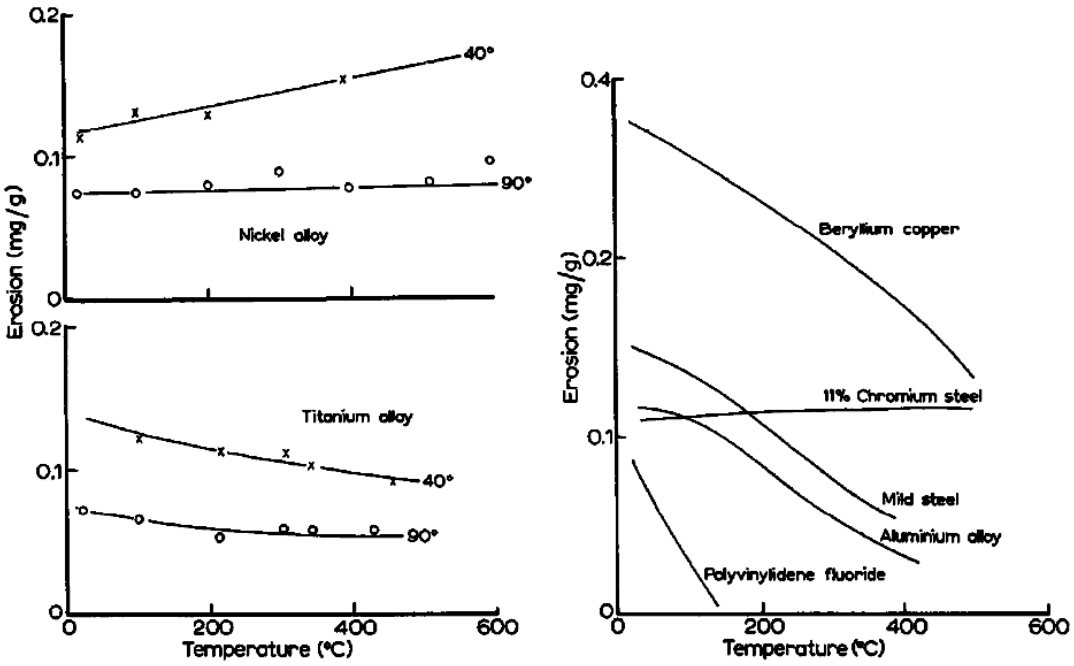

Figure 2-17: Variation of erosion rate with increasing temperature for different surface materials as noted on the graph [21].

Levy et. al. [22] investigated the effect of physical properties of erodent on the erosion rates for different materials. They showed that the erosion rate of AISI 1020steel

(Vickers Hardness of 150 kgfmm^{-2}) remains constant as the hardness of impinged particle reaches approximately 700 kgfmm^{-2} as shown in Figure 2-18.

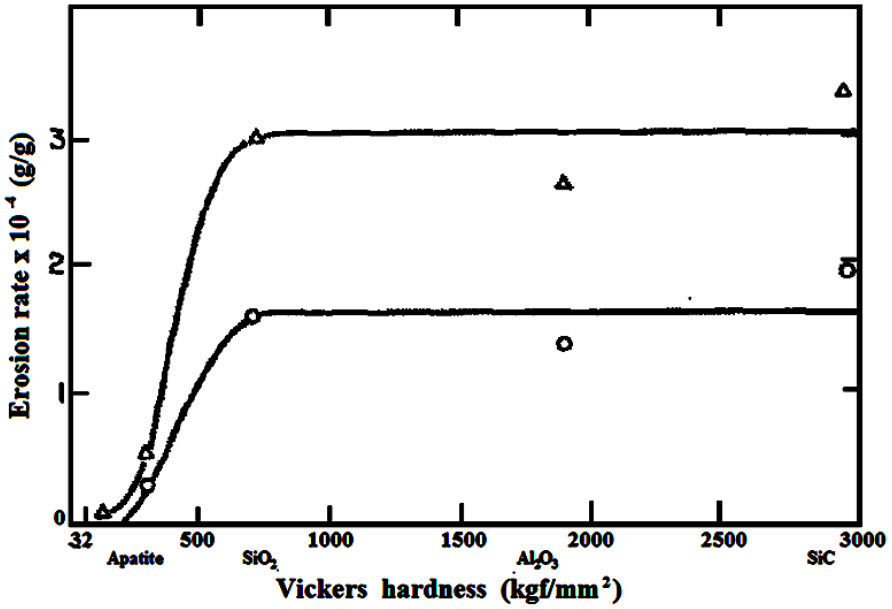

Figure 2-18: Erosion rate of 1020 steel as a function of Vickers hardness [22].

2.7 Surface Morphology

Figure 2-19 compares the morphology of three wear surfaces eroded by different erodents [22]. The lowest erosion rate was observed in alumina (Figure 2-19(b)) while silicon carbide registered the highest wear rate among the three erodents. The difference in erosivity between these three particles is primarily due to the small difference in angularity.

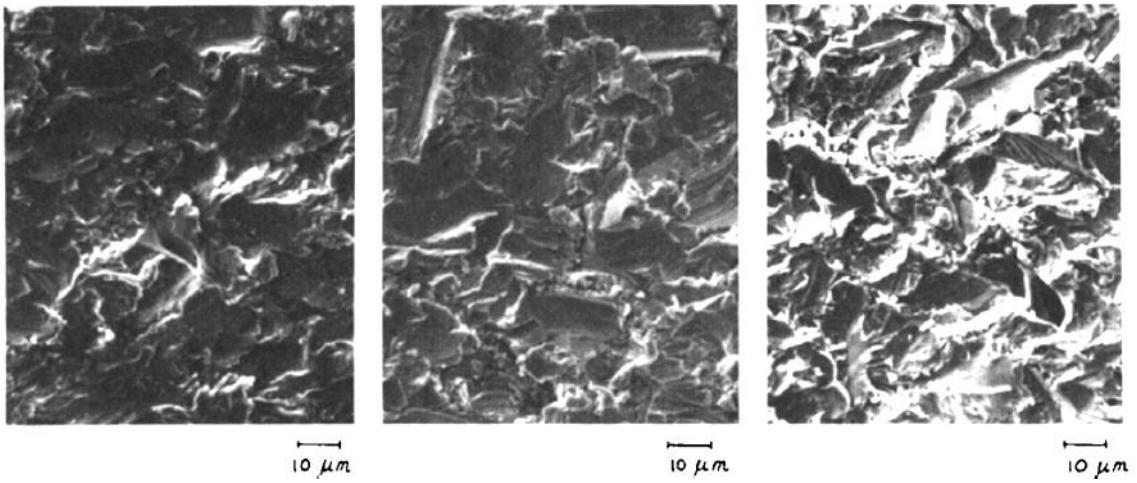

(a) (b) (c)

Figure 2-19: Surface eroded by (a) Sand (SiO) Er=3.0 x 10^{-4} gg^{-1} (b) Alumina Er=2.6 x 10^{-4} gg^{-1} (c) Silicon carbide Er=3.3 x 10^{-4} gg^{-1} at 80 m/s; Er = erosion rate [22].

Figures 2-20 and 2-21 showed the particle angularity before and after erosion experiments for alumina and silicon carbide. Levy et. al. [22] observed that alumina showed more rounding of the sharp corners than the silicon carbide particles. Silicon carbide and sand showed little sign of rounding of corners after impacts and remains approximately the same after impact as they were before. The integrity of particles is sufficiently high when impingement on the AISI 1020 carbon steel at velocity of 80 m/s without fracture.

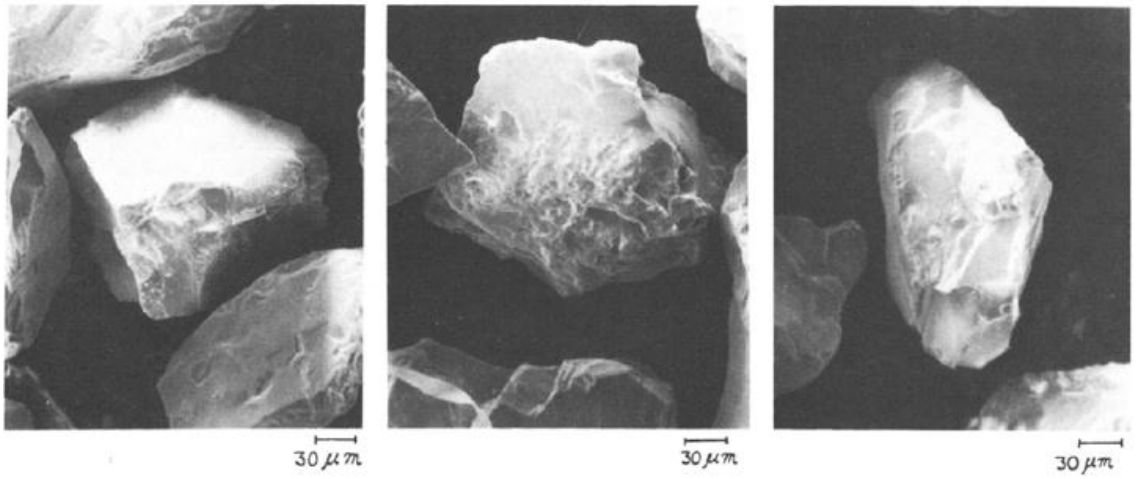

(a) (b) (c)

Figure 2-20: Particle characteristics before and after impact of 180-250 μm alumina (a) Before impact (b) After impact at 30° on AISI 1020 steel V=80 m/s (c) After impact at 90° on AISI 1020 steel ; V=80 m/s[22].

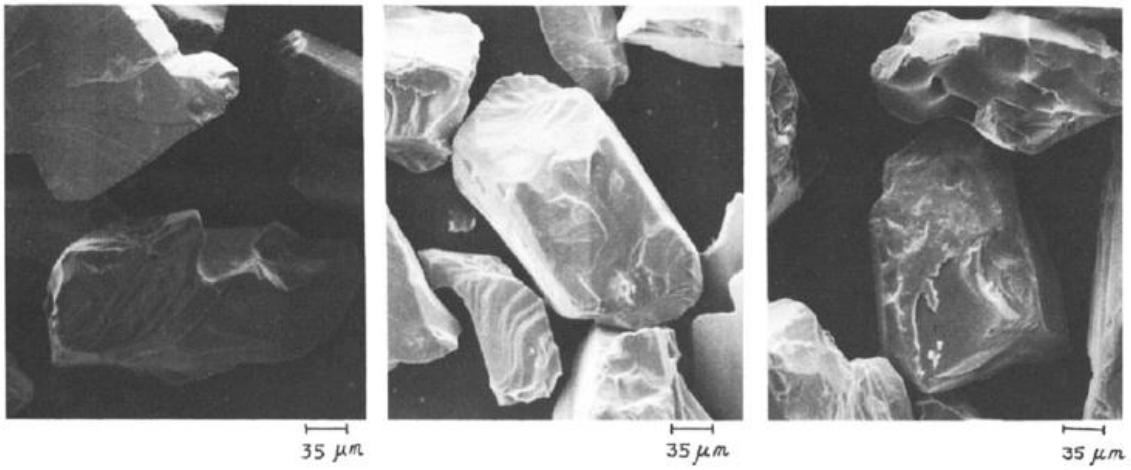

Figure 2-21: Particle characteristics before and after impact of 180-250 μm silicon carbide (a) before impact (b) after impact at 30° on AISI 1020 steel V=80 m/s (c) after impact at 90° on AISI 1020 steel ; V=80 m/s [22].

Levy et. al. (1983) [22] suggested that the scratches and parallel lines on the surface of particles are due to the crushing and fracture. In his study, the rounded steel shot showed much less erosivity than angular steel grits.

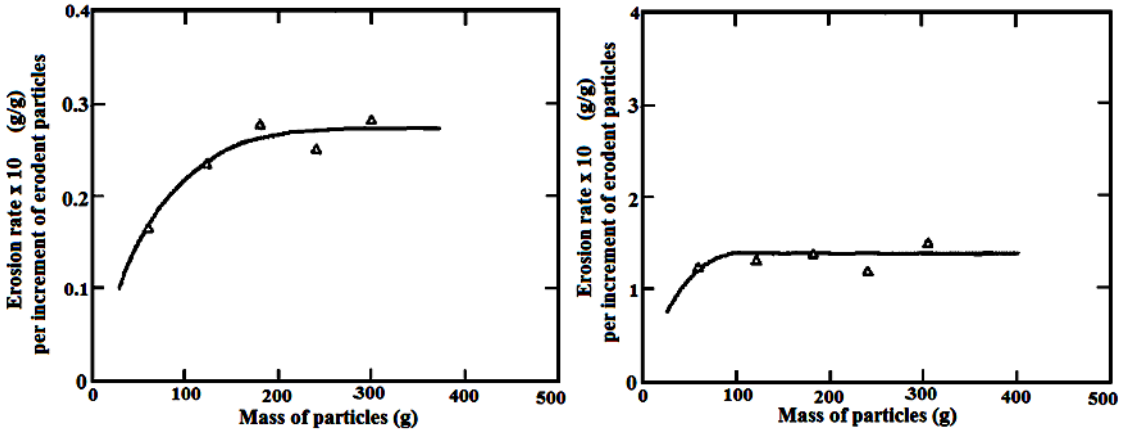

(a) (b)

Figure 2-22: Erosion characteristics of AISI steel eroded by (a) Apatite particle (180μm) and (b) Alumina particle (250 μm) at V=80m/s, α=90^{o} and T=25^{o}C [22].

Levy et. al. [22] observed that the erosion rate of apatite (in Figure 2-22(a)), which was broken up on impact, is much lower than the erosion rate of alumina (in Figure 2-22(b)). Alumina transmitted more energy to the AISI 1020 steel than fragmented apatite causing higher damage to the surface. AISI 1050 steel obtain the steady state erosion rate after impinged by 200gm of apatite. Whereas alumina developed the steady state erosion rate after impinging of only 50gm of alumina.

2.8 MODELING

2.8.1 Micro-machining Model

In the mid-1950s, Finnie [23] proposed first model to explain the erosive wear phenomenon of ductile materials, by angular particles. With a number of assumptions, a theoretical model of the micro-machining mechanism of erosion was developed based on particle velocity and impinging angle. This is still considered the fundamental achievement in the study of the erosion mechanism of ductile materials.

During erosion of ductile material, a large number of abrasive particles strike the surface. Some of these particles will land on flat faces and do no cutting, while others will cut into the surface and remove material. The model was developed for material removal from the surface based on an idealized particle interaction with a surface as presented in Figure 2-23.

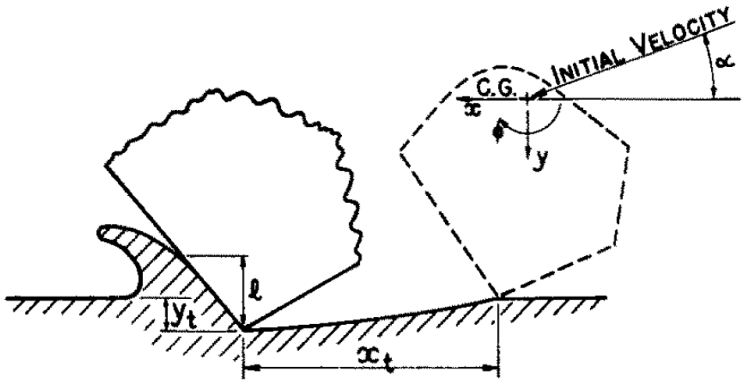

Figure 2-23: Idealized picture of abrasive particle striking a surface and removing material. Initial velocity of the particle's centre of gravity makes an angle α with the surface [23].

The equations of motion were derived and solved for the idealized particle, and the predicted material loss was compared with the experimental results. To solve the equations of motion of the particle the following assumptions were made:

1) The ratio of the vertical and horizontal component of the force was assumed to be of constant value (K). This is reasonable if a geometrically similar configuration is maintained throughout the period of cutting.
2) The depth of contact (l) to the depth of cut (y_e) has a constant value (ψ).
3) The particle cutting face is of uniform width, which is large compared to the cutting depth and
4) A constant plastic flow stress (p) is reached immediately upon impact.

The volume of material Q removed by a single abrasive grain of mass m, velocity V and impact angle α was given by

$$Q = \frac{mV^2}{p\psi K}\left(\sin 2\alpha - \frac{6}{K}(\sin^2\alpha)\right) \quad for\ \tan\alpha \le \frac{K}{6} \tag{2-2}$$

$$Q = \frac{mV^2}{p\psi K}\left(\frac{k\cos^2\alpha}{6}\right) \quad for\ \tan\alpha \ge \frac{K}{6} \tag{2-3}$$

The first equation applies to lower impact angles for which the particle leaves the surface while still cutting. The second equation applies to higher impact angles in which the horizontal component of the particle motion ceases while still cutting. The critical angle α_c is the impact angle at which the horizontal velocity component has just become zero when the particle leaves the body; i.e., the impact angle above which the residual tangential speed of the particle equals zero.

The model relates both the impact velocity and impact angle to material removal. Finnie [23] conducted the erosion experiment on copper, SAE 1050 steel and aluminum by impinging the silicon carbide on the surface of these ductile materials at different impact angles with a given impact velocity. The model underestimated the experimental data at impact angle of 90^{o}. The following figure represents the model output and experimental data.

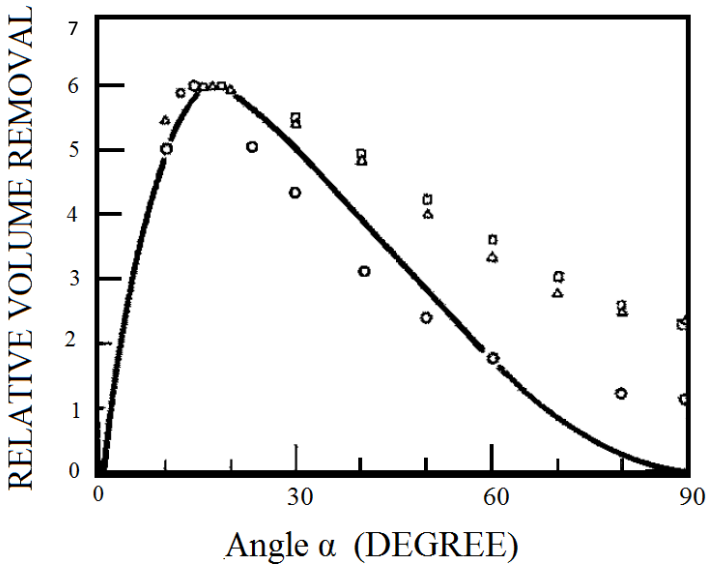

Figure 2-24: Predicted and experimental rate of volume removal with angle for different ductile materials. The data point: square – SAE 1020 steel, triangle – copper, circle – aluminium [23].

The experimental data closely agreed with predicted erosion data at different angles except closer to the normal impacts (in Figure 2-24). Finnie derived the simplified equation for estimating the maximum erosion written as below:

$$Q = 0.075\left(\frac{MV^2}{2}\right)\frac{1}{p} \qquad (2\text{-}4)$$

where, p is the constant plastic flow stress, determined by very high strain rate.

Finnie obtained the values of p between 350000 and 400000 p.s.i. (2.41-2.75 GPa) when low-carbon steel (SAE 1020) impacted by 250μm silicon carbide with 76m/s at an angle of 20^o [23].

In 1963, Bitter [7] developed a model describing the deformation and cutting wear. In his model the free-moving angular particles impinge on the surface at different angle and velocity. Bitter's model was capable of describing wide variety of erosive particles than that of Finnie. In the following section modeling of deformation wear and cutting wear are briefly described.

2.8.2 Deformation Model

Bitter considered the deformation of surface caused by the repeated impacts of solid particles. He derived the equation of deformation wear by relating the maximum stress in the impacted area to the impact velocity of solid particles.

Bitter considered the energy balance of collision and defined the energy of erosion as following:

$$\boldsymbol{Q_P \approx [\sqrt{Q} - \sqrt{Q_e}]^2 = ½m[V - K]^2} \quad (2\text{-}5)$$

where

Q is the initial kinetic energy of particle, Q_e is the elastic deformation energy, Q_P is the amount of energy contributed for the formation of permanent indentation and m is the mass of particle.

Bitter suggested that Q_e is small in relation to Q_P in ductile material and concluded that the energy of erosion (Q_P) is proportional to the mass of the impinged particle. Bitter introduced the empirical parameter, energy factor, which is defined by the following equation:

$$W_D = \frac{M(V\sin\alpha - K)}{\varepsilon} \tag{2-6}$$

where

α is the deformation impact angle of the air-particle stream, M is the mass of particle impacted on the surface, kg, W_D is the unit mass loss from the surface, kg, V is the particle velocity m/s, K is the velocity of collision at which the elastic load limit in just reached, in m/s and ε is the amount of energy required per unit mass of material removed and termed as deformation energy factor, J/kg.

The deformation energy factor can be expressed as the quantity of energy required to remove one unit mass of material. Bitter's equation shows that the erosion volume is largely dependent on the impinged mass of the particles, the constant K, and the energy factor, ε. The energy factor is dependent on the operating condition, physical and material properties and external environment. The constant K is the velocity of impact particle at which the surface experiences the maximum elastic load. Bitter showed that the value of K remains constant and is small in relation to the impact velocity of erosion in a ductile material.

2.8.3 Cutting Model

The cutting process is associated with the material removed through cutting from the surface. The cutting wear is largely dependent on strain due to impact of particle on the target material.

There are two situations to be considered the cutting process:

(a) The horizontal component of impact velocity is not zero when particle leaves the surface

$$W_{c1} = \frac{\frac{1}{2} m(V_{\parallel}^{2} - v_{\parallel}^{2})}{\phi} \tag{2-7}$$

(b) The horizontal component of impact velocity becomes zero when the particle leaves the surface

$$W_{c2} = \frac{\frac{1}{2} m V_{\parallel}^{2}}{\phi} \tag{2-8}$$

where $v_{||}$ the residual horizontal velocity while leaving the surface as a result of decelerating from the initial horizontal velocity of $V_{||}$, m, the mass of particle, ϕ, the cutting energy factor, W_{c1} & W_{c2} represents the volume of material removed in two different cases.

For (a), $v_{||}$ is non-zero when the impact angle is less than α_o and the cutting process continues as the particle leaves the surface. For (b), $v_{||}$ becomes zero before the particle leaves the surface. Bitter derived the horizontal component of impact velocity becomes zero before the vertical component of impact velocity cease if the impact angle of solid

particle is greater than 84.5^{o}. If the horizontal and vertical component of impact velocity becomes zero at the same time, the elastic deformation energy restored to the particles.

To determine boundary condition for cutting erosion, Bitter's model can be described by two equations as follows:

$$W_{c1} = \frac{2MC(V\sin\alpha - K)^2}{\sqrt{V\sin\alpha}}\left(V\cos\alpha - \frac{C(V\sin\alpha - K)^2}{\sqrt{V\sin\alpha}}\phi\right) \tag{2-9}$$

$$W_{c2} = \frac{\frac{1}{2}M[V^2\cos^2\alpha - K_1(V\sin\alpha - K)^{\frac{3}{2}}]}{\phi} \tag{2-10}$$

where

α is the impact angle of the air-particle stream, degree, M is the mass of particle stream, kg, W_{C1}, W_{C2} are expressed in unit of mass loss, in kg, K is the velocity of collision at which the elastic load limit is just reached, in m/s, K_1 is the constant for the residual parallel component velocity of particle, $\emptyset$ is the amount of energy required to remove unit mass of material and termed as cutting energy factor, J/kg

Equation (2-9) describes the particle with positive parallel component of impact velocity as the particle leaves the surface. This residual parallel velocity component is just zero as the impact angle reaches to an acute angle α_o from zero. From experimental data of Bitter, for ductile material the acute angle α_o is generally less than 15^{o}. For

equation (2-10), if V *sin* α ≥ K , both equation 2-9 and 2-10 can be used. If $\alpha \geq \alpha_o$ equation 2-10 can be used. If $\alpha \leq \alpha_o$ equation 2-9 can be used.

Bitter compared equation 2-10 with the Finnie equation and derived the equivalent equation as given by:

$$W_{c2} = \frac{MV^2 \cos^2 \alpha}{6\varphi.y} \tag{2-11}$$

where

φ is the ratio of length to depth of the scratch formed, y is the constant pressure between particle and eroded body, If 3 φ y = ϕ , the equations of Bitter and Finnie are identical.

2.8.4 Model for Particle Distribution in Air Stream

In 1993**,** Shipway and Hutchings [24] studied the scattering of air-particle stream while leaving the acceleration nozzle. A focus coefficient term for different nozzles has been derived to describe the spread of the plume. That is, the smaller the value of β, the more widely the plume would spread. The phenomenon was described by the following equation:

$$r = \frac{h}{\beta}\ln(m) - \frac{h}{\beta}\ln(\frac{2\pi.h^2 Q_{crit}}{\beta^2}) \tag{2-12}$$

where, radius of eroded area, r, in mm, is proportional to the stand-off distance, h, in mm, mass of impinged particles per unit area, Q_{crit}, in g/mm^2, and inversely proportional to focus coefficient, β, which is a non-dimension variable.

In 1994, Shipway et. al. [25] worked on a method to assess the degree of inter-particle interaction for the purpose of minimizing the collision between particles during erosion experiments. They derived the equation to calculate the average distance between particles as following:

$$L = [\frac{mU\pi.r^2}{Q_o}]^{1/3} \quad (2\text{-}13)$$

where

Q_o is particle mass flow rate, U is the mean particle velocity, r is the nozzle radius, m is the mass of each particle.

They concluded that the particle-particle spacing is greater than ten times the diameter of particle and the flux can be as high as 47.6 kgm^{-2}s^{-1} without significant interference.

Elastic deformation constant is the velocity for which the particle impact stress reaches the elastic limit for the material. If the stress of impact particle just reaches the elastic limit no erosion would occur. As long as the impact stress of particle exceeds the elastic limit, plastic deformation will occur. Higher compression pressure will be required for plastic deformation. Therefore, compression forces higher than that of elastic deformation constant generate the plastic deformation on the surface layer that initiate the material removal process.

According to the equation derived by Bitter [7], the constant K is

$$K = \frac{\pi^2 y^{\frac{5}{2}}}{2\sqrt{10}} \left(\frac{1}{d}\right)^{1/2} \left[\frac{1-q_1^2}{E_1} + \frac{1-q_2^2}{E_2}\right] \quad (2\text{-}14)$$

where,

d is the density of particles, y is the maximum elastic limit load, E_1 Young modulus of sphere, E_2 Young modulus of flat body, q_1 Poisson's ratio of sphere, q_2 Poisson's ratio of flat body.

Bitter showed that the K value for mild steel is 0.668 m/s. When this value compared to the velocity range considered in the present study (30 m/s to 60 m/s), this constant can be ignored.

The threshold energy is the amount of energy required to be absorbed into the surface layer before the erosion commences. The threshold energy is a function of the number of impact particles. For convenience, threshold energy is defined as the energy spent on a target material till the weight of target material is not less than its original weight. Incubation period [26] is the time period before steady state erosion rate is achieved. The threshold energy of aluminum alloy is 1kJ when impinged by 60-125 micron quartz at impact angles of both 90^o and 40^o [26].

In 1981, Follansbee et. al. [27] considered that the steady state erosion rate is the linear portion of mass loss curve of testing material against the number of impact particles. The erosion rate of ductile material is inversely proportional to its fatigue life and

proportional to the volume undergoing plastic strain. In 1986, Hovis et al [28] showed the steady state erosion rate is a function of particle size. The steady state erosion rate is also affected by the particle flux [29]. As the particle flux increased from 0 to 500 $kgm^{-2}s^{-1}$, the erosion rate is decreased 80%.

Steady state erosion rate is the long term material removal rate which is constant with time, keeping all the other variables constant. Steady state erosion rate is velocity dependent and is expressed as follows [26].

$$E = av_o^{\gamma} \tag{2-15}$$

where E is erosion rate per impact; a, γ are constants, and v_o is the incident impact velocity.

2.8.5 Formation of Craters Due to Normal Impact

A spherical particle impinging normally on a surface of ductile material leads to a uniform formation of crater. This surface texture is closely related to the material removal in the deformation mechanism. In order to understand the formation of crater, Rickerby and Macmillan [30] derived the following equation:

$$p = \frac{mv_o^2}{2\pi.l^2(r - \frac{l}{\varepsilon})} \tag{2-16}$$

$$l = \{\frac{mv_o^2}{2\pi.p(r - \frac{l}{3})}\}^{1/2} \tag{2-17}$$

where l is depth of crater, r is the radius of particle, p is dynamic hardness of surface material, v_o is initial impact velocity and m is the mass of the particle.

The measurement of depth of crater relative to the surface was conducted by profilometer. The diameter of crater, d was determined by following equation:

$$d = 2(2rl - l^2)^{\frac{1}{2}} \tag{2-18}$$

By understanding the relationship between the physical parameter of crater, Rickerby et. al. [30] showed that both the dynamic hardness and static hardness have linear relationship with diameter of the crater.

Other mechanical properties related to the impact event are the magnitude of plastic strain rate as shown below:

$$\dot{\varepsilon} \approx 0.064(\frac{d.v_o}{r.l}) \tag{2-19}$$

where, $\dot{\epsilon}$ the plastic strain rate, d the diameter of crater, v_o the incident velocity of erodent, r the diameter of erodent and l the depth of crater.

Since the plastic strain rate is related to Vickers hardness number which influences the erosive resistance, plastic strain rate is also an important factor in quantifying material removal from the surface. As the number of craters is increased with increasing particle impacts, more and more craters overlaps each other leading to the process of material

removal [30] in deformation with spherical particles. Ricky and Macmillan et. al. [30] summarised the process of material removal stage as follows:

(i) A threshold number of impact below which material removal is negligible.

(ii) The number of impact is more than the threshold value leading more material being removed.

(iii) Linear relationship between number of impacts and material removal regime.

The summary has been validated using erosion tests and a mass loss equation was proposed based on the number of particles impacted. Rickerby and Macmillan [26] derived the equation for particle numbers as follows:

$$\boldsymbol{m_e = b(N_i - N_o(v_o))^{\beta_c}} \tag{2-20}$$

where m_e is mass loss, b and β_c are constant, N_i is number of impact, N_o is threshold number of impact, v_o represent the maximum particle elastic impact velocity.

The total number of impacts, N_i, including N_o, which is the maximum number of impact without erosion and its value is dependent on the velocity. In order to take account for the number of impacts contributing to the mass loss, the term $(N_i\text{-}N_o(v_o))$, where v_o represent the maximum particle elastic impact velocity for number of impact before erosion begun, is determined. The parameters b and β_c are experimentally determined.

Once the steady state is obtained, the erosion rate, E, is given by the linear region of mass loss curve divided by the average mass of impact particle.

During incubation,

$$\boldsymbol{E = \frac{b\beta}{m}(N_i - N_o(v_o))^{\beta-1}} \tag{2-21}$$

During the steady state condition, the erosion rate, E, is defined as the ratio of mass loss of material to average impinged mass of particle. The erosion rate is also proportional to the impact velocity of particle and expressed as:

$$E = av_o^{\alpha} \tag{2-22}$$

where a and α are constants, v_o is the incident impact velocity in m/s and E is erosion rate, gm/gm.

This equation is deduced from the plot of erosion versus impact velocity of particle stream. In Rickerby and Macmillan's experiment, the specimen was pure aluminium and the particulate used was 1.58mm WC-6% Co sphere with mass of 30mg and Vickers hardness number of about 2000 kgf mm^{-2}. The velocity exponent was estimated from equation 2-22.

In summary, the mechanism of material removal at normal impact is to detach the thin platelets created between the overlapping craters. The deformation of crater due to normal impact is evenly distributed around the impact zone. The threshold number of impact is related to the amount of overlapping craters and the amount of strain hardening required for the detachment of platelets from each impact crater. After the threshold number of impacts is reached, the platelets formation is dependent on the degree of strain hardening. At the steady state, the formation of platelets increases at a rate that causes the material removal at a steady state.

In 1982, Rickerby and Macmillan et. al. [30] concluded from their measurement that at a given shallow impact angle, the pile-up of displaced material at exit end of crater is

dependent on the impact velocity of particles. The pile-up of displaced material is developed into shear lip. Also, the rim of crater is irregularly distorted resulting from the random impact of particles. Due to the high impact velocity of particle, the slip lines are observed at the exit end of the crater [31].

Rickerby and Macmillan et. al. [30] related the formation of crater as the material removal mechanism contributing to the mass loss of target material. When the steady state erosion regime is reached, the average mass loss of target material per particle impact remains constant. Individual crater formation is the primary mechanism of materials removal in shallow angle impacts.

2.9 Surface Behaviour Related to Erosion Process

The transformation of liquid to solid metal is done by extracting a large quantity of heat specified by latent heat of fusion. The surface of this solid metal (or surface phase) retains sufficient free energy in order to remain equilibrium with its surrounding crystal. Therefore, the surface phase of solid metal has the tendency to decrease its surface free energy (or surface energy) leading to the absorption of molecules from the interfacing environment at the surface. This absorption layer is not more than a single molecule thickness. The absorbed molecules may be quite stable as a protection layer or unstable leading to a loss of surface material.

The surface wear is dependent on its free energy, morphology and composition of surface phase. For example, the hardness of the surface phase is an indicator of resistance to wear and therefore, the wear is greatly influenced by the surface characteristics. In the case of an air-particle stream impinging on the surface of ductile material, the important parameter for determining surface wear is solid-solid interface

surface energy, which can be expressed as grain boundary energy, stack fault energy and twin boundary energy. These parameters play an important role in explaining the response of mechanical properties of surface material during the erosion process [31].

2.10 Modeling for Present Study

In 1968, with better understanding of the material removal process in erosion, Neilson et. al. [5] simplified the inherent complexity in Bitter's cutting and deformation wear model and presented a model with deformation and cutting energy factor. They argued that the energy for removal of unit amount material remains essentially constant for certain impact conditions and can be considered as material properties. They have also presented the procedure for determination of the energy factors for surface-erodent combinations experimentally.

Based on the understanding of the material removal processes in erosion, Neilson et. al. [5] proposed a simplified model for the erosion of material. They assumed the cutting wear factor ϕ (kinetic energy needed to release unit mass of material from the surface through cutting) and deformation wear factor ε (kinetic energy needed to release unit mass of material from the surface through deformation) and proposed the relationship for erosive wear loss based on the material and process parameters as follows:

$$W = \underbrace{\frac{\frac{1}{2}M(V^2\cos^2\alpha - v_p)}{\phi}}_{(A)} + \underbrace{\frac{\frac{1}{2}M(V\sin\alpha - K)^2}{\varepsilon}}_{(B)} \quad for \ \ \alpha < \alpha_0 \tag{2-23}$$

$$W = \underbrace{\frac{\frac{1}{2}MV^2\cos^2\alpha}{\phi}}_{(C)} + \underbrace{\frac{\frac{1}{2}M(V\sin\alpha - K)^2}{\varepsilon}}_{(B)} \quad for \ \ \alpha > \alpha_0 \tag{2-24}$$

where W is the erosion value, M is the mass of particles striking at angle α with velocity V. K is the velocity component normal to the surface below which no erosion takes place in certain materials and v_p is the residual parallel component of particle velocity at small angles of impact. Part B accounts for deformation wear and part A and C account for cutting wear at small angles of impact and large angles of impact respectively. α_0 is the angle at which the v_p is zero so at this angle both the equations will predict the same erosion.

The calculation of energy factors had been given by Neilson et. al. [5]. In their calculation procedure, the value of K is ignored as the velocity for elastic impact is very small compared to the impact velocity considered in erosion tests.

2.11 Energy Factor

Energy factors are related to the energy of erodent absorbed into the surface that generates mass loss from the target material [7]. The mass loss of target material remains constant when eroded by a constant mass of solid particles at steady state conditions. The steady state of erosion is established when the mass loss from the surface is proportional to energy of solid particle transmitting to the target material. The energy of solid particle transmitted to the target material is dependent on the particle shape, velocity and hardness of solid particle, as well as the hardness and intrinsic ability of the target material to absorb energy [32].

2.11.1 Deformation Energy Factor

The energy needed to remove a unit volume of material from the surface by deformation wear is termed as deformation energy factor [7]. The absorbed energy of deformation wear is to indicate the level of ability to deform or the brittleness of the material. Bitter [7] concluded that the deformation energy factor includes a series of elasto-plastic deformation process as well as the actual material removal. In the case of metal, the energy for material removal is negligible in the elastic deformation process. The energy for plastic deformation is absorbed in the form of lattice distortion and liberated as heat as a result of re-crystallization.

2.11.2 Cutting Energy Factor

Cutting energy factor is the amount energy needed to scratch out a unit volume of material from the surface. The material cutting energy is equivalent to the hardness of material or yield strength of material [23]. The cutting and deformation energy factors will be discussed in detail in Chapter 5.

Chapter 3

EXPERIMENTAL METHODOLOGY

3.1 Introduction

This chapter describes the experimental setup used to conduct the erosion experiment in this study. The main objective of the experiment in this study is to analyse the erosion performance of ductile materials under the impingement of solid particles at different impact velocity and angle. The study involves quantitative analysis of mass loss from the surface as well as visual analysis of the surface morphology and associated wear mechanisms.

3.2 Experimental Setup

The erosion experiments presented in this study is conducted on flat surface of ductile material with impact velocity up to 60 m/s at different erosion conditions shown in Table 3-1. They are subdivided into four columns. The first and second column is the material and abrasive particle. The third and fourth column describes the erosion condition.

Table 3-1: Erosion condition of erosion experiment

Material	Abrasive particles	Impact velocity, v, of solid particle with respect to surface material, in m/s	Impact angle, θ, of impact particles, in degree
Aluminium and mild steel	Alumina, ilmenite	60	90, 45, 30
		50	90, 45, 30
		30	90, 45, 30

The expected experimental results include:

(1) The mass loss from impacted surface as a function of erosion parameters and time.

(2) The determination of steady state erosion rate.

(3) The determination of deformation and cutting energy factor.

(4) Surface analysis for wear mechanisms

The erosion experiment was conducted according to the procedure described in ASTM G76-07. The objective of erosion test is to determine the mass loss of target material impacted by different solid particle-laden air stream. Figure 3-1 shows the micro-sandblaster being used in this study.

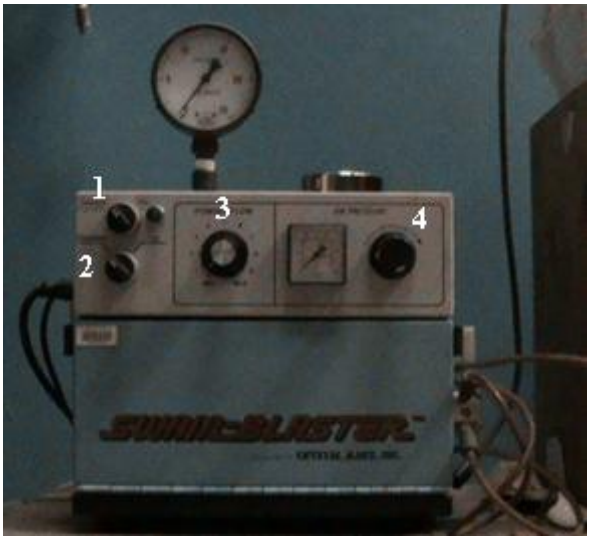

Figure 3-1: Photograph of the micro-sandblaster model "MV-2 SWAM-BLASTER" from Crystal Mark, inc.

The micro-sandblaster allows the flow control of solid particles and air pressure independently for conducting the experiment at different flowing velocity of particle

stream through controlling air pressure as well as different mass flow rates through flow control knob on the apparatus. In Figure 3-1 the label '1' shows the switch to allow the particle stream 'on' or 'off'. The label '2' is the power switch. The label '3' adjusts particle flux independent of the air pressure. The label '4' adjusts the particle velocity through air stream pressure control.

The mixing chamber controls the particle flow rate independent of the air pressure through pressure equalisation of the particle chamber of the instrument. A schematic of the mixing chamber is presented in Figure 3-2 shown below:

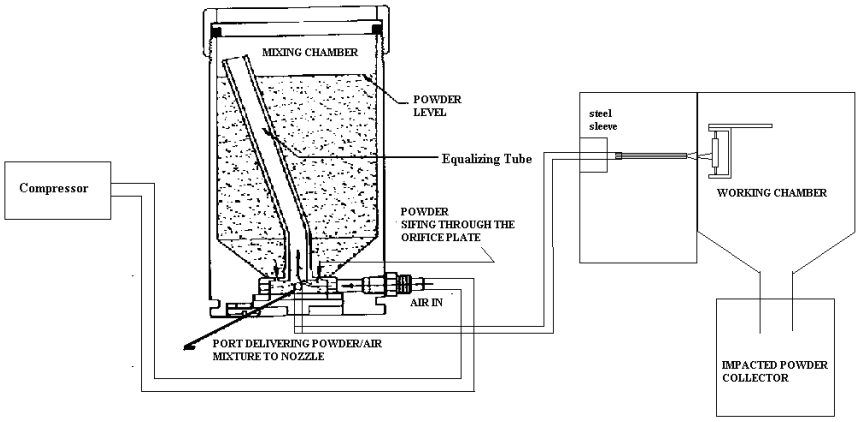

Figure 3-2: The schematic diagram of the solid particle erosion testing equipment (not to scale).

According to the standard, the nozzle length to diameter ratio is 25:1 for achieving even distribution of particles across the air-particle stream. The target specimen can be adjusted at different angles with respect to the axis of the air-particle stream using a sample holder attachment.

The acceleration nozzle used in these tests was 40mm in length with internal diameter about 1mm. The length to internal diameter ratio is 40:1. It is greater than the standard

requirement 25:1. The nozzle is manufactured from erosion resistance tungsten carbide. The erosion of the nozzle is monitored during testing to ensure the wear is less than 10% of the internal diameter of the nozzle.

Procedure to calibrate the instrument for particle velocity with respect to air pressure as well as the variation of particle velocity with mass flow rates are described in sections below.

3.3 Test Materials and Erodent

Erosion experiment conducted in this study is to analyse the wear characteristics of ductile materials, which was selected as mild steel and aluminium. The test samples were cut from the same long strip for the uniformity of the specimen. The size of the specimen was approximately 10mm x 30mm x 2mm.

The abrasive particles selected were hard materials with different angularity and these were alumina and ilmenite. Ilmenite particles are apparently angular in general, but the SEM image showed that particles have spherical asperity. The selected size range of alumina was 63-125μm with average particle size about 75 μm. and the selected size range of ilmenite was 63-180 μm with average particle size being 125 μm.

The conveying air used in the experiment was dry. The impact velocity of abrasive particle was in a range of 30± 3 m/s and 60± 3 m/s. The range of compressed gas pressure in the mixing chamber is between 34.5 kPa and 103kPa.

The air-particle stream impacted on the central portion of specimen. The specimen was installed at different angles with respect to the axis of air stream. The particle stream velocity was adjusted through controlling the air pressure. Calibration of particle

velocity with air pressure was conducted prior to the erosion experiment using the double disk method. Maintaining the steady flow of solid particle is also essential for successful measurement of the particle energy delivered to the eroding surface. The method of measuring the impact velocity of solid particle is presented in the section below.

3.4 Measurement of the Particle Velocity in Gas Stream

There are number of methods available to measure the particle velocity in gas entrained particle stream in the literature. These include opto-electronic detector [33], multi-flash photography [34], laser Doppler [35] and rotating double disk [36] methods.

3.4.1 Experimental Method for Measuring Particle Velocity

In 1993, Shipway and Hutchings conducted a test for measuring impact velocity of solid particle in a gas-blasting stream [34]. They measured the impact velocity of particles using an opto-electronic flight-timer. A simplified diagram of the instrument used by Shipway and Hutchings is shown in Figure 3-3.

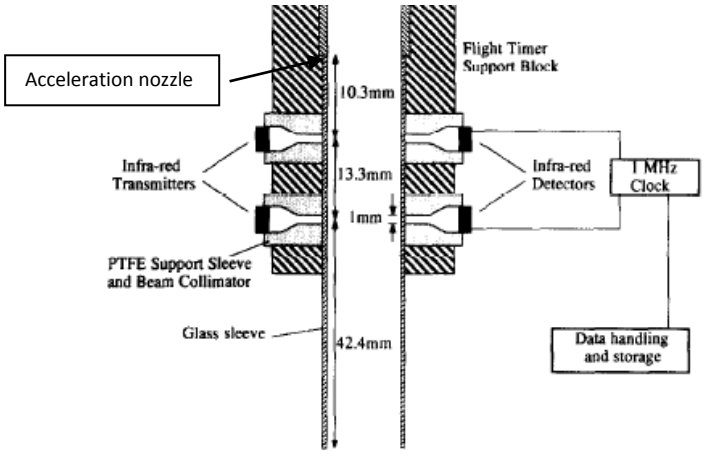

Figure 3-3: Arrangement for measuring the particle velocity in gas stream [24, 33].

Shipway attached the velocity sensors on the wall of a glass tube which was connected to the exit of acceleration nozzle. The velocity sensors were two pairs of infra-red emitters and detectors situated at different distances from the exit of glass sleeve. As the particles passed through both light beams, the velocity of the particles was determined from the time of flight.

In 2004, Deng et. al. [34] employed multi-flash photography as a method of measuring the particle velocity in a gas stream blasting out from the centrifugal accelerator erosion tester. Dent installed a standard 35mm multi-flash camera with a long view lens and focused on the particle stream exiting from the rotating disk of erosion tester. In order to have a clear image, four Vivitar 286 flashguns were triggered as the photographs were taken. The photographs were taken at different flash intervals in the range 20-100μs at the time all flashguns were being triggered.

In 1975, Ruff et. al. [36] derived a formula to determine the particle velocity in a gas stream at a specific distance from the accelerating nozzle exit. This method is more efficient and direct for measuring the particle velocity at a particular impact point. The installation procedure is also simple as compared to the multi-flash method or using an opto-electronic flight timer.

The rotating double disc method was employed to measure the impact velocity of particle in the present study. Figure 3-4 illustrates the setup of the nozzle and the discs for measuring the impact velocity of the particle.

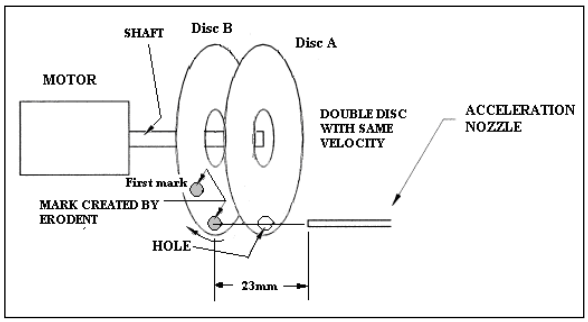

Figure 3-4: Schematic of double disc method for particle impact velocity.

In the double disc method, the particles velocity is measured from the flight time between the two fixed rotating discs. The two discs mounted on a shaft are rotated by a motor at a known speed. The particle accelerating nozzle is fixed on the other side as shown in the diagram. There is a hole in the disc A in front of the nozzle for the particles to pass through. There is a fixed mark on Disc B, directly opposite to the hole in the disc A. When the shaft is rotated at a high speed, particles passing through the hole on disc A will hit disc B somewhere down on the path. A mark is created on the aluminium foil stuck on the surface of disc B from the particle impacts. From the linear distance between the fixed mark and the new mark on Disc B, the particle velocity can be determined through the following equation 3-1.

$$v = \frac{2\pi R\omega L}{S} \tag{3-1}$$

where,

R is the radial distance of the marks on the disc B in m,

ω is the rotation rate in revolution per second.

L is the two disc separating distance, kept constant and

S is the linear distance between two marks on the disc B measured after the test.

The following Figure showed the arrangement of the nozzle and the discs in the chamber.

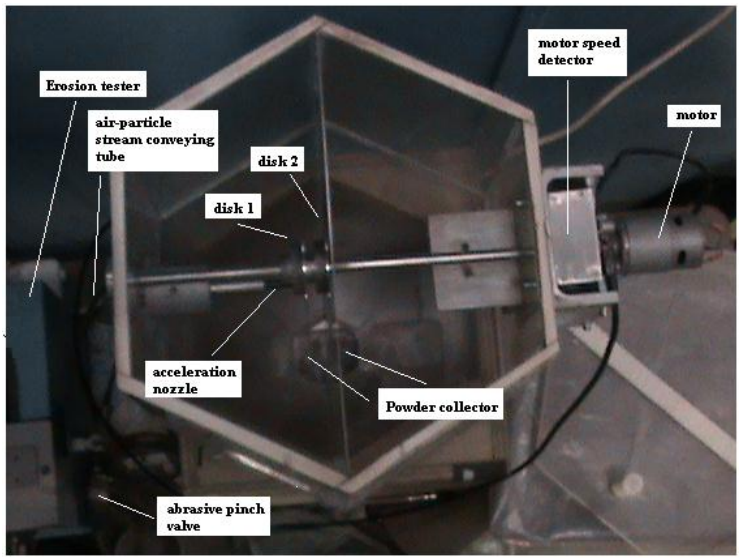

Figure 3-5: The Disc chamber for measurement of particle velocity in a gas stream.

The particle velocity increases with increasing air pressure. Calibration of the particle velocity with incremental pressure was conducted for the test pressure range. The impact velocity of solid particle with expanding air stream in the mixing chamber of the erosion tester was conducted as presented below. It is evident that the smaller particle alumina was accelerated faster than the larger particle ilmenite.

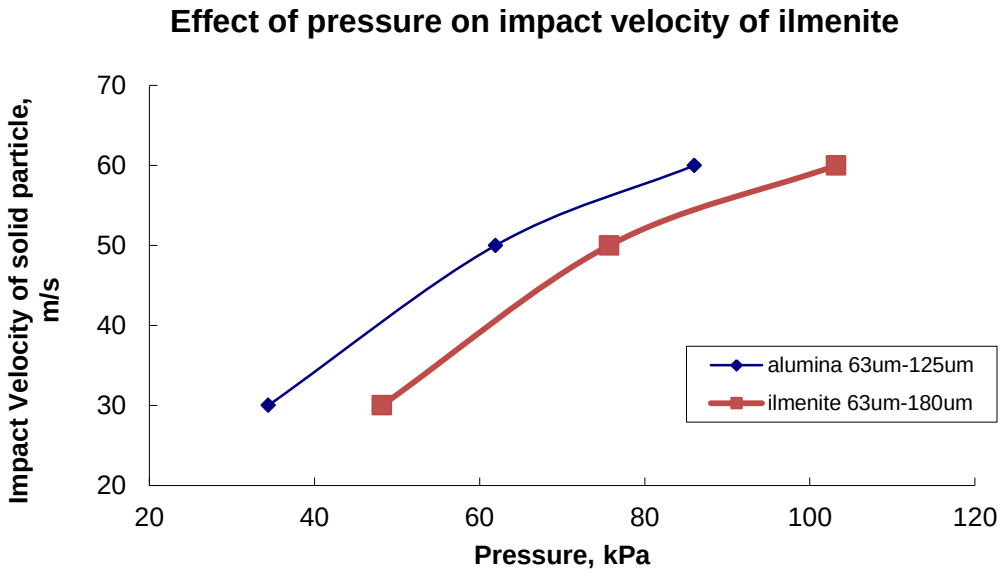

Figure 3-6: The relationship between the compressed air pressure and impact velocity of solid particles at a distance of 23 mm from exit of accelerating nozzle within the mass flow rate range of 0.1 and 0.2 gm/sec.

The relationship between compressed air pressure and impact velocity is shown by the curves above. The mass flow rate of erodent is maintained at a value of between 0.1 and 0.2 gm/second.

3.4.2 Analysis of the Erodent Particles

Erosion experiments were conducted using alumina and ilmenite particles to determine the energy factors of aluminium and mild steel for the predictive model in this study. Description and procedure to determine the energy factors will be presented in Chapter 5.

The study also analysed the influence of particle variables on the erosion rate and the material removal mechanism in ductile materials. Aluminum and mild steel are ductile metals. The crystalline structure of aluminum is face-centered cubic. The commercially pure aluminum is commonly 99.50-99.79% of aluminum (AL 1100-o) [37]. The crystalline structure of mild steel is body-centered cubic. The commercial mild steel is commonly 0.05% - 0.25% of carbon [37]. Aluminum has a softer surface than that of mild steel.

Aluminum oxide is classified as ceramic. Aluminum oxide in alumina particle is from 85% to 99%. Ilmenite is a component of mineral sand. The chemical formula of ilmenite is iron titanium oxide ($FeTiO_3$). Ilmenite is classified as the cation-anion (metal-nonmetal) hexagonal close-packed crystalline structure [37].

The SEM images of abrasive particle clearly revealed the primary difference between these two particles. The Figure 3-7 show the SEM images of the particles as well as the particles size distributions in Figure 3-8. The physical properties and conveying condition are given in Table 3-2.

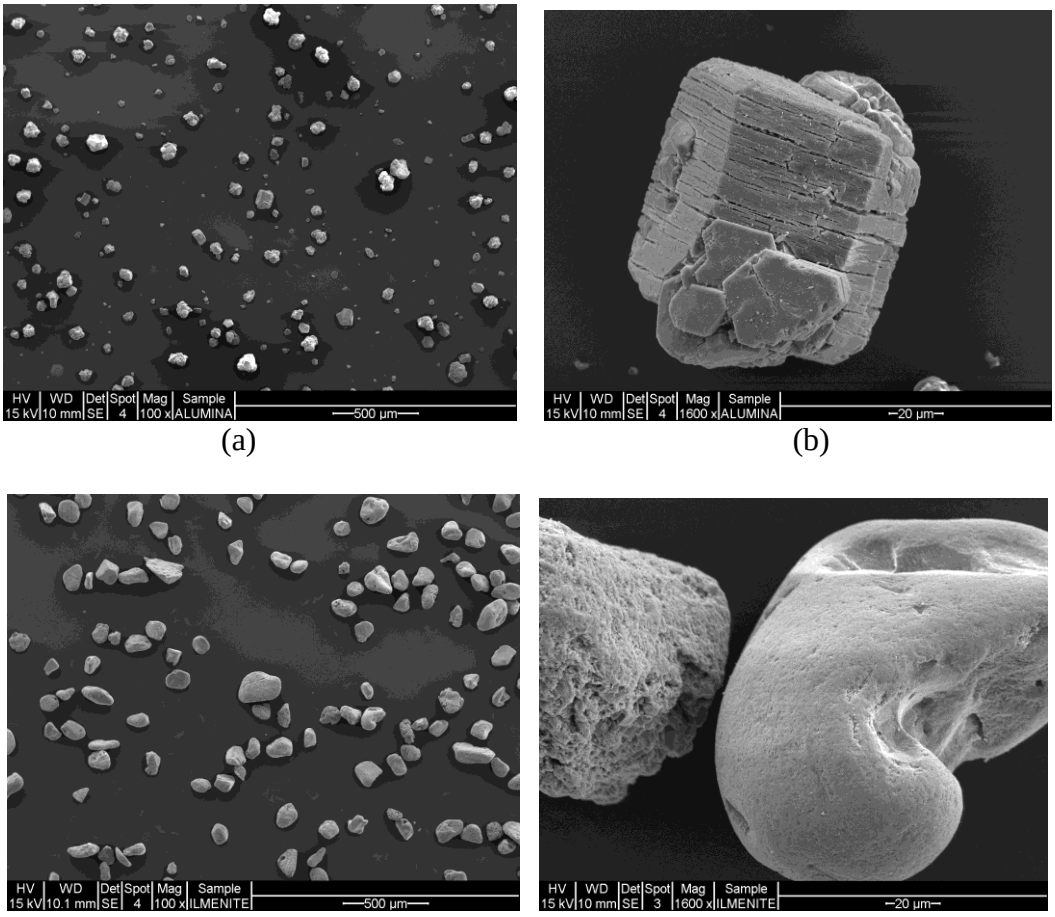

(a) (b)

(c) (d)

Figure 3-7: SEM observation of size and shape of alumina (a) x100 (b) x1600; of ilmenite (c) x100 (d) x1600.

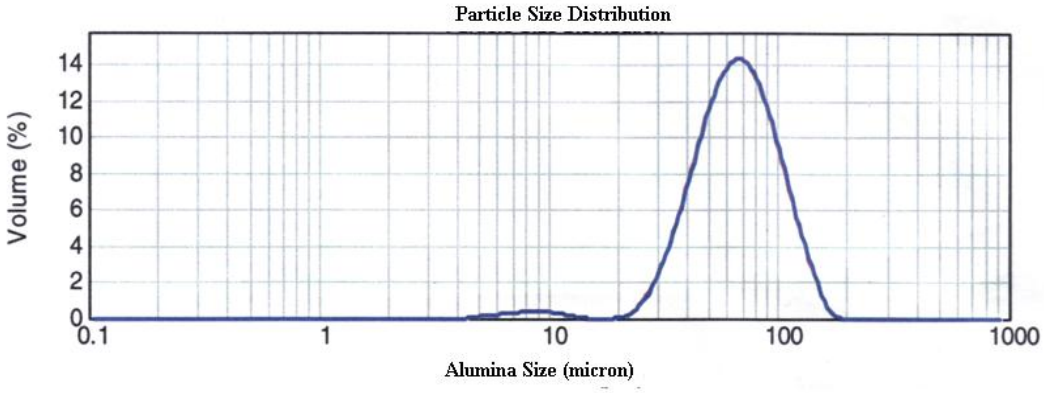

(a)

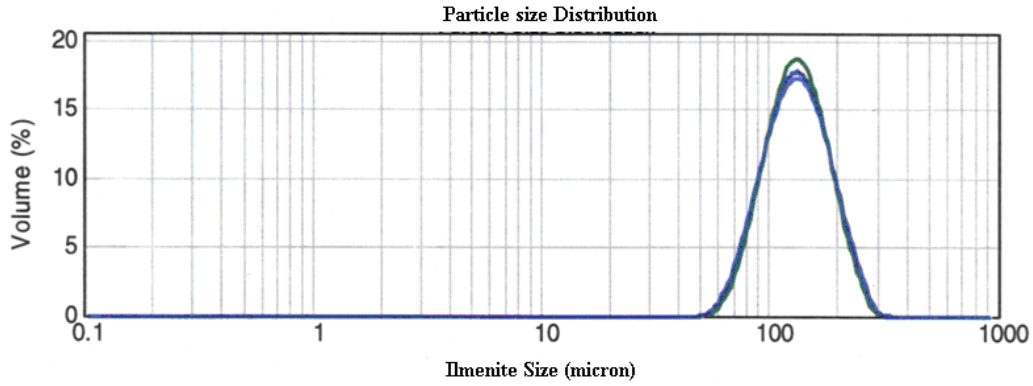

b)

Figure 3-8: The particle size distribution measured by Malvern Mastersizer laser particle analyzer, (a) alumina and (b) ilmenite.

Table 3-2: Mechanical properties and erosion parameter

	Alumina	ilmenite
Erodent bulk density	3766 kg/m^3	4352 kg/m^3
Erodent size range (µm)	65µm-125µm	65µm-180µm
Erodent hardness(mohr)	9(mohr), 2000 (Knoop)	5-6(mohr), 300-500 (Knoop)
Erodent shape	Less angular edges	Irregular, more angularity
Impingement angle (α^0)	30^o, 45^o, 90^o	30^o,45^o,90^o
Impact velocity (m/s)	30 ± 10, 60 ± 10	30 ± 10, 60 ± 10
Nozzle to sample distance(mm)	21 ± 2	21 ± 2
Erodent feed rate (g/min)	10.2 ± 0.6	10.2 ± 0.6
Test temperature	Room Temperature	Room Temperature
Nozzle diameter(mm)	1 ± 0.5mm	1 ± 0.5mm

3.5 Test Procedure

The specimen was mounted on the sample holder at the location where the impact velocity of the solid particle in an impacting air stream had been measured. The specimen holder has been designed to rotate the specimen at small angles with respect to the axis of particle stream from the nozzle.

Depending on the erosion performance of the specimen, the measurement period was varied between 3 minutes to 2 hour. At a fixed interval of time, the sample was removed, cleaned and weighed. The particle impacted on the surface for test duration was also collected, weighed and recorded for calculations later on.

The following schematic showed the positions of the specimen with respect to the air-particles stream for impacts. For the deformation erosion, the impact angle of particle stream is defined at 90^0 (Figure 3-9(a)) whereas for oblique impacts, the specimen is placed at any desired angle with respect to the particle stream as shown in Figure 3-9(b).

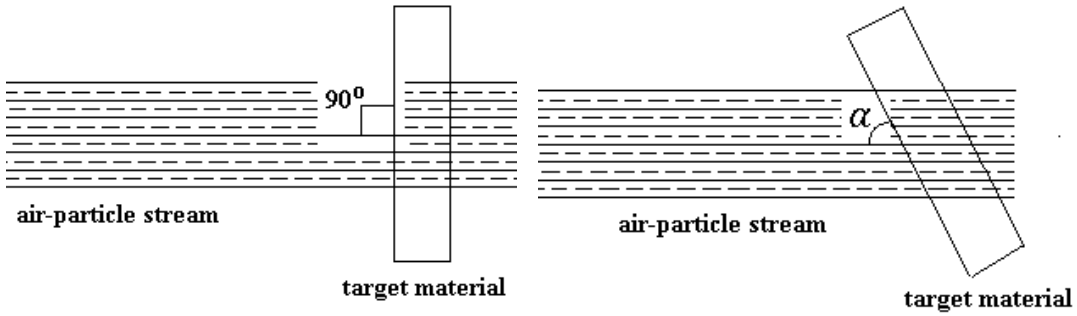

(a) (b)

Figure 3-9: Schematic of the particle impacts arrangement (a) normal impact (b) oblique impacts.

3.6 Determination of Steady State Erosion Rate

As mentioned before, erosion tests were performed using two different particles, namely alumina (Av. 70μm) and ilmenite (av. 130μm) on a micro sandblaster, model SWAM_BLAST® MV-2L from Crystal Mark Incorporated (Figure 3-1). A specialized chamber (Figure 3-5) was designed to enable the specimen to be in a controllable testing

condition as well as to collect the solid particles impacted on the specimen. The investigation of the erosion rate was carried out at the abrasive particle velocity of 30m/s, 50m/s and 60 m/s and the impact angle range was 0-90^{o}. The particle velocities were also calibrated for different mass flow rates as well as pressure conditions. Calibration of particle velocity using the double disc method has been presented earlier. Erosion rate was determined from the weight loss of target material and mass of impacted abrasive particle. The mass loss of target material was measured by weighing at an accuracy of 0.1mg.

Initial measurements were repeated until the threshold amount of particles for each combination of surface and particles has been impacted or constant mass loss was achieved. The linear portion of cumulative mass loss of target material versus cumulative mass of impinged erodent curve determines the steady state erosion rate.

The blasted area of the specimen is located completely on the flat surface of the specimen. In order to observe deformation and cutting erosion, the specimen was maintained at different angles with respect to the axis of the air-particle stream. Finally the erosion rate was determined as:

$$\text{erosion rate} = \frac{\text{change in mass of sample}}{\text{mass of impacting particles}} \tag{3-2}$$

Based on the models presented by Neilson et. al. (1968) [5], the target materials have been further analysed for the energy factors due to deformation and cutting mechanisms. The cutting wear factor ϕ (kinetic energy needed to release unit mass of material from the surface through cutting) and deformation wear factor ε (kinetic energy

needed to release unit mass of material from the surface through deformation) [7] have been determined according to the proposed relationship for erosive wear loss presented as:

$$W = \underbrace{\frac{\frac{1}{2}M(V^2\cos^2\alpha - v_p)}{\phi}}_{(A)} + \underbrace{\frac{\frac{1}{2}M(V\sin\alpha - K)^2}{\varepsilon}}_{(B)} \quad for \ \ \alpha < \alpha_0 \tag{3-3}$$

$$W = \underbrace{\frac{\frac{1}{2}MV^2\cos^2\alpha}{\phi}}_{(C)} + \underbrace{\frac{\frac{1}{2}M(V\sin\alpha - K)^2}{\varepsilon}}_{(B)} \quad for \ \ \alpha > \alpha_0 \tag{3-4}$$

where, W is the effective material removal in an erosion process in kg after impinged by a quantity of mass, M in kg, of solid particles at an acute or right angle, θ, with respect to flat surface of the specimen in degree with an impact velocity, *V*. K is threshold velocity under which no permanent deformation occurs on the surface. v_p is zero as impact angle of solid particle is α_o so that at this angle both the equations will predict the same erosion. Part *B* accounts for deformation wear and part *A* and *C* account for cutting wear at small angles of attack and large angles of attack respectively.

Finally the eroded samples were observed through optical and scanning electronic microscope (SEM) for analysis of the dominant wear mechanisms on the surface. Chapter 4 and 5 provided the detailed description of experimental results and evaluate the erosion performance of specimens under the influence of erodent parameters described in this chapter.

Chapter 4

EXPERIMENTAL RESULT

4.1 Introduction

In Chapter 3 the surface material and erodent, experimental procedure and parameters have been presented. In this chapter the experimental results are presented in detail with emphasis on erodent variables for the wear performance. The objectives of the chapter can be summarised as follows:

1. To analyse the steady state wear rate for different erodent and surface materials selected.
2. To study the dominant wear mechanism in ductile materials for different erodent and impact parameters.
3 To determine the energy factors for the surface-erodent combination selected for the study.

4.2 Determination of Steady State Wear Rates of Ductile Materials

Ductile material, such as aluminium and mild steel, are widely used because of its low cost and good erosion-corrosion resistance. The best way to develop better understanding of the wear characteristics of these materials is to study these materials under a known condition for their behaviour and relationships with wear parameters.

In this section the steady state erosion rates have been determined using the test rig and experimental procedures described in Chapter 3.

To establish the steady state wear, different surface-particle combination needs different amounts of particles to be impacted on the surface. This phenomenon has been discussed in detail in Chapter 2. Before the steady state condition is achieved, the initial period of testing is called the incubation period. The material removal from the eroded area is very low at the beginning and then increases until the steady state erosion is achieved. In some cases, the sample weight increases due to the embedded particles in the sample. Once the threshold number of particles has been impinged on the surface, steady state erosion can be established.

Figures 4-1 and 4-2 present the mass loss from aluminium and mild steel surfaces eroded by alumina at 60 m/s. The measurements were undertaken with the precision of 0.1mg. The data were recorded until the steady state was achieved.

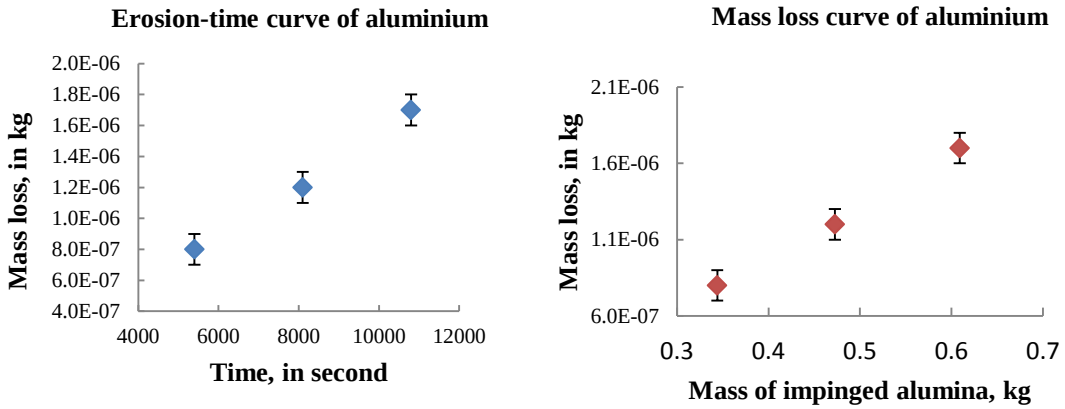

(a) (b)

Figure 4-1: Variation of mass loss with time and impinged mass of alumina with 60 m/s for aluminium under 90^{o} impact. (a) mass loss variation with time (sec) and (b) mass loss variation with particle mass.

Figure 4-1(b) showed that more than 300gm of alumina was impacted before the steady state erosion was established. The steady state erosion rate was achieved after the sample weight gain due to the particle deposition on the surface had stabilised. Slope of the mass loss of surface material with respect to the mass of impinged particle showed a linear relationship. The steady state erosion rate of 3.4 x 10^{-6} kg/kg has been calculated from the experimental data for aluminium.

Figure 4-2 showed the measured mass loss with time and particle impacted for mild steel eroded by alumina with 60 m/s. The curves show a similar trend as aluminium but with lower erosion rate for mild steel. An erosion rate of 1.6 x 10^{-6} kg/kg was calculated from the graph for mild steel.

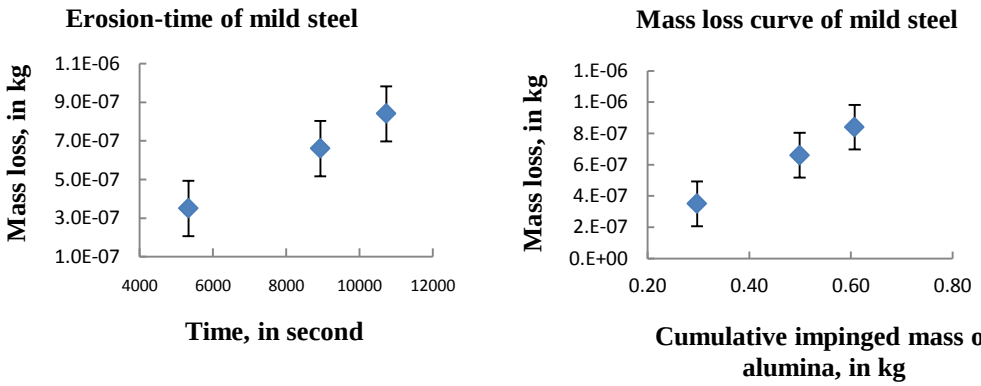

(a) (b)

Figure 4-2: Variation of mass loss mild steel impacted by impinged at 60 m/s at 90^{o} (a) variation with time, (b) variation with mass of erodent.

Figure 4-3 shows the steady state wear rates on aluminium and mild steel eroded by alumina at different angles of impact and particle velocities. The curves have been derived from the similar data sets for aluminium and mild steel eroded at 90^{0} presented in Figures 4-1 and 4-2.

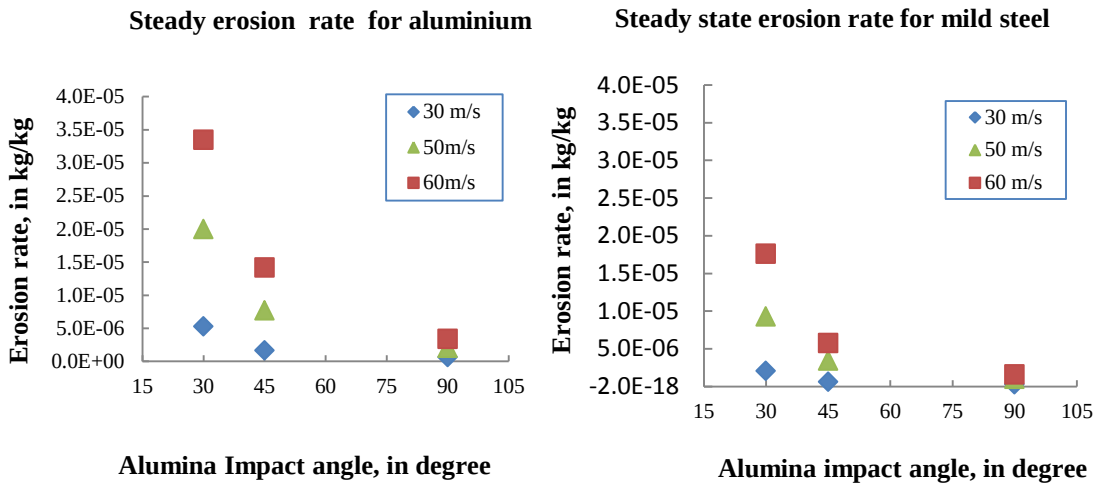

(a) (b)

Figure 4-3: Steady state erosion rate of (a) aluminium and (b) mild steel.

As expected for ductile materials, both mild steel and aluminium showed the minimum wear rates for normal impacts. The maximum erosion was recorded for 30^0 impact angle for both the materials with sharp decrease at 45^o and a minimum at 90^0. This is primarily due to the transition of material removal mechanism from purely deformation at normal impacts to a combination of cutting and deformation at oblique impacts. For ductile materials cutting is the most efficient mechanism for material removal. This is demonstrated through the maximum erosion rate at around 30^0 where the particles are more efficient in energy transfer to the surface.

The variation of mass loss on aluminium with test duration and with mass of ilmenite erodent is presented in Figure 4-4(a) and 4-4(b) respectively. It has been shown that the mass loss increases linearly with increasing time and mass of erodent. Rate of erosion has been calculated from the slope of the mass loss curve with mass loss of erodent. Erosion rate of alumina with ilmenite has been recorded as 46.1 x 10^{-6} kg/kg for 60 m/s for normal impacts. Comparing the erosion characteristics of aluminium eroded by

alumina and ilmenite, the threshold mass of ilmenite is considerably lower than alumina; less than 200gms was required to attain the steady state erosion in this case. This is due to the fact that the number of embedded particles is less for ilmenite due to low particle attrition.

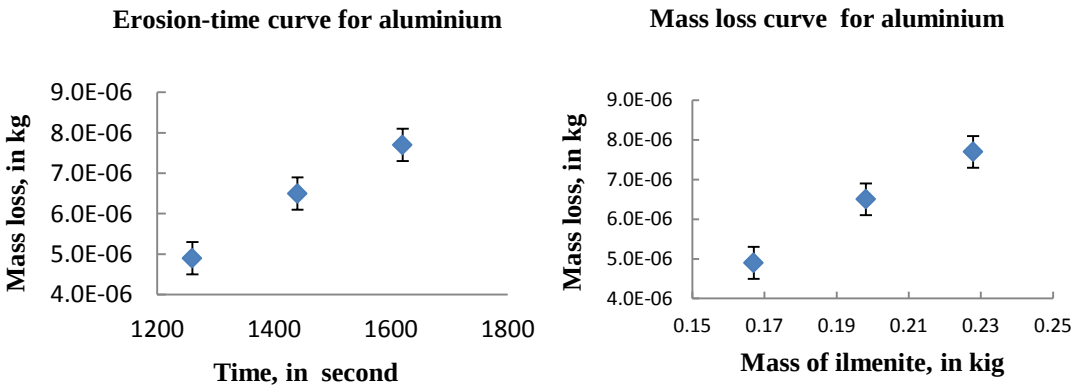

Figure 4-4: (a) Erosion-time curve for aluminium impinged by ilmenite with 60 m/s at 90^{o}, (b) Variation of mass loss with mass of ilmenite with 60 m/s for aluminium under 90^{o} impact.

Figure 4-5 presents the mass loss of mild steel eroded by ilmenite with 60 m/s at 90^{0} impact angle. Similar to the test results of aluminium, the erosion rate increased linearly with increasing the test duration and the mass of erodent impacted on the surface. The steady state erosion rate was attained with less than 140gms impacted at this speed. The steady state erosion rate for mild steel was 38.9 x 10^{-6} kg/kg for 60 m/s at normal impact.

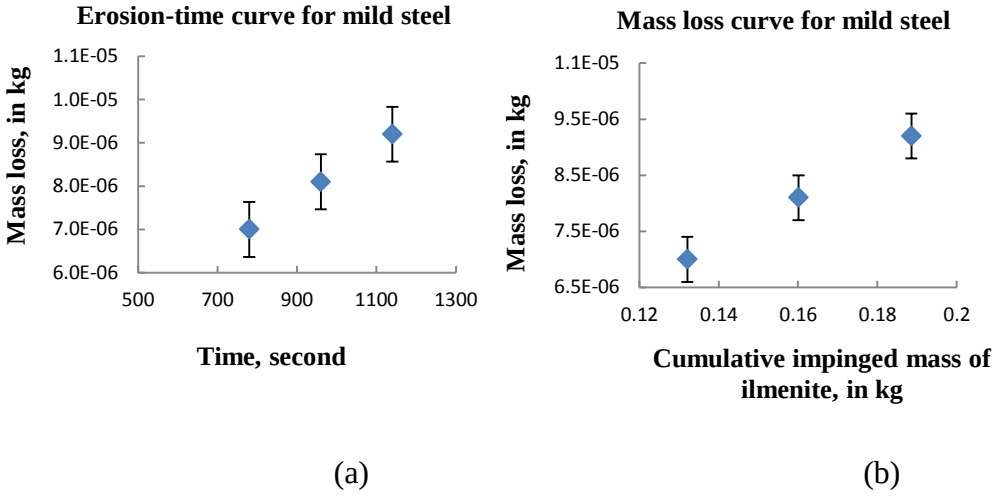

(a) (b)

Figure 4-5: (a) Erosion-time curve for mild steel impacted by ilmenite, (b) Variation of mass loss of mild steel with cumulative mass of ilmenite.

Figure 4-6(a) and Figure 4-6(b) show the steady state erosion rate for aluminium and mild steel eroded by 63-180μm ilmenite at different angles and impact velocities. It was observed that for all impact angles, the erosion rates for 60 m/s were considerably higher than that with 30 and 50 m/s. The variations in wear rates for all impact angles between 30m/s and 50 m/s have been relatively small.

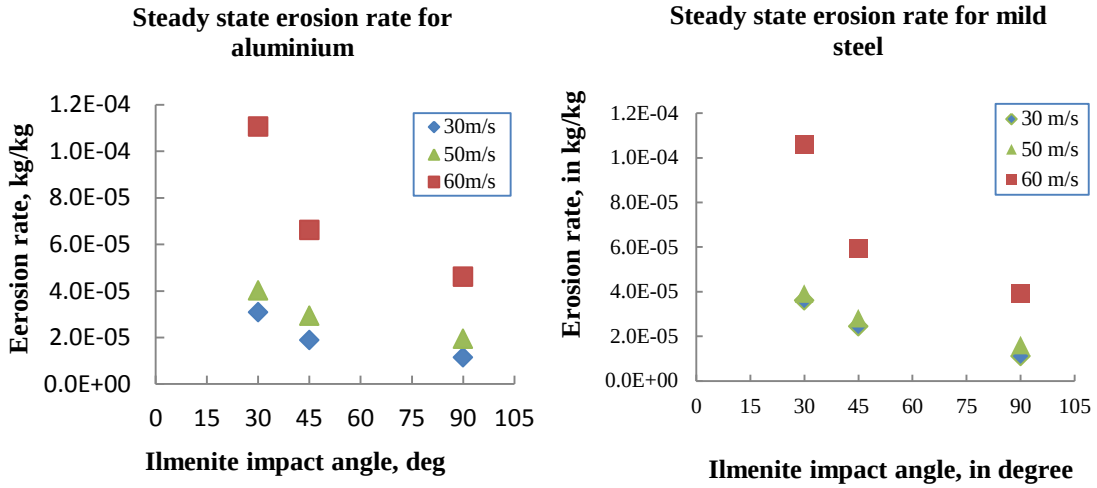

Figure 4-6: Steady state erosion for (a) aluminium (b) mild steel at different impact velocity of ilmenite.

Figures also showed that the steady state erosion rate of aluminium and mild steel decreases rapidly from 30^0 to 45^0 and more slowly after that reaching to a minimum at normal impact. This is significant as the erosion rate changes from dominantly deformation at higher impact angles to dominantly micro-cutting at shallow impact angles as the impact angle reduces to less than 45^o where micro-cutting is the dominant mechanism.

Comparing the Figures 4-1 and 4-4, erosivity of ilmenite is higher than that of alumina due to the particle integrity and the ability of the particle to penetrate the surface. The different amount of cumulative mass of alumina and ilmenite particles were required to achieve the steady state wear at different velocities and impact angles. This is probably due to two reasons:

(a) The mass of alumina fragments deposited in the sample is more than the mass of materials actually removed for the surface.

(b) During the incubation period, the onset of material removal is more for alumina due to particles disintegrating during impact.

4.3 Effect of Impact Angle on Erosion Rate

The mass removal at oblique angle is considered to be primarily due to cutting although considerable deformation is expected depending on the angle of impact and the surface material properties. For ductile materials, cutting wear is attributed as the primary contributor to the material removal. It was observed that the threshold amount of alumina for obtaining steady state mass loss was different for mild steel and aluminium as well as for different angle of impacts and particle velocities. Hence, for steady state wear behaviour of material and the impact condition must be understood before analysing any erosion results.

Erosion results for different erodent and different surface materials have been compared from Figure 4-1 to 4-9 to analyse the effects of particle characteristics. Both the alumina and ilmenite are hard materials with different angularity and surface integrity. Alumina has sharp edges that can damage the surface easily, yet their agglomerated nature made it vulnerable to particle attrition and reduces wear. On the other hand, corners and edged of ilmenite are smooth and rounded, making it inefficient to cut into the surface, especially at low impact angles. Overall, ilmenite produces more surface damage (higher erosion rate) compared to alumina at all the impact angles and velocities due to its integrity.

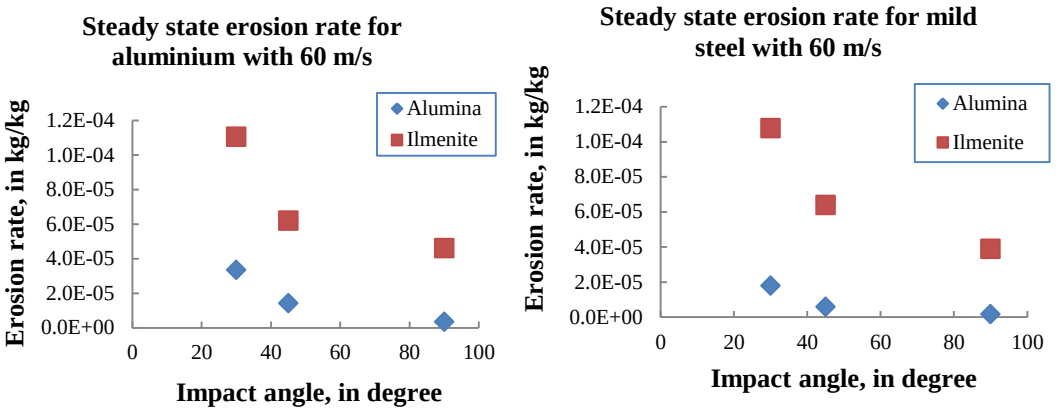

(a) (b)

Figure 4-7: Variation of steady state erosion rate for (a) aluminium, (b) mild steel impinged by solid particle with 60 m/s at different impact angle.

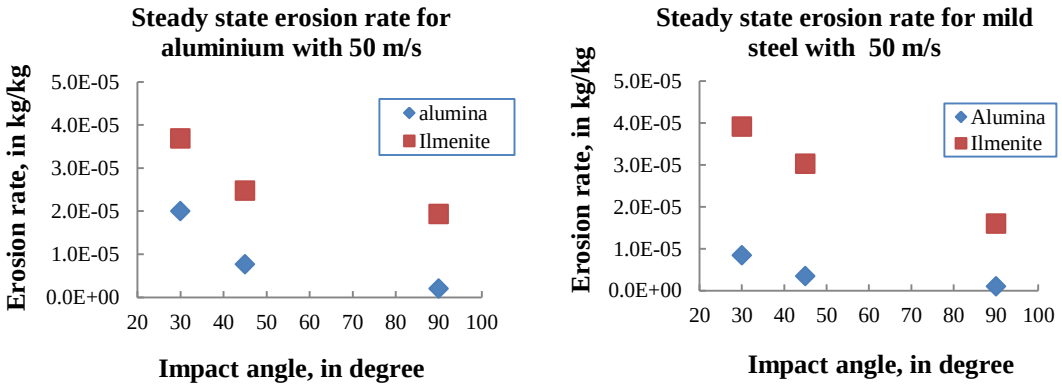

Figure 4-8: Steady state erosion rate for (a) aluminium, and (b) mild steel after impinged by solid particles with 50 m/s at different angles.

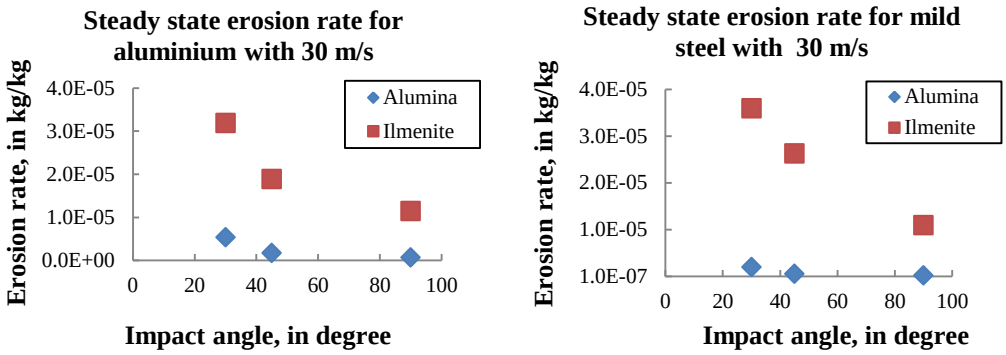

Figure 4-9: Steady state erosion rate for (a) aluminium, and (b) mild steel after impinged by solid particles with 30 m/s at different angles.

4.4 Observation Morphology of Eroded Surface

The mild steel and aluminium based surfaces eroded by two different erodent materials have been discussed in the previous sections. The wear surfaces are analysed in this section to determine the dominant wear mechanisms in these materials in different wear situations. The difference in wear rate for different wear situation means the wear mechanisms have changed. Recognising dominant wear mechanisms and relating them to the rate of wear hold the key to the development of predictive models for wear in any industrial applications.

The primary surface characteristics in ductile materials have been discussed in Chapter 2. In this sections those surface characteristics and the underlying wear mechanisms will be discussed with respect to the wear parameters and relate them with the material removal rates discussed in the previous section.

A surface texture indicating plastic deformation is a common surface characteristic founded on worn surfaces of ductile material eroded by solid particles. These characteristics are expected from the known material removal mechanisms. Extensive surface deformation that led to ripple formation, formation of subsurface cracks and crack propagation and material loss by flaking are primary concerns of this section. Thus the aim of this section is to study the eroded surface and analyse how the wear mechanism affects the wear rate.

4.4.1 Alumina Surfaces Eroded by Alumina and Ilmenite

The general characteristics of aluminium eroded by alumina are present in the Figure 4-10 for different wear conditions. Figures 4-10 (a)-(c) presented the surfaces for 30m/s and Figures 4-10 (d)-(f) presents the surfaces worn at 60 m/s. In general, the wear surfaces are characterised by the development of ripples. Even though ripples are not expected to form at normal impacts, in these tests, ripple-like structures are clearly visible at all velocities and angles of impact. For normal impacts in Figure 4-10(a), ripples are formed as concentric circles moving in an outward direction at 30 m/s, whereas, at 60 m/s, they are formed as radial rays emitting from the centre (Figure 4-10(d)). At slower velocities, ripples seem to be more uniform compared to that at higher velocities. The ripples seem to be larger in amplitude and less uniformly distributed over the surface largely due to the greater depth of deformation. Ballout et al [38] suggested that the tangential velocity of impacting particles led to the formation ripples on the eroded surface.

Formation of ripples in normal impacts can be explained from analysis of the particle flow after impact. As the particles rebound from the initial impacts, due to interaction with the oncoming particles, particles tend to flow outwards along the surface. Particles

flowing parallel to the surface being further impacted by the normal particles create randomly oriented pits which eventually take the pattern of ripples. At higher velocity, the escaping particle forms preferential channels along the surface that possibly generate the ripple patterns emanating outwards from the centre of impact.

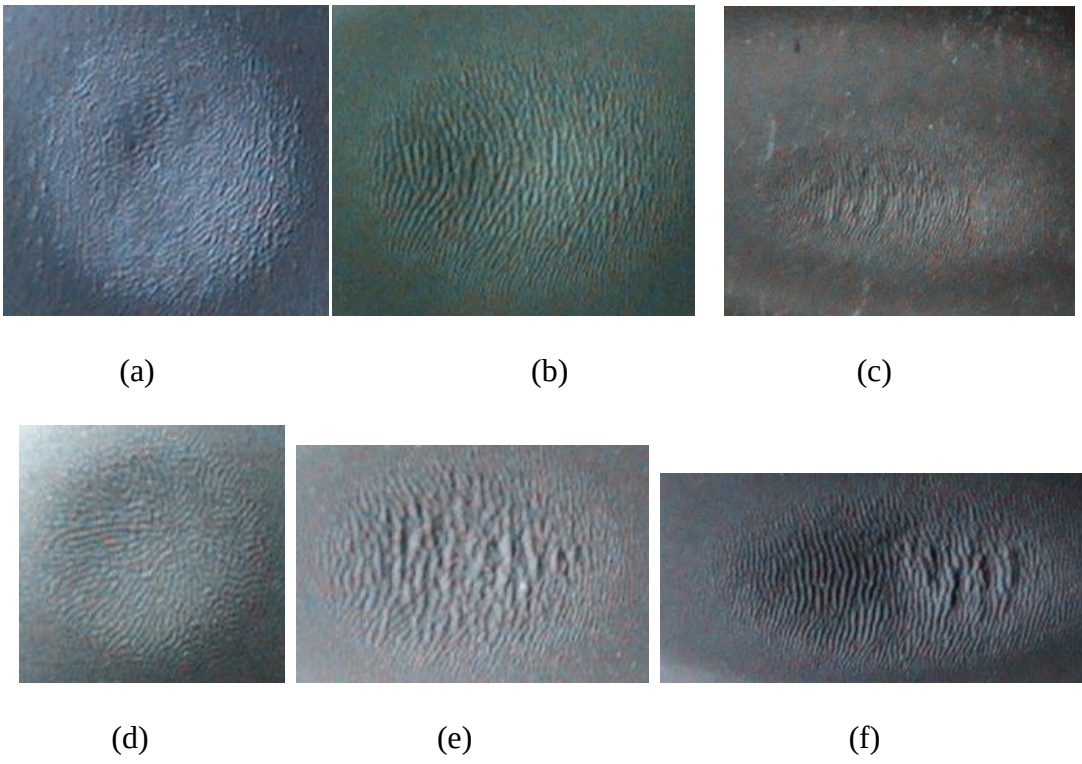

(a) (b) (c)

(d) (e) (f)

Figure 4-10: Aluminium eroded by alumina with 30 m/s at (a) 90^{o} , Er = 6.28×10^{-07} kg/kg (b) 45^{o},Er = 1.67×10^{-06} kg/kg (c) 30^{o}, Er = 5.3×10^{-06} kg/kg, with 60 m/s at (d) 90^{o}, Er = 3.4×10^{-06} kg/kg (e) 45^{o}, Er = 1.41×10^{-05} kg/kg (f) 30^{o}, Er = 3.36×10^{-05} kg/kg ; Symbol: Er, steady state erosion rate.

For oblique angles, clear systematic ripples are observed at all angles and velocities. The eroded areas are seen to be narrowed with reducing impact angle. This is due to the fact that the particle velocity is the highest at the centre of the particle stream and reduces gradually towards the periphery. With decreasing impact angles, the normal component of the particle stream decreases outwards from the centre. This reduces the

effectiveness of the particles away from the centre of the particle stream in material removal.

Comparing the surfaces for impact velocities of between the 30 m/s and 60 m/s, the ripples are clearly seen to have larger amplitude for higher velocity. This demonstrates that at the steady state situation, the amplitude of ripples can indicate the material removal rate specially when comparing two different wear situations.

The wear rates for respective samples are also presented in the caption of the Figures. It can be seen that the wear rate at 30^0 of impact angle is almost an order of magnitude higher than that the wear rate at 90^0 impacts. The erosion rate of aluminium shown in figure 4-10(f) is six times higher than that in Figure 4-10(c). The degree of roughness in Figure 4-10(f) appears higher than that in Figure 4-10(c).

Figure 4-11 presents the surface texture of aluminium substrates eroded by ilmenite at different particle impact velocity and angle. Clearly, the formation of ripples is the primary characteristic in these samples especially at oblique angles. The primary difference can be observed in the case of 90^o impacts, where unlike previous samples, distinct ripples did not form. This shows that the texture of the surface layer is dependent on the erodent and erosion variables at normal angle of impact.

(a) (b) (c)

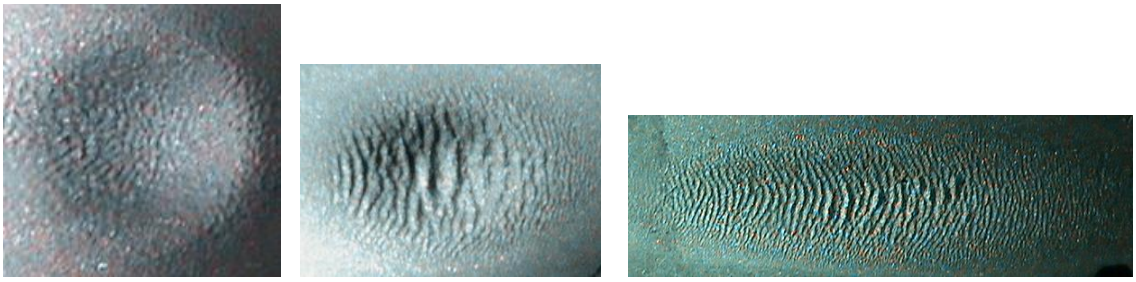

(d) (e) (f)

Figure 4-11: Surfaces of aluminium eroded by ilmenite particles with 30 m/s at (a) 90^{o} , Er=1.56 x 10^{-05} kg/kg (b) 45^{o}, Er= 2.38 x 10^{-05} kg/kg (c) 30^{o} Er=3.18 x 10^{-05} kg/kg, and at 60 m/s at (d) 90^{o}, Er=4.6 x 10^{-05} kg/kg (e) 45^{o}, Er=6.5 x 10^{-05} kg/kg; (f)30^{o} Er=1.11 x 10^{-04} kg/kg; Symbol: Er, steady state erosion rate.

In summary, the formation of ripples (Figure 4-11) is similar to that of the alumina samples which are more uniform at lower velocities compared to that at higher velocities. At higher velocity, the amplitude and frequency of the ripples appears to have increased, and there is evidence of higher material loss from the surface.

As the impact velocity of ilmenite increased from 30 m/s to 60 m/s, the steady state erosion rate was increased almost four times. Comparing Figure 4-11(a) and Figure 4-11(d), with increased impact velocity, the ripple pattern is more obvious and the roughness of the surface is shown to have increased.

4.4.2 Mild Steel Surfaces Eroded by Alumina and Ilmenite

Figure 4-12 and 4-13 presents the wear surfaces of mild steel eroded by alumina and ilmenite respectively. As seen earlier from the material loss from the surfaces, erosion of mild steel by alumina was less than the erosion rate of aluminium which is clearly supported by the visual observation of the surfaces.

In Figure 4-12, the impact area of the wear samples is clearly seen with some pitting on the surface. This is probably due to the changes in the surface layer of mild steel, as the fine alumina particles get embedded into the surface. The formation of transfer film and its effects on erosion rate of mild steel has been investigated by Cenna et al [39].

In general, formation of ripples on mild steel eroded by alumina at low velocity was not observed in these specimens. This is probably due to the different mechanism of material removal in mild steel-alumina combinations. As the particle velocity was low, particle penetration in the surface was very low and the formation of ripples is primarily due to the deformation mechanism. Moreover, particle disintegration at impact also played an important role not to generate ripples at these impact parameters and surface erodent combinations. The surface characteristics presented here are smooth with random pitting.

As the impact velocity of alumina is increased from 30 m/s to 60 m/s, the steady state erosion rate of mild steel is increased almost ten times. Both Figure 4-12(a) and Figure 4-12(d) show a smooth surface with randomly generated wear scars (pits). Comparing the surfaces at 30^0 impact angles at 30 and 60 m/s, Figure 4-12(c) and Figure 4-12(f), it is apparent that low level ripples started to appear on the surface.

(a) (b) (c)

(d) (e) (f)

Figure 4-12: Surfaces of mild steel eroded by alumina particles with 30 m/s at (a) 90^o , Er=2.8 x 10^{-07} kg/kg (b) 45^o, Er=6.02 x 10^{-07} kg/kg (c) 30^o Er=2.04 x 10^{-06} kg/kg; with 60 m/s at (d) 90^o, Er=1.6 x 10^{-06} kg/kg; (e) 45^o, Er=5.75 x 10^{-06} kg/kg (f)30^o Er=1.79 x 10^{-05} kg/kg.; Symbol: Er, steady state erosion rate.

Figure 4-13 presents the wear surfaces of mild steel eroded by ilmenite at different velocities and impact angles. Even though ripples can be seen at higher velocity, the surfaces are generally smooth at normal impacts.

At lower velocity, the particle penetration is relatively low due to the surface hardness and the rounded nature of the particle edges. This limits the particle penetration into the surface and the surface deformation. Thus mild steel presents similar surface characteristics for both ilmenite and alumina at low velocity impacts although the

surfaces clearly show higher material loss supported by the wear rates (Figure 4-12 (a)-(c) and Figures 4-13 (a)-(c)).

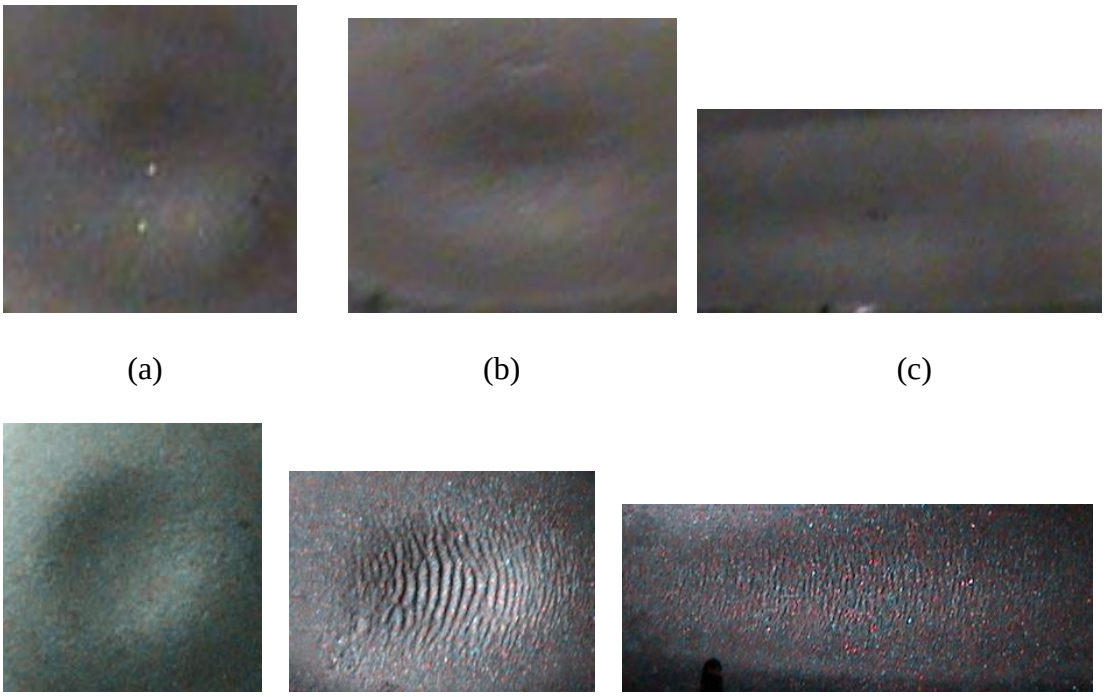

(a) (b) (c)

(d) (e) (f)

Figure 4-13: Comparison between surfaces of mild steel eroded by ilmenite particles with 30 m/s at (a) 90^o , Er=1.1 x 10^{-5} kg/kg (b) 45^o, Er= 2.64 x 10^{-5} kg/kg (c) 30^o Er=3.6 x 10^{-5} kg/kg, and with 60 m/s at (d) 90^o, Er=3.89 x 10^{-5} kg/kg; (e) 45^o, Er=6.37 x 10^{-5} kg/kg (f)30^o Er=1.08 x 10^{-04} kg/kg.; Symbol: Er, steady state erosion rate.

For higher impact velocities, depth of penetration increases due to the higher impact energy of the particle. The particle tangential component of impact energy (cutting energy) is not always enough to have a clear cut of the surface to remove material as chips. This leads to the development of ripples.

As the impact velocity of ilmenite increased from 30 m/s to 60 m/s, the steady state erosion rate of mild steel increases rapidly. The steady state erosion rate shown in Figure 4-13(f) is three times higher than that in Figure 4-13(c). Ripple is shown in Figure 4-13(f) but the eroded surface shown in Figure 4-13(c) is smooth. The higher impact velocity of ilmenite impinging on the surface of mild steel favours the formation of ripple. When comparing Figure 4-13(d), (e) & (f), denser ripples appear in Figure 4-13(e). The ripple does not appear on the surface of mild steel eroded at normal impact Figure 4-13(d). Finnie [15] showed that the ripple tends to disappear at a high impact angles. Figure 4-13(d) is in agreement with Finnie's rule possibly due to the hard surface of target material. These tests show that the surface of mild steel eroded by ilmenite favours the formation of ripple at higher velocities only.

In summary, the surfaces of ductile surface material eroded at different impact angles (30^o, 45^o, 90^o) and particle velocities (30 and 60 m/s) have been studied. The surfaces are examined here after achieving steady state erosion rates to have a better understanding of the steady state erosion mechanisms. Although the formation of ripples is a general phenomenon in material removal in ductile materials, it was demonstrated that mild steel required higher velocities to generate ripples on the surface. Ripples were formed on aluminium surfaces eroded by alumina and ilmenite whereas, in the case of mild steel, ripples were formed only with ilmenite impacted at high impact velocity and low impact angles.

Development of ripple is an important characteristic of material removal in ductile materials that can be related to material removal rate.

4.5 Analysis of Surface Micrographs of Eroded Surfaces

In the previous section, development of ripple was demonstrated for aluminium and mild steel, under typical process parameters. As a consequence of erosion process parameters and associated wear rates, ripples are generated on the wear surfaces. It has been demonstrated that the ripple formation is dependent on wear parameters as well as the particle and surface characteristics. Nevertheless, ripples can be related to the material removal rates at different wear situations.

In this section, surface topography has been analysed (using Scanning Electron Microscopy (SEM), Philips XL30 SEM & Oxford ISIS EDS) for wear mechanisms responsible for material removal in different wear situations.

Particle impact on ductile materials develops different micro-features on the surface due to the particles interactions with the surface. The common characteristics of the eroded surface are formation of chips due to micro-machining and ploughing and platelet formation due to deformation. The formation of these micro-features resulted from typical particle interaction process such as impact (low and high angle), indentation, sliding as well as combination of any of these. Spherical particles deform the surface by ploughing, displacing the material to the side and in front of the particle. For angular particle, deformation depends on the orientation of the particle as the particle rolls forward or backward during contact. Even though formation of cracks and crack propagation is not a usual mechanism of material removal in ductile materials, due to extensive surface works and surface hardening as well as the formation of a transfer film, cracks are often formed on ductile materials.

The worn surface of aluminium impacted by alumina and ilmenite are present in Figures 4-14 (a), (b), (c) and (d). Figures 4-14(a) and 4-14(c) present the impact area at low

magnification to have a general understanding of the surface features. It is well known that the material removal in normal impact happens primarily in deformation. In the case of alumina, the surface presented ripple like structures on the surface which is randomly spread around the impact zone. In the case of ilmenite, ripples are formed like rays emitting from the centre of the impact zone. This is probably due to the particle flow along the surface after the impact. The formation of ripples in these cases clearly demonstrates the higher deformation wear in ilmenite compared to alumina.

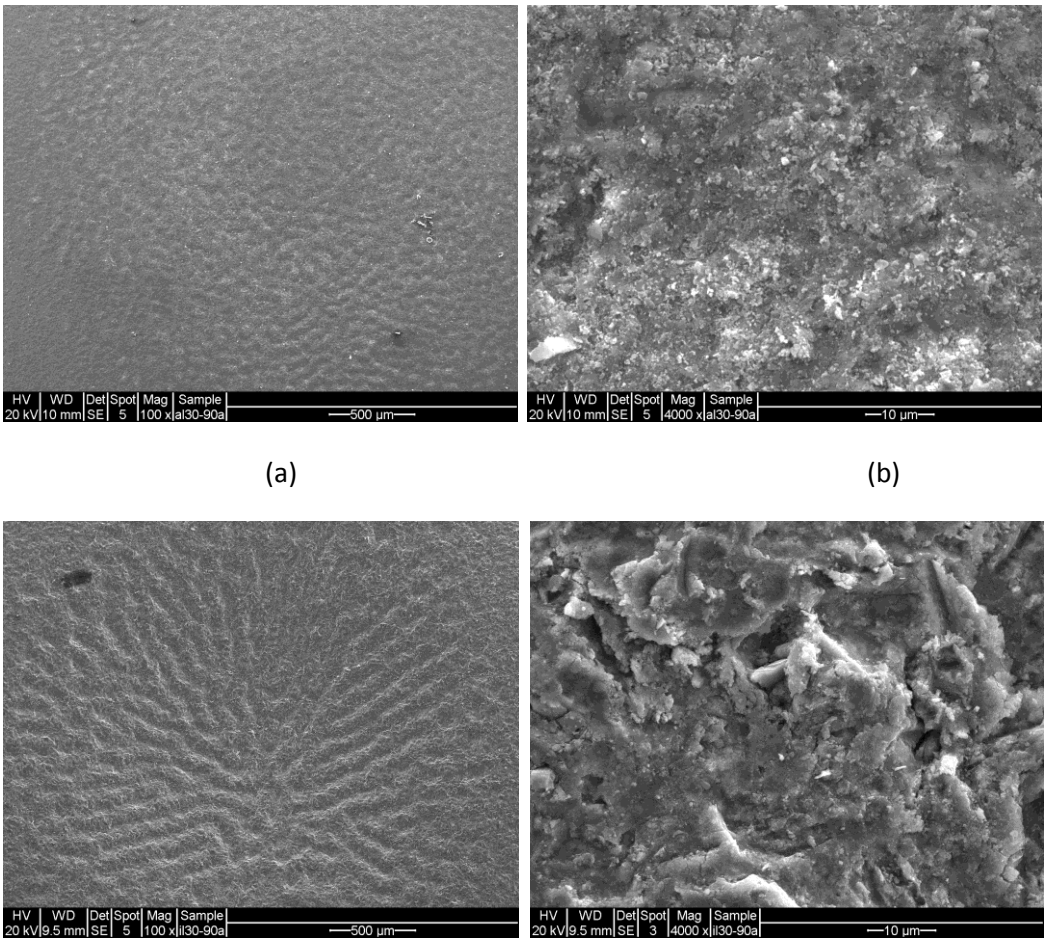

Figure 4-14: Morphology at centre of eroded surface of aluminium impinged at 90 degree by alumina at magnification of (a) x100 (b) x4000; by ilmenite at magnification of (c) x100 (d) x4000.

Figure 4-14(b) and 4-14(d) present the surface structures at higher magnification. The primary difference between these two images is the fine particles present on the surface worn by alumina compared to that worn by ilmenite. The aluminium surface worn by alumina clearly presented brittle characteristics of the wear debris present on the surface due to the particle fracture on impact that produces fine particles of alumina. These fine particles are easily embedded into the aluminium surface changing the surface characteristics from primarily ductile to brittle. Thus the surface topography for aluminium impacted by alumina presented brittle fracture of the surface.

On the other hand, the aluminium surface eroded by ilmenite clearly showed the ductile nature of the surface characterised by wear debris from the cutting and deformation processes.

The worn surface of the mild steel specimen eroded by alumina and ilmenite particles at 90^{o} impact angle with 30 m/s is shown in Fig. 4-15. Figure 4-15(a) and 4-15(c) present the general appearance of the impact zone whereas Figures 4-15(b) and 4-15(d) present the surface features in higher magnifications. Both Figures in lower magnification show a smooth appearance with relatively rougher surface for ilmenite (Figure 4-15(a) & (c)).

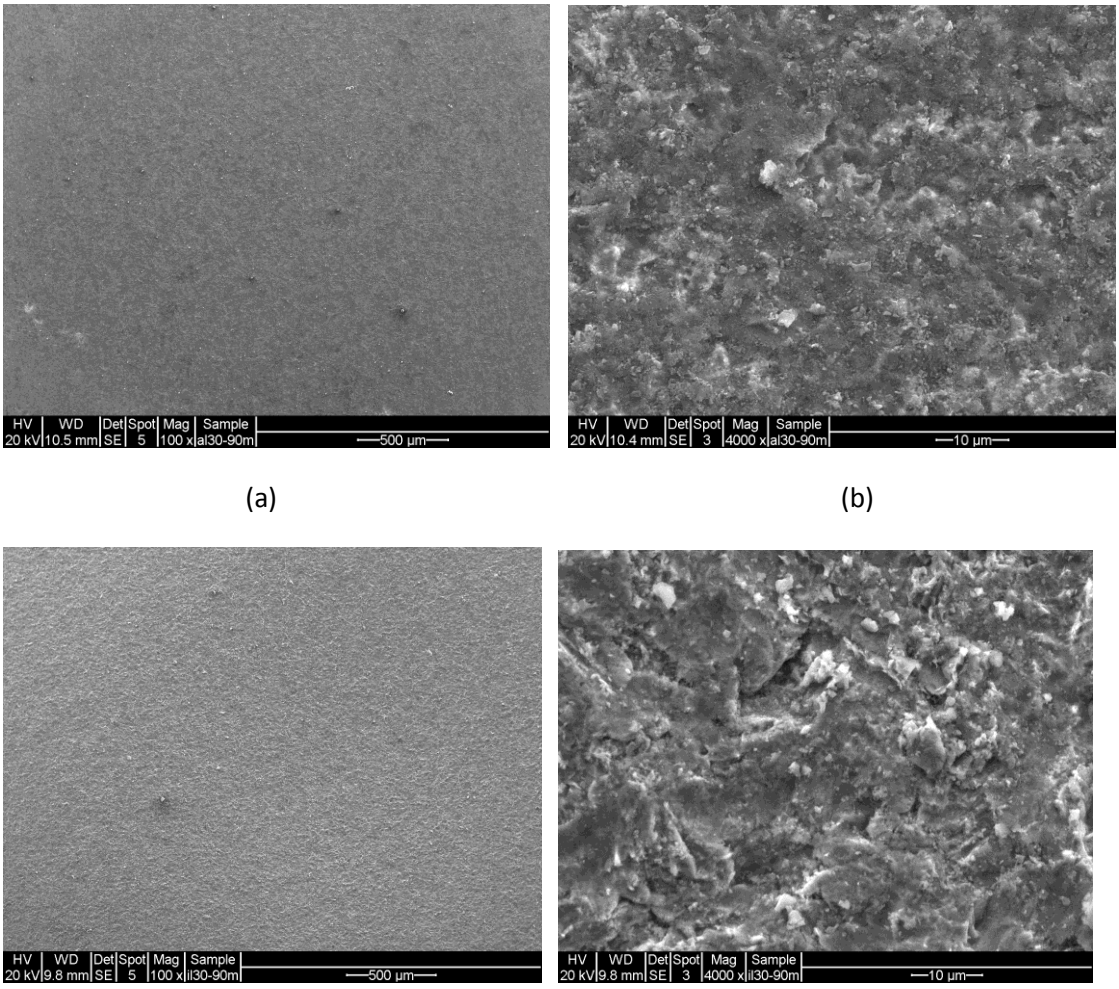

Figure 4-15: Morphology of centre of eroded surface of mild steel impinged at 90^{o};by alumina at magnification of (a) x100 (b) x4000; by ilmenite at magnification of (c) x100 (b) x4000.

Different surface textures can be seen at higher magnifications on the surfaces eroded by alumina and ilmenite (Figure 4-15(b) and 4-15(d)). Similar to aluminium, fine wear debris can be seen in the mild steel eroded by alumina but to a lesser extent. Surface flaking of the mild steel is clearly observed presenting very low levels of material removal with alumina. Random pitting of the surface was also observed, that

demonstrates the low level of fine particles embedded into the surface that usually alter the surface characteristics from ductile to brittle as seen in the case of aluminium.

Mild steel eroded by ilmenite at 90^0 is presented in Figure 4-15(d). Surface penetration ilmenite particles is much higher than that of alumina particles as they do not fracture on impact. The size of the wear debris from mild steel when eroded by ilmenite, is also larger than when eroded by alumina.

The low erosion rate at normal impact for alumina has been achieved, at least to some extent, through the changes of wear mechanisms by the embedded particles of alumina. Figure 4-15(d) is clearly rougher than Figure 4-15(b). From the wear loss of mild steel, it indicates that the development of roughness depends on mass loss of surface material as demonstrated in Figure 4-15(d). This relationship will be further explained through determination of deformation energy factor for mild steel impinged by alumina and ilmenite in Chapter 5.

The worn surface of aluminium specimens eroded by alumina and ilmenite at a 30^o impact angle is shown in Figure 4-16. Figure 4-16(a) and 4-16(c) present the general features of erosion areas whereas Figures 4-16(b) and 4-16(d) present the micrograph of worn aluminium surface at higher magnifications.

Well-developed ripples can be seen on aluminium surfaces eroded by both alumina and ilmenite. Ripples are formed on ductile materials where the primary material removal mechanism is deformation. Clearly, ripples formed with ilmenite are larger in amplitude leading to a higher material removal rate with ilmenite than with alumina.

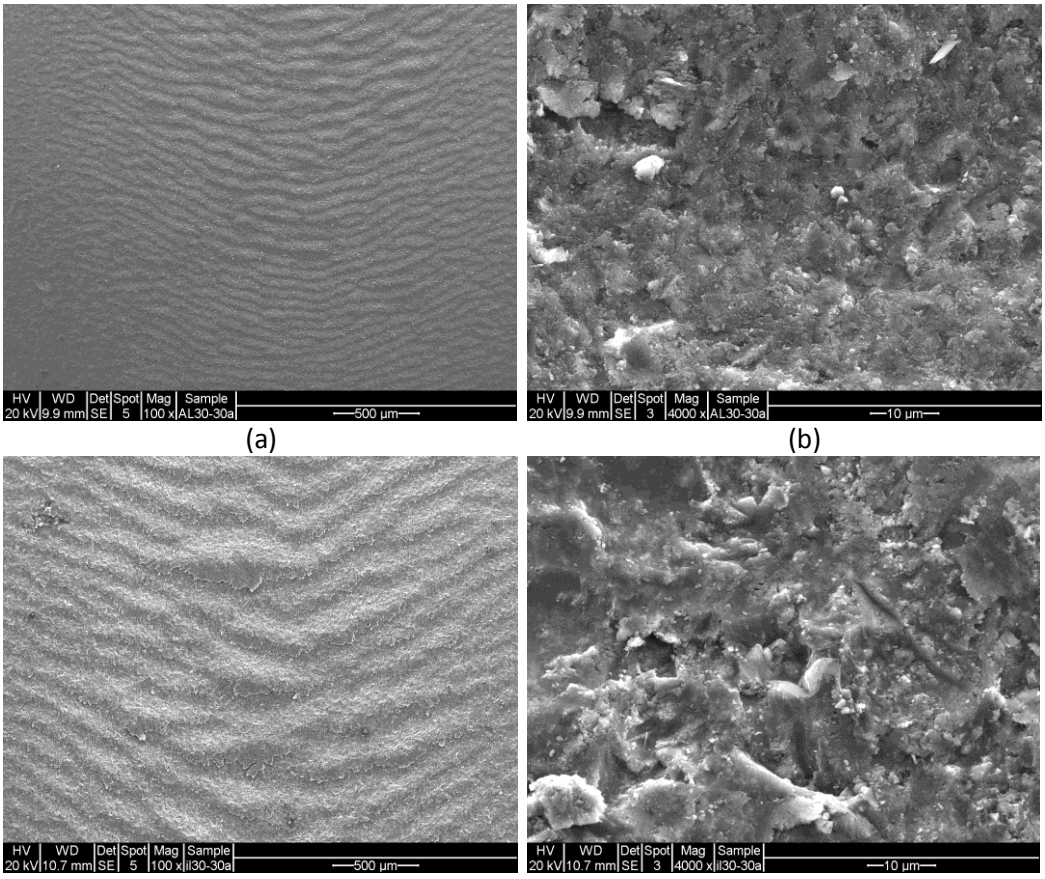

Figure 4-16: Centre Morphology of aluminium eroded surface impinged at 30^{o}; by alumina at magnification of (a) x100 (b) x4000; by ilmenite at magnification of (c) x100 (d) x4000.

The higher magnification images from the representative areas of the impact zone are presented in Figures 4-16(b) and 4-16(d). The surfaces show smoother appearance for alumina compared to that for ilmenite where higher depth of penetration is clearly visible. Figure 4-16(d) showed the cutting, deformation and platelet formation of the surface, presenting ductile characteristics of material removal in aluminium eroded by ilmenite. Aluminium surface eroded by alumina at 30^{0} showed the alumina oxide film formed on the top of the surface layer which failed subsequently in a brittle fashion as seen in Figure 4-16(b).

Figure 4-17 shows the worn surfaces of mild steel specimens eroded by alumina and ilmenite at 30^0. Macrographs of the worn surface shown in Figure 4-17 (a) & (c) showed two different textures. Ripples developed on worn surface of mild steel eroded by ilmenite (Figure 4-17(c)) whereas a smooth surface is observed (Figure 4-17(a)) on mild steel surface worn by alumina. Again, it is evident on the micrograph at higher magnification that a thin layer on the surface was affected by alumina particles (Figure 4-17(b)).

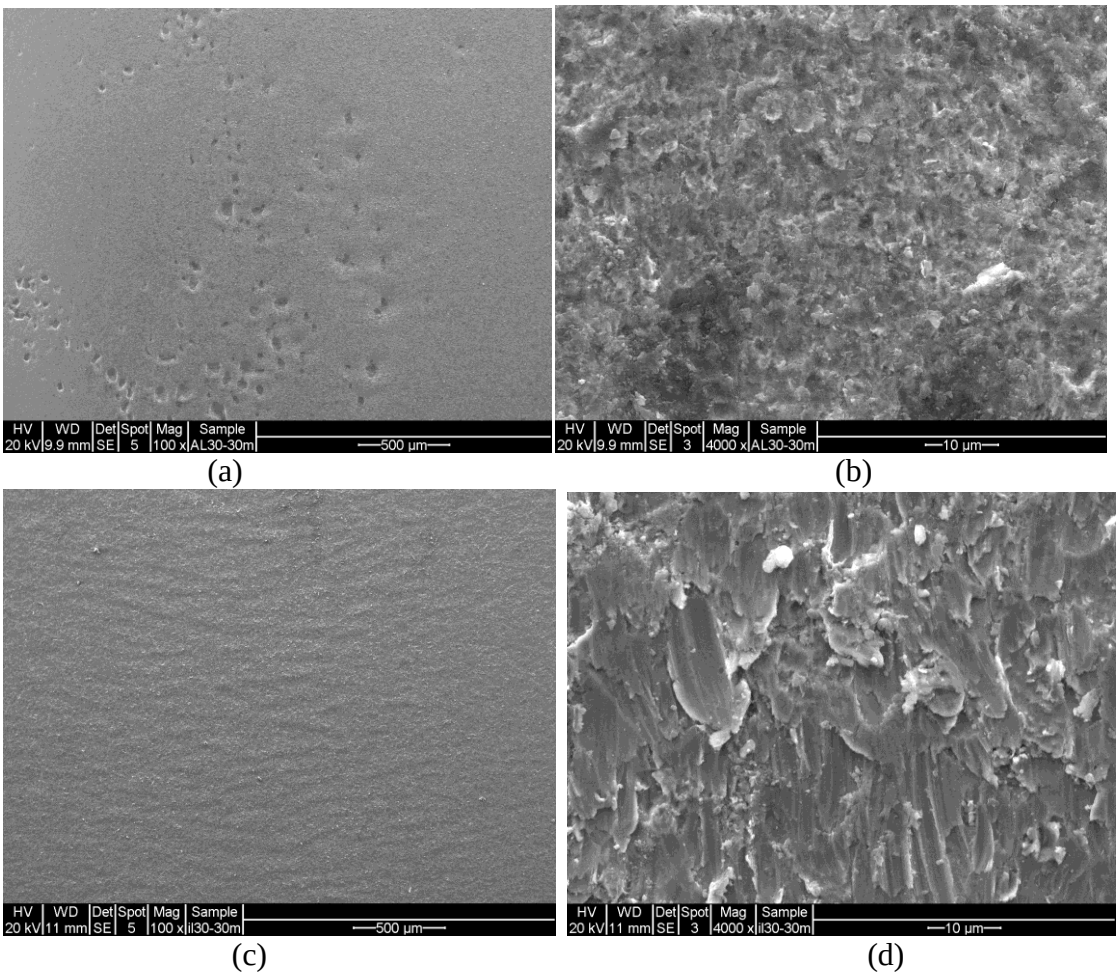

Figure 4-17: Centre Morphology of eroded mild steel surface impinged at 30^o ;by alumina at magnification of (a) x100 (b) x4000; by ilmenite at magnification of (c) x100 (d) x4000;

Mild steel surface eroded by ilmenite at 30^0 at higher magnification is presented in Figure 4-17(d). The micrograph clearly demonstrated the primary material removal mechanism is cutting in this instant. However, ploughing is also visible throughout the wear surface. From the formation of ripples observed at lower magnification (Figure 4-17(c)), it is evident that the deformation mechanism plays a lesser role in material removal compared to cutting for this combination of material and impact parameters.

Figure 4-14 and 4-15 showed the worn surfaces of aluminium and mild steel eroded by alumina and ilmenite at normal impact. Comparing surface features of aluminium and mild steel, worn surfaces of aluminium showed higher surface damage than that of mild steel. This is expected as this high hardness mild steel can resist the impact damage better than softer alumina. Comparing the surfaces eroded by alumina and ilmenite, lower surface damage was observed for alumina due mainly to two reasons; 1) alumina particles tend to fracture or disintegrate on impact and 2) the fine particle embedded into the surface generates a transfer film that tends to protect the surface. On the other hand, ilmenite being angular in general transfers energy to the surface more efficiently and hence higher surface damage has been observed.

In summary, the above micrographs show two aspect of surface material response. First, the absorbed impact energy transferring to a useful material removal mechanism depends on hardness of the surface, impact angle and penetration of the particle. Secondly, aluminium and mild steel show the typical behaviour of ductile damage.

The surface micrographs are further analysed for specific characteristics of material removal mechanism in ductile materials. The micro-machining process shown in Figure 4-18 demonstrates type I & type II cutting illustrated by Hutchings [4]. Formation of

large flake shows that type II cutting to removes material efficiently. The accumulated plastic deformation at the rim and lips show type I cutting process, with wear debris produced from plastic rupture after experiencing a low-cycle fatigue process.

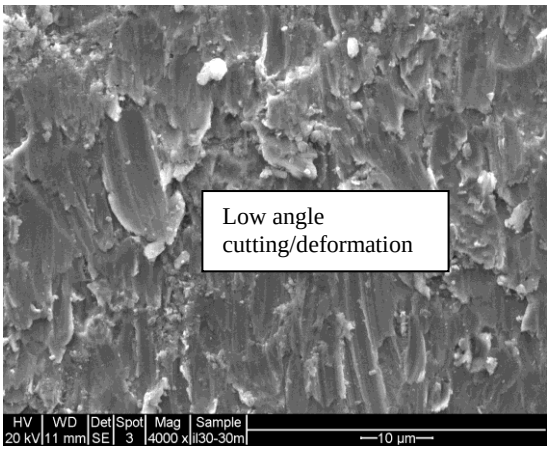

Figure 4-18: Material removal mechanisms in ductile materials in oblique angle (30^0 cutting angle, 30 m/s on mild steel, ilmenite particle flow from top to bottom).

The micro-machining is one of the dominant material removal mechanisms demonstrated by ilmenite on ductile surfaces at oblique impacts. It was also found that the impact velocity of ilmenite increases the efficiency of the wear mechanism.

Figure 4-19 shows the surface of aluminium and mild steel impacted by ilmenite at an impact angle of 30^0. Figure 4-19(a) shows the eroded surface of aluminium impinged by ilmenite and Figure 4-19(b) shows the eroded surface of mild steel impinged by ilmenite at an angle of 30^o with impact velocity of 30 m/s. As discussed before, the ilmenite particles do not disintegrate at impact as demonstrated by the wear surfaces free of debris from erodent particles. The surface of aluminium and mild steel in Figure 4-19 shows the highest erosion at 30^o described in previous sections.

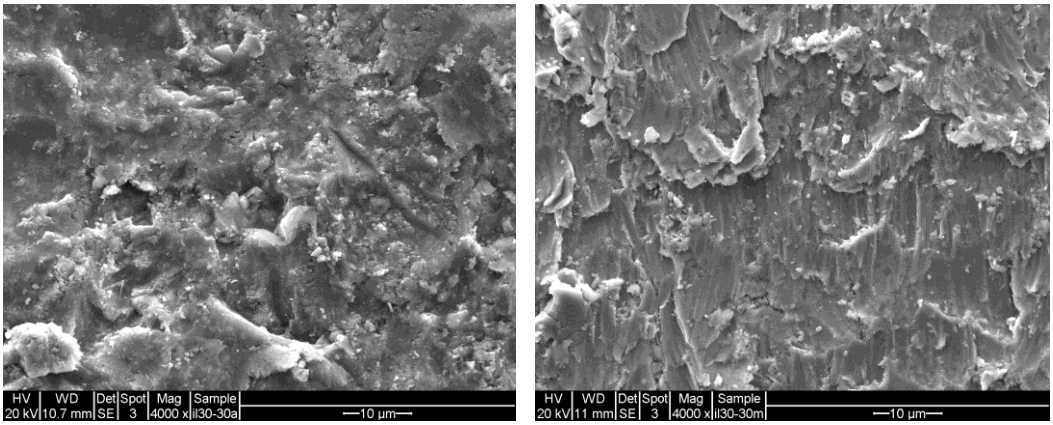

(a) (b)

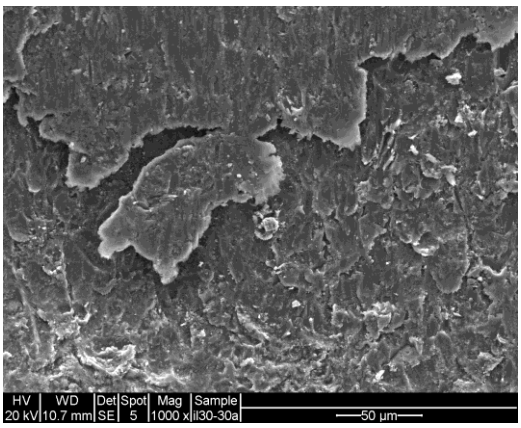

(c)

Figure 4-19: Aluminium and mild steel surfaces eroded by ilmenite at oblique angle with magnification of (a) aluminium surface x4000 (b) mild steel surface at x4000 (c) aluminium surface at x1000

The Figure 4-19(c) shows the peak area of a ripple developed on the eroded surface of the aluminium. Although cutting is the dominating material removal mechanism at oblique angles for ductile materials, extensive deformation occurs on the wear surface that effectively develops the ripples. As seen in Figure 4-19(c), a thin layer of material is being pushed over the surface, the area underneath the sliding layer remains unworn, effectively developing a peak. The area in the valley zone is effectively the high wear

area. As the cutting continues, the waveform moves forward effectively generation a new peak and valley.

Figure 4-19(b) presented the mild steel surface eroded by ilmenite under similar impact conditions. As discussed earlier, the level of ripple formation in mild steel was low. This is due to the fact that the cutting remained the dominant wear mechanism with lower level contribution from deformation. The thin layer of material sliding over the surface can be seen in the mild steel as well, although very low compared to that of aluminium.

Comparing the eroded surface of mild steel with aluminium shown in Figure 4-19, it is obvious that the eroded surface of mild steel is smoother than that of aluminium and there is less plastic deformation. This is due to its low erosion resulting from its hard surface layer and its characteristic plastic flow pressure. The surface characteristics clearly consistent with the mass loss of mild steel compared to aluminium. The plastic deformation caused by impacting particles clearly indicates that the material hardness is one of the dominant parameter to control the wear of material.

Different surface characteristics have been observed for the surfaces worn by alumina. A high level of fine wear debris was present due to the particle fracture and disintegration of agglomerates of the fine particles of alumina. In many cases the surface appearance was more brittle in nature than ductile. This is consistent with the fact that alumina particles become embedded into the surface and develop a surface film which shows different surface characteristics than the parent material [39]. Figure 4-20 presented the aluminium and mild steel surfaces eroded by alumina at normal incident. Both the surfaces present a scale like structure which seems to be brittle in nature.

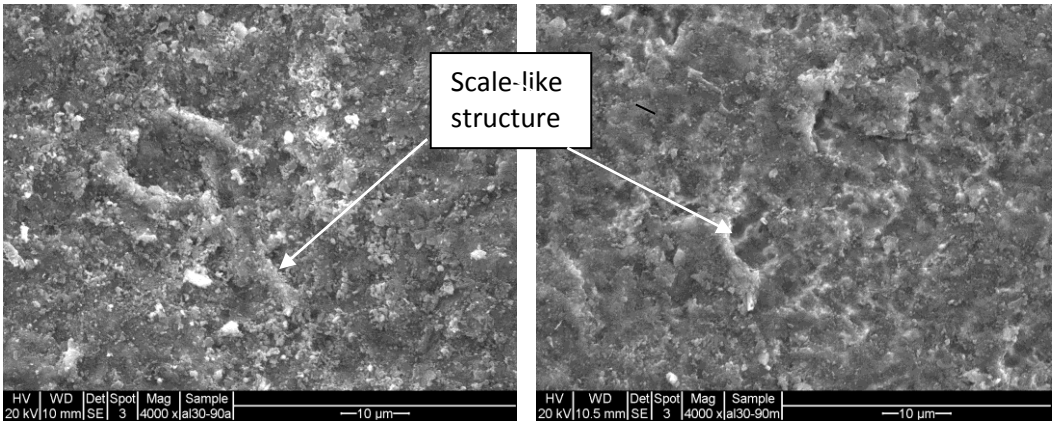

(a) (b)

Figure 4-20: (a) Eroded surface of aluminium impacted by alumina at an angle of 90^o with an impact velocity of 30 m/s. (b) Eroded surface of mild steel impacted by alumina at an angle of 90^o with impact velocity of 30 m/s.

The generation of transfer a film on alumina conveying mild steel pipelines is believed to be responsible for high wear in critical areas of pipeline. This was also recognised by Cenna et al. [39]. These transfer films are removed through delamination from the surface and removed through formation of a network of cracks. The scale-like structure seen on these wear surfaces are not well developed, but consistent with brittle fracture of the small areas of the surface creating craters as seen in Figure 4-20. The impacting small angular particles produce indentation and possibly enhance the micro cracking and chipping for removing material. The sensitivity of the erosion rate depends on the rate of wear debris to remove.

A two-stage erosion mechanism may occur due to the impacting alumina on the ductile surface. In stage one; particles are embedded into the surface during the incubation period changing the surface characteristics. And in stage two, the surface is damaged in

brittle fashion and material removed as fine particles as opposed to formation of chips as expected for ductile materials.

Levy [9] showed that, in the presence of alumina, scales effectively increase as the surface temperature reaches about 150^{o}C. The typical wear loss is increases as a function of metal thickness loss. Levy also showed that there is transition behaviour of thickness loss rate, from low to high metal loss rate as the impact velocity increases beyond about 30 m/s.

Another distinct surface characteristics was observed in aluminium and mild steel eroded by ilmenite at normal impacts. Figure 4-21 presents the SEM micrograph of mild steel and alumina surfaces eroded by ilmenite. Figure 4-21(a) illustrates the eroded surface of alumina and Figure 4-21(b) shows the eroded surface of mild steel eroded by ilmenite at 90^{o} with impact velocity of 30 m/s.

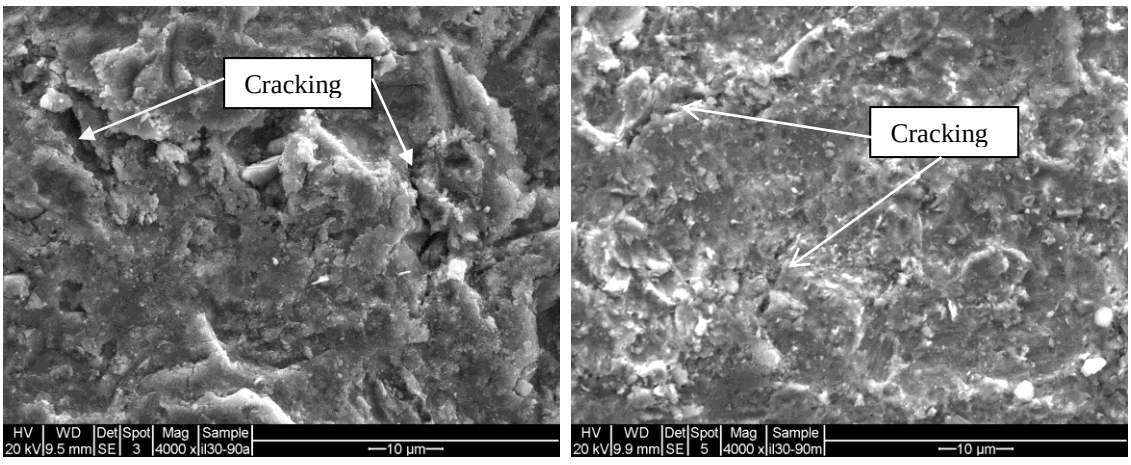

(a) (b)

Figure 4-21: SEM images of eroded surface impacted by ilmenite at normal incidence and 30 m/s particle velocity (a) aluminium (b) mild steel.

Although cutting and ploughing deformation mechanisms are obviously seen on the surface as expected, cracking on the surface is equally visible. Unlike surfaces eroded by alumina, no fine particle can be seen on the surface. Wear particles seen on the surface are of the substrate itself. It is believed that the surface cracking in these areas is primarily due to the work hardening of the surface layer. Although the cracks are seen to be developed perpendicular to the surface extending into the material, it is believed that they do not form crack-networks to remove material as layers, as seen in the case of surfaces worn by alumina (Figure 4-20).

Figure 4-21(b) showed the similar mechanism of crack formation in mild steel eroded by ilmenite at 90^0 impacts. The surface of mild steel appears smoother due to low level of plastic deformation due to higher hardness. Cracks similar to those in aluminium are also seen in mild steel surface but they appear smaller compared to that of aluminium. Although the cracking is a brittle characteristic of the surface, the dominant wear mechanism remains cutting and deformation as presented by other surface features such as the wear debris as well as cutting and deformation through ploughing. Small cracks developed during impact process but do not have any substantial effect on material removal rate.

The impingement of ilmenite on mild steel and aluminium may induce subsurface deformation, crack nucleation and propagation and finally delamination wear. The mechanisms of material removal were then flaking involving sliding, abrasive and adhesive wear.

In summary, it is shown that the impingement of ilmenite on ductile material surfaces may cause brittle fracture together with ductile behaviour. Material removal from the surface occurs through ductile mechanisms without significant impact on wear rates due to the formation of cracks on the surface. From the analysis of wear mechanisms of aluminium and mild steel, it was demonstrated that the wear mechanism of mild steel and aluminium remains the same for the same erodent whereas, wear mechanism for different erodents can be substantially different.

4.6 Conclusion

A series of erosion experiments were designed for measuring the mass loss of target material and observation of morphology of the eroded surface. The mass losses of the target materials under the influence of different low impact velocity of solid particles (alumina, ilmenite) have been discussed. The micrographs of ductile surfaces have been examined and analysed for associated wear mechanisms. The resulting material removal mechanisms are also discussed.

Furthermore, the steady state erosion rates have been compared for erosion performance of different surface materials. In order to understand the effects of particle impact energy on wear rates as well as wear mechanisms, the cutting and deformation energy factors will be determined and analysed in the following chapter.

Chapter 5

ENERGY FACTOR

5.1 Introduction

Energy factors have been defined in Chapter 2 in the context of the development of a predictive model for wear of materials. In Chapter 4 wear rates of two ductile materials eroded by alumina and ilmenite were determined experimentally and the wear surface were analysed for dominant wear mechanisms responsible for material removal in particular wear environments. In this chapter, the energy factors are determined from the experimental results for different solid particle and substrate combinations.

The aim of this chapter is to understand the relationship between energy factors and wear mechanisms for different surface-particle combinations. The energy factors vary with particle impact angle for a given impact velocity, but they can be considered as a material property [5] within a range of particle velocities and hence can be considered as a wear coefficient of a target material for modelling of wear.

5.2 Energy Factors

Predictive models for the wear of materials have been discussed in detail in Chapter 2. The model based on particle impact energy developed by Neilson et. al. [5] has the potential for application in real life wear situation if the energy factors are known correctly.

Based on the understanding of the material removal processes in erosion, Neilson et. al. [5] suggested a wear model to evaluate the material loss based on the material and impact parameters. They considered the cutting wear factor ϕ (kinetic energy needed to release a unit mass of material from the surface through cutting) and deformation wear factor ε (kinetic energy needed to release a unit mass of material from the surface through deformation) as wear properties in a specific wear condition and expressed the erosive wear loss based on these wear properties and their associated process parameters as shown below:

$$W = \underbrace{\frac{\frac{1}{2}M(V^2\cos^2\alpha - v_p)}{\phi}}_{(A)} + \underbrace{\frac{\frac{1}{2}M(V\sin\alpha - K)^2}{\varepsilon}}_{(B)} \quad for \ \alpha < \alpha_0 \tag{5-1}$$

$$W = \underbrace{\frac{\frac{1}{2}MV^2\cos^2\alpha}{\phi}}_{(C)} + \underbrace{\frac{\frac{1}{2}M(V\sin\alpha - K)^2}{\varepsilon}}_{(B)} \quad for \ \alpha > \alpha_0 \tag{5-2}$$

where W is the erosion value, M is the mass of particles impacting at angle α with velocity V. K is the vertical component of velocity below which no erosion takes place and v_p is the residual parallel component of particle velocity as solid particle leaves the impact area. Part B accounts for deformation wear and part A and C account for cutting wear at low angles and large angles of impact respectively. α_0 is the angle at which the v_p is zero so that at this angle both the equations will predict the same erosion.

The major emphasis in these models is the energy factors that determine the material loss in cutting and deformation processes. In such material removal processes, researchers [3, 6, 23 and 40] studied the development process of craters and concluded

that the material removal can be characterized based on critical impact velocity and the ratio of hardness of material to hardness of impacting particle. They showed that the penetration depth is dependent on the particle impact velocity. The volume of material removal is proportional to the absorbed kinetic energy of the impacting solid particles. From these studies, it can be clearly stated that the impact energy of the particle is an important erosion parameter affecting the erosion rate of target material.

Neilson et. al. [5] derived an analytical method from works of Finnie [23] and Bitter [7] for evaluating erosion at different impact angles. According to this method, at normal impacts, the material removal is only by the deformation mechanism. For oblique impacts, material removal occurs due to the superposition of deformation and cutting mechanisms. Based on this understanding they proposed the simple steps listed below to determine the deformation and cutting energy factors using the steady state wear rate determined in previous chapter.

1. Using the mass loss of material per unit mass of particle, obtained at α = 90^0, ε can be determined from the equation $\frac{W_{90^o}}{M} = \frac{\frac{1}{2}V^2}{\varepsilon}$
2. Using ε, the contribution of deformation wear to the total wear at all angles can be obtained from equation (5-1) and (5-2)
3. The cutting wear can be obtained at all angles by subtracting the deformation wear from the experimental values.
4. Using the cutting wear value obtained at (3), the cutting wear factor can be determined from $\frac{W}{M} = \frac{\frac{1}{2}V^2\cos^2\alpha}{\phi}$.

As the cutting and deformation mechanism are the primary mechanisms in wear of ductile materials, these two factors can determine the wear loss in any wear situations, provided that the particle impact energy delivered to the surface is determined correctly. Erosion parameters that affect the absorption of impact energy onto the surface are particle velocity, particle angularity and the energy absorption capacity of the solid surface [13].

5.3 Calculation of Energy Factor for Aluminum and Mild Steel

Analysis of wear rates and the surface response of aluminium and mild steel eroded by alumina or ilmenite have been presented in Chapter 4. In this chapter the wear rates are further analysed based on particle kinetic energy dissipated on the surface. As mentioned earlier, the energy required to remove unit mass of material from the surface through deformation is termed the unit energy of deformation or deformation energy factor. Similarly, the energy required to remove unit mass of material from the surface through cutting is termed the unit energy of cutting or cutting energy factor.

Using the determined wear rates and steps described in section 5.2, the unit energy of deformation and cutting are determined. The relationship between dissipated energy and wear rate in a worn ductile surface are studied in this chapter.

5.3.1 Deformation Energy Factor

The determination of steady state erosion rate has already been presented in the previous chapter. The steady state erosion rate at normal impact is used to determine the deformation energy factor.

The deformation energy factor at a fixed range of velocities represents the resisting force against particles and can be used as a wear coefficient for comparing erosion resistance of different materials. The velocity dependency of deformation energy factor is presented in the sections below.

Figure 5-1 presents the deformation wear factors of aluminium and mild steel eroded by alumina and ilmenite. The Figures clearly showing that the energy factors are higher for alumina compared to that for ilmenite. In Figure 5-1(a), the ratio of the two factors vary between 25 at lower velocity and 15 at higher velocity. This shows that the absorbed energy of alumina for aluminium is at least 15 times lower than that of ilmenite in the range of velocities considered. In figure 5-1(b), the ratio of two factors vary between 40 at 30 m/s and about 25 at 60 m/s. This demonstrates the absorbed energy of alumina is at least 25 times lower than that of ilmenite. Mild steel requires twice the impact energy than that of aluminium for removal of a unit mass of surface material.

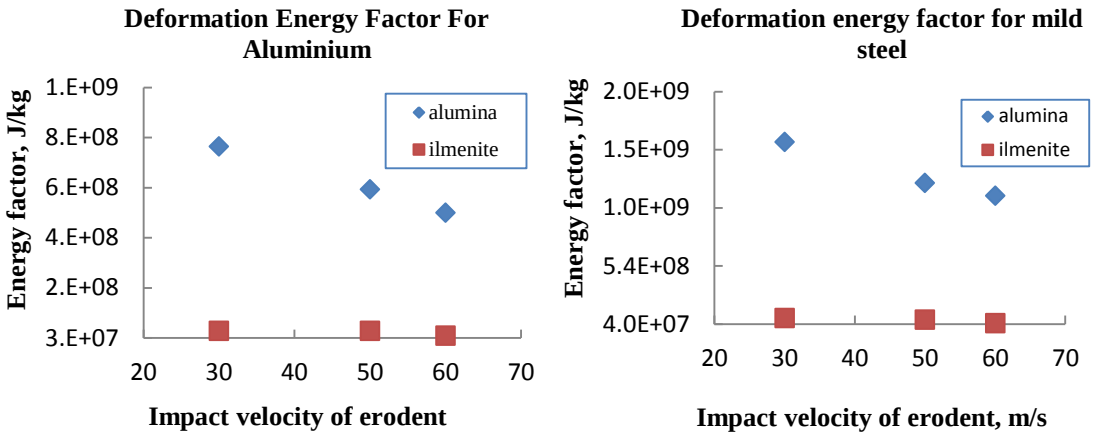

Figure 5-1: Deformation energy factor for (a) aluminium (b) mild steel

In Figure 5-1(a) and (b), the deformation energy factor for aluminum and mild steel shows a decreasing trend with impact velocity for alumina which means less energy was required for removal of the same amount of material from the surface. This is understandable considering the proportion of energy spent in elastic and plastic deformation. With increasing particle velocity, the proportion of energy spent in plastic deformation increases as the energy required for elastic deformation remains constant.

Aluminium possesses a lower deformation energy factor than that of mild steel indicating a higher proportion of absorbed energy dissipating in the form of brittle fracture leading to produce wear debris.

5.3.2 Cutting Energy Factor

The cutting energy factor describes the energy required to remove a unit amount of material in cutting action primarily at oblique angles. Figure 5-2 presents the cutting energy factors for aluminum and mild steel eroded by alumina and ilmenite particles. Figure 5-2(a) presents the cutting energy factors for aluminum and Figure 5-2(b) presents the cutting energy factor for mild steel. In the Figures, similar to the deformation energy factor, the cutting energy factor also decreases with increasing particle velocity. The difference of cutting energy factors for different impact angles reduces with increasing impact velocity for both mild steel and aluminum. Cutting energy factors at 45^0 impacts are 2 to 3 times higher than that of 30^0 impacts for 30 m/s particle velocity. The cutting energy factor for aluminum and mild steel eroded by alumina is more than double compared to that for ilmenite due to the efficiency of micro-machining of ilmenite as described in chapter 4.

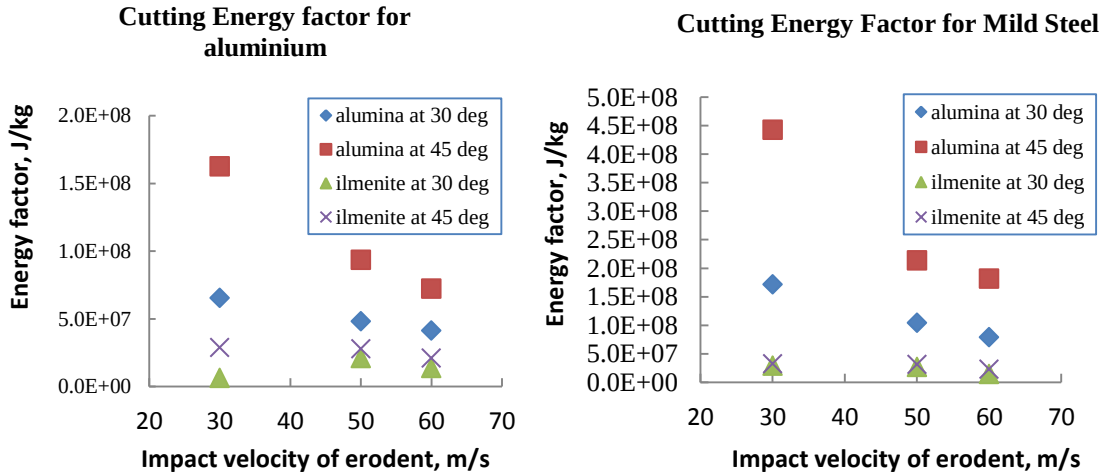

Figure 5-2: Cutting energy factor at different velocity for (a) aluminium and (b) mild steel.

Figure 5-1 and 5-2 show the trends in deformation and cutting energy factor as a function of impact velocity of alumina and ilmenite respectively. The deformation and cutting energy factor rapidly decreases as the impacted alumina velocity increases from 30 m/s to 60 m/s. This shows the increasing efficiency of material removal by alumina at higher impact velocity. For normal impacts, alumina generates a transfer film on the surface which reduces the material removal (discussed in chapter 4) and in effect increases the energy needed to remove a unit mass of material from the surface.

5.4 Effect of Impact Angle on Energy Factors

The effect of impact velocity on determining energy factor of ductile surface was discussed in the previous sections. The effect of impact angle on deformation and cutting energy factor of a ductile surface is described in this section. The cutting energy factors for aluminium and mild steel as a function of impacted angle is presented in this section.

Figure 5-3 & 5-4 shows the cutting energy factor curve for aluminium and mild steel as a function of impact angle of erodent. In general, the cutting energy factor for aluminium and mild steel increases rapidly as the impact angle of alumina increases from 30^{o} to 90^{o}. This indicates more energy required for material removal.

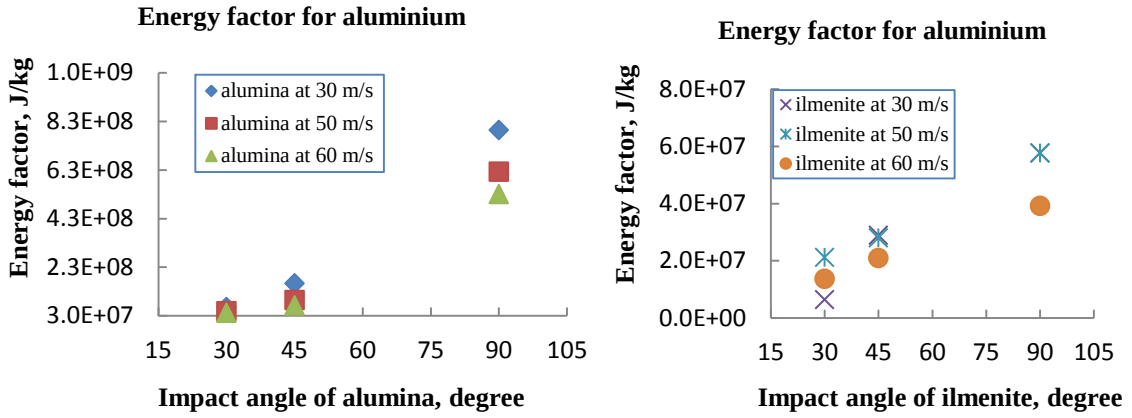

(a) (b)

Figure 5-3: Energy absorption of aluminium due to different impact angle of (a) alumina (b) ilmenite.

In Figure 5-3(a) & 5-4(a), the harder and angular alumina shows low efficiency in the cutting process at higher impact angle, demonstrated by its higher cutting energy factor. This shows that cutting is more efficient at low angle of impacts.

Energy factors for ilmenite were compared with alumina under the similar impact conditions on aluminium in Figure 5-3(a) and 5-3(b). The energy factors for ilmenite were lower than for alumina showing the energy transfer to the surface was more efficient. This is primarily due to the particle disintegration effect of alumina at impact. Ilmenite cuts into the surface easier than alumina due to the particle shape as well.

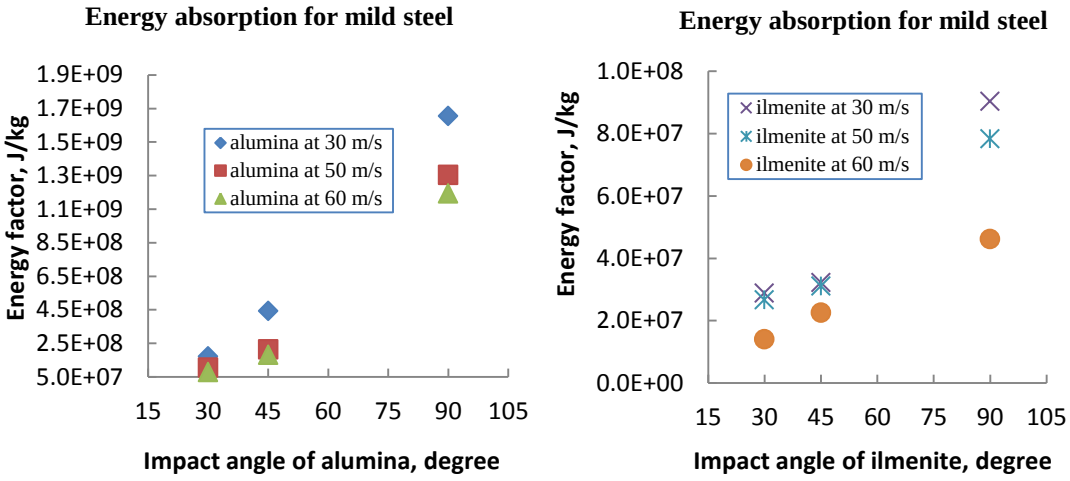

Figure 5-4: Energy absorption of mild steel due to different impact angle of (a) alumina (b) ilmenite.

The results show that the effect of impact angle on the cutting energy factor is not linear. The energy factors at 90^0, the deformation energy factor, are also shown in the Figures. The deformation energy factors are almost 1-2 orders of magnitude higher than that of the cutting energy factors. This is due to the fact that, for ductile materials, material removal in deformation needs multiple impacts to remove material from the surface whereas for oblique angles, material can be removed by single impact as well as the lips and ploughed material that can be removed in subsequent impacts very easily.

As shown through the micrographs in previous section, ripple formation on the surface is a result of the material removal process that contains cutting and deformation, shallow angle impact in fact is an efficient method of material removal for ductile materials.

5.5 Calculation of Steady State Erosion Rate

The steady state erosion rates are calculated using the energy factors determined experimentally as described in previous sections. In practice, the cutting energy factor for maximum wear is required to determine steady state erosion rate for application in wear models. This is generally defined by this angle for maximum erosion.

Figure 5-5 shows the calculated steady state erosion rate curves for aluminium and mild steel impinged by alumina. Figure 5-6 shows the calculated steady state erosion rate curves for aluminium and mild steel impinged by ilmenite. The steady state erosion rate curves were calculated from the cutting energy factors of 30^o and 45^o shown in previous sections.

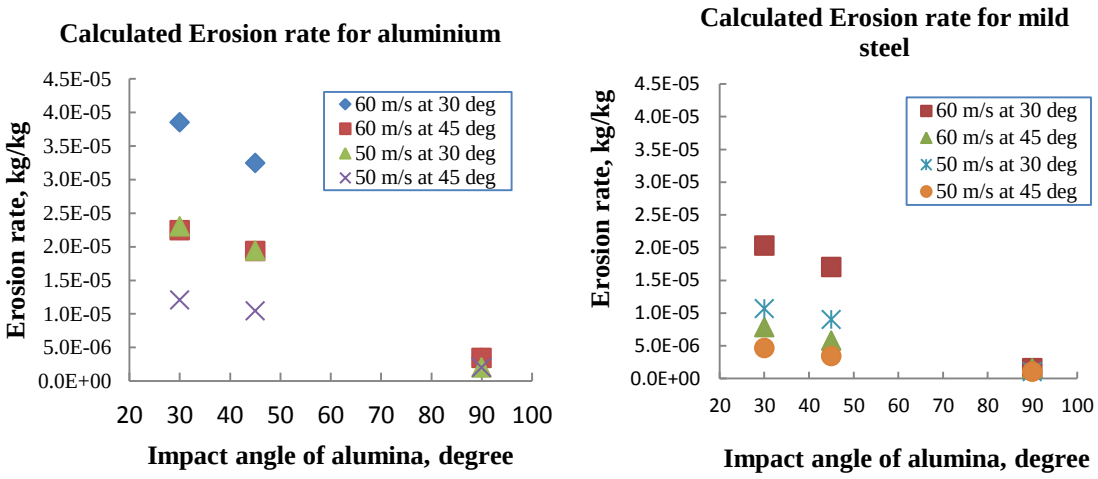

(a) (b)

Figure 5-5: Steady erosion rate was calculated from determined energy factor above for (a) aluminium (b) mild steel. The Legend shows cutting energy factor for impact velocity and angle.

Figure 5-5 shows two different steady state erosion rates. Each Figure calculated by cutting energy factor determined at 30^o and 45^o for impact velocities, 50 m/s and 60

m/s. It was found that the divergence for mild steel in Figure 5-5(b) is less than that of aluminium shown in Figure 5-5(a). This is probably due to the fact that mild steel surface absorb more energy at this angle of impact.

In Figure 5-6, the steady state erosion rate curves of aluminium and mild steel eroded by ilmenite was calculated by cutting energy factor determined at 30^{o} and 45^{o} for ilmenite impact velocities, 50 m/s and 60 m/s. It shows the similar divergence for aluminium and mild steel.

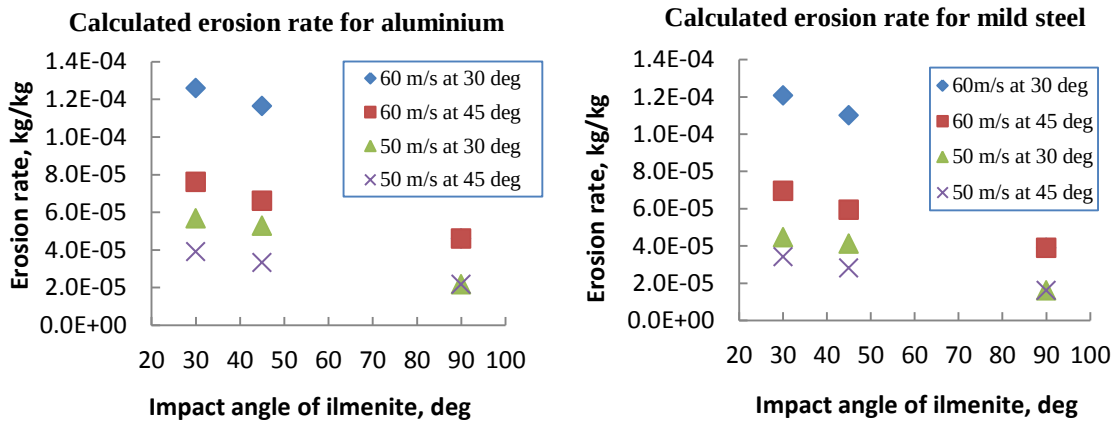

Figure 5-6: Calculated erosion rate at different angles for (a) aluminium (b) mild steel. The Legend shows cutting energy factor for impact velocity and angle.

5.6 Methods for Determination of Cutting Energy Factor for Wear Models

The steady state erosion rate curves as a function of impact angle (Figure 5-7 to 5-8) were calculated using the mean value between cutting energy factor of 30^{o} and 45^{o}. Thus, the steady state erosion rate curve was located between these two curves was

discussed in previous section. Figure 5-7 shows the steady state erosion rate of mild steel and aluminium at 60 m/s and 50 m/s respectively.

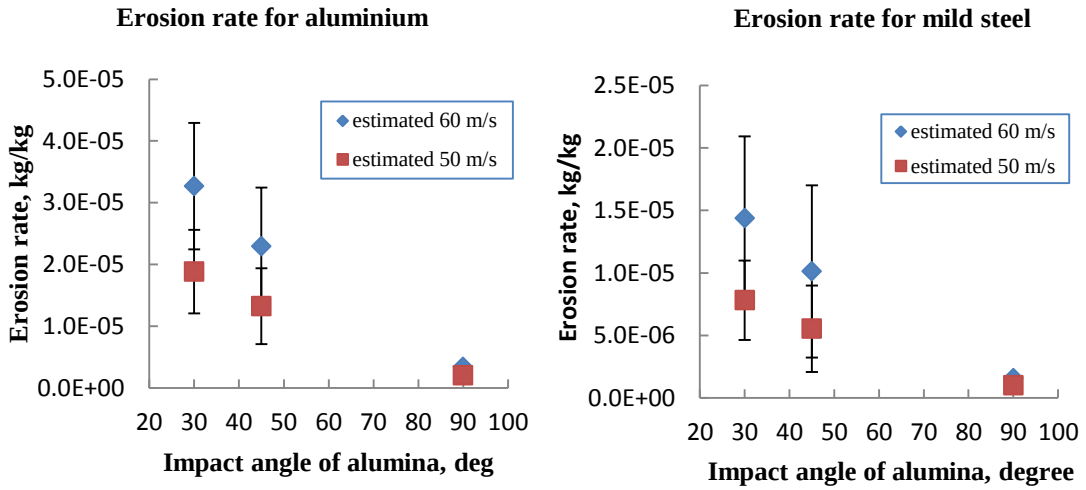

(a) (b)

Figure 5-7: Determined erosion rate from estimated energy factor for (a) aluminium (b) mild steel after eroded by alumina.

Figure 5-8 shows the steady state erosion rate was calculated by the average energy factor described earlier for aluminium and mild steel impinged by ilmenite. The tolerance of aluminium and mild steel impacted by ilmenite at 60 m/s is higher than that for 50 m/s.

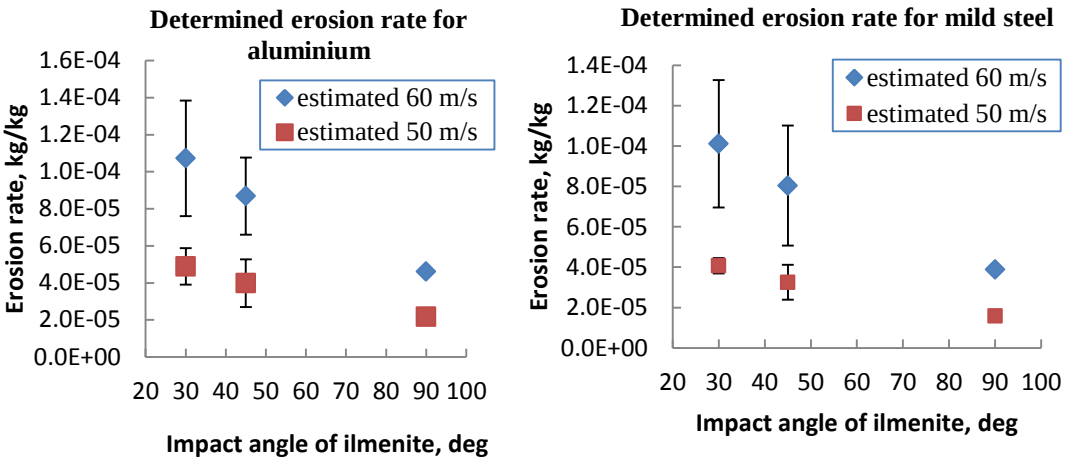

(a) (b)

Figure 5-8: Determined erosion rate from estimated energy factor for (a) aluminium (b) mild steel eroded by ilmenite.

In summary, Figure 5-7 showed steady state erosion rate curves with error bars which show the tolerance of calculated steady state erosion rate for alumina. Also, figure 5-8 showed that the tolerance in wear rates due to the impact velocity of ilmenite.

5.7 Application of the Energy Factors in Predictive Models

Pneumatic conveying tests have been conducted in the laboratory for the application of the energy factors in a predictive wear model for wear of pipelines. The energy factors determined in this study have been used in this modelling. Gradual thickness losses of the pipeline have been measured using an ultrasonic thickness gage. The thickness gage can measure a thickness at 0.01mm accuracy. For the convenience of the conveying process, the particles have been separated from the air flow and recirculated in to the process. Although the particles have been degraded due to recirculation, it was not

practical to use single pass conveying tests. The degradation of the particles has been reflected on the measured thickness loss data when compared with the model output discussed later.

Figure 5-9 [39] presents a comparison of experimentally measured thickness loss data and the thickness loss from the predictive model. It can be seen from Figure 5-9(a), the rate of thickness loss has been gradually increased towards the later part of the test. The trend of thickness loss rate is expected as discussed in the earlier paragraphs. With increasing loss of material, the surface profile changes which favours increasing energy dissipation to the surface. With increasing energy dissipated to surface increases the material loss through cutting and deformation is increased.

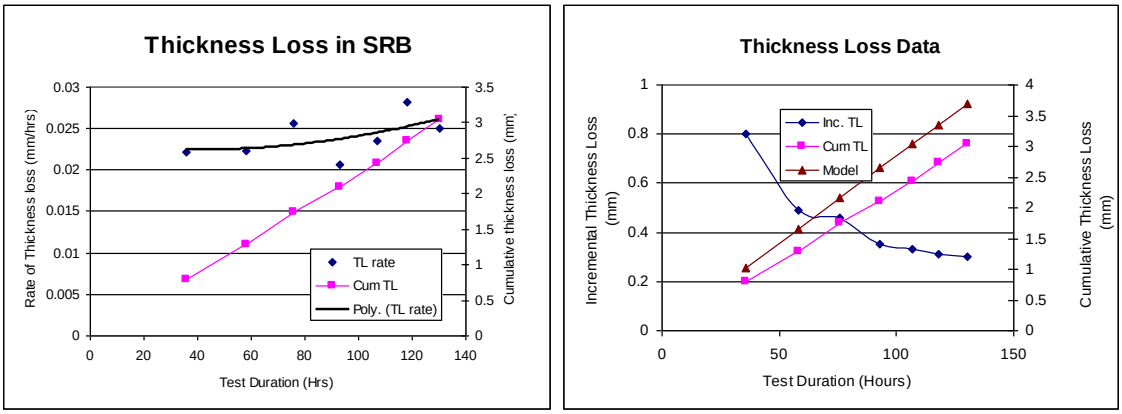

Figure: 5-9: (a) Rate of thickness loss and cumulative thickness loss from the bend wear (b) Incremental thickness loss and cumulative thickness loss from the bend compared with model output.

Incremental and cumulative thickness loss from the critical wear area of the short radius bend is presented in Figure 5-9(b). It also showed the model output for the cumulative

thickness loss for the similar pipeline configurations and conveying parameters. The model output graph has a similar trend as the experimental wear loss. But the model output consistently overestimated the actual measurement of the thickness loss. This can be explained considering the conveying of the sand and the measurement of the energy factors.

The energy factors were measured using the single pass of the particles. That provided the maximum abrasivity of the particles in determining the energy factors. In fact, that is the case for pneumatic conveying in industry. For the conveying tests in the laboratory, it was not practical to use single pass tests for these conveying. Instead, particles have been recycled for several hours. Although the particles have been degraded due to the recycling, we have monitored the particle degradation through particle size distribution tests for uniformity. Due to the degradation of the conveying materials, lower wear rates were expected compared to the model output.

The application of the energy factors in the predictive model clearly demonstrated the benefit of such a modelling approach and determining the energy factors for specific application of the wear of materials. It also demonstrated the importance of the surface-erodent combination in determining these factors.

5.8 Processes in Erosion Energy Factor

Even though there have been many attempts to strengthen the erosion resistance of different materials, energy factors are not popular parameters for evaluating erosion resistance. Unlike erosion rate which is a direct measure of the overall effect of the wear process, energy factors indicate the mechanical processes that take place during the

surface-particle interaction process. This includes specific well defined material removal processes from the surface during wear process.

The processes described by energy factors measure the effects of interaction of impacting solid particles and the surface material. Because of the large number of factors that affect the material removal process, the energy factors are capable of accounting for the effects of surface, erodent and impact factors accurately. The aim of this section is to describe some of the processes described by the energy factor during particle contact with the surface through the deformation and cutting process, for better understanding of the dissipation of impact energy.

5.8.1 Erosive Energy of Particle

Although there is a huge body of work involving wear rate and materials behaviour at different wear environments there is very limited published work incorporating different energy factors with wear rates and environments. From the published data in the literature, it is possible to determine the associated energy factors for different surface-erodent combination (shown in Figures 5-10 to 5-11). The energy factors determined for mild steel and aluminium in the current experimental program are also included in the Figures for comparison.

Figure 5-10 presents the deformation energy factors for aluminium and mild steel eroded by different erodent at different impact velocities. Although it is not possible to extract all the information about the wear environment, the comparison of deformation energy factors for aluminium and mild steel demonstrated that the energy factors may vary almost an order of magnitude depending on different factors. Particle size does not

seem to have any systematic effect on the deformation energy factors. Although the deformation energy factors were expected to reduce considerably with increasing velocity, as presented by Neilson et. al. [5], it was not evident from these data.

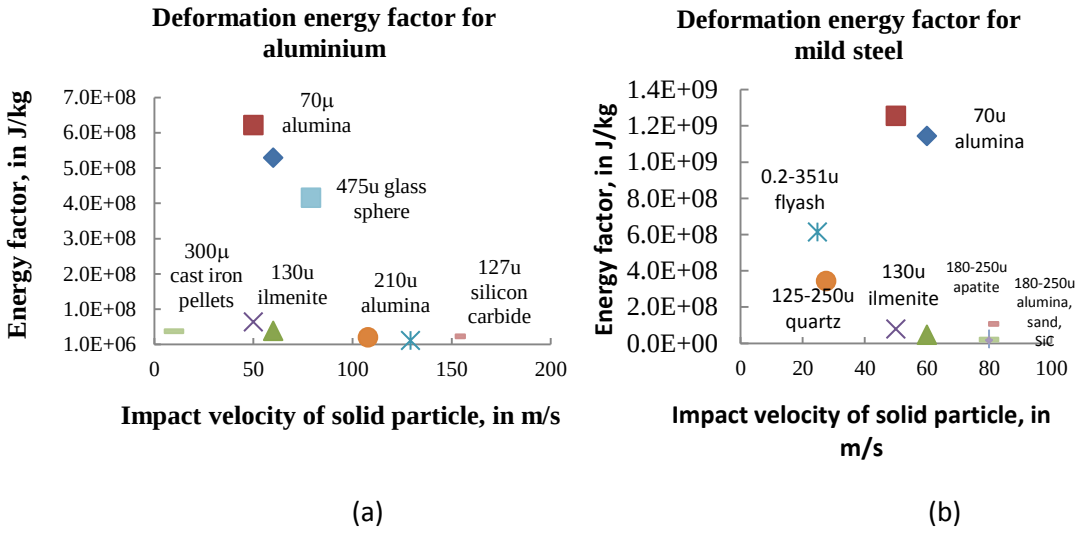

Figure 5-10: Deformation energy factor for different particles and size from literature data [5, 7, 22, 23] and present experimental data. (a) of aluminium, and b) mild steel.

Figure 5-11 shows the distribution of cutting energy factors at 30^0 impacts for aluminum and mild steel for different impact velocities. Cutting energy factors for aluminum showed a narrow band, demonstrating that the variation of cutting energy factor is small compared to the deformation energy factors, except for alumina and glass sphere eroded at around 50 m/s. Again, similar to that for deformation energy factors, the variation of the cutting energy factors with impact velocity was very small.

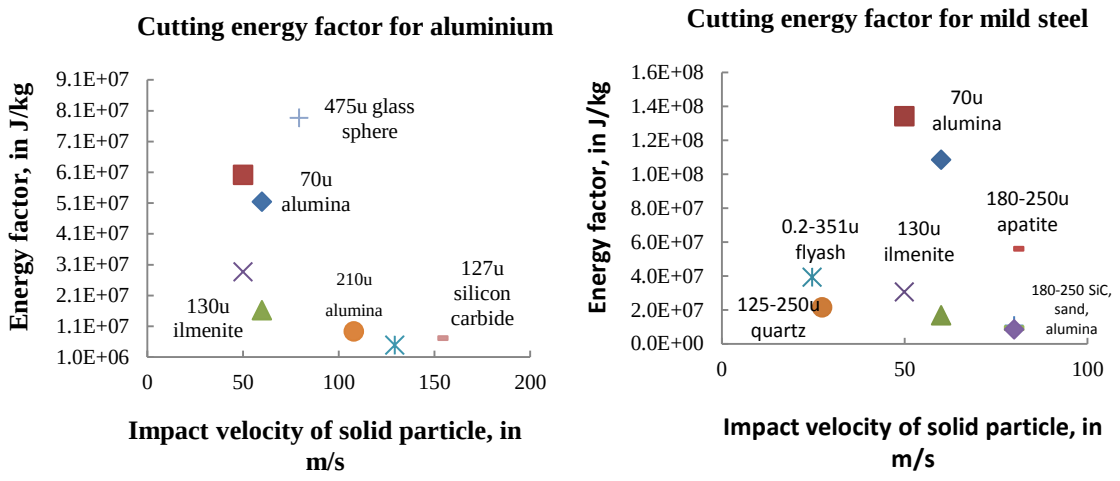

(a) (b)

Figure 5-11: Cutting energy factor of 30 degree for (a) aluminium [4, 6] (b) mild steel [4, 6, 22, 23]

Similar to that of aluminum, the cutting energy factors for mild steel also presented very small variation with increasing particle velocity. Alumina showed the energy factor at 50 m/s is almost an order of magnitude higher compared to other particles.

Although the results gathered from the literature did not show the expected variation of energy factors with increasing particle velocity, the effect of particle velocity is a major factor as seen in the current study. The compilation also did not show a major sensitivity to the particle size.

Considering the limitations of a small number of studies in the literature, it is still encouraging to see that the energy factors can describe the combined effects of surface, erodent and impact factors for predictive models.

5.9 Conclusion

The main purpose in this study is to provide a generic method for evaluating wear in ductile materials based on profound scientific methodologies. Energy based models have been developed over the last fifty years based on the understanding of the particle interaction with the surface and material removal process. The energy factors described in the models have been applied based on the laboratory erosion results as well.

Wear in pneumatic conveying is a well-known issue that reduces the service life of the conveying pipeline. It is also known to the stakeholders that the wear in pipeline is primarily erosion type wear, recently recognised as a combination of abrasive wear superimposed by erosive wear which makes the modelling more complex.

In this study, the energy factors for a combination of two ductile surfaces and two erodent particles have been determined experimentally. Wear tests in pneumatic conveying was conducted in the laboratory to measure the wear loss and compared the measured loss with the output of the model based on the energy factors determined experimentally. The application experimental results showed excellent agreement with the model output based on empirical parameter of energy factor.

Energy factors collated from the literature showed universality of the energy factors to describe the cutting and deformation mechanisms as surface property only.

Chapter 6

CONCLUSION AND FUTURE WORK

6.1 Conclusion

The overall objective of this thesis was to understand the relationship between wear rates and wear mechanisms in ductile material using available information from the literature together with solid particle erosion experimental results from the current experimental program.

The analysis in chapter 2 provided a good description of ductile materials behaviour under variety of erosive wear conditions. Development of models for predicting wear rates in different wear conditions leads to the understanding that uniform criteria can describe various factors affecting wear in erosion. Understanding complex superposition of the deformation and cutting mechanisms revealed that the energy factors associated with these mechanisms can predict the wear rates in specific wear situations provided that these factors are known and thus became the central issue of this study.

Commercial grade of aluminium and mild steel have been wear tested using alumina and ilmenite. Both the surface materials are ductile and the erodent is hard and angular. Using standard procedures, wear rates for different impact angles and particle velocities were determined. Following the procedure from the literature, the energy factors were determined for the surface materials at different wear parameters. Comparison between the data obtained from the literature and the calculated values have also been presented.

Finally the determined energy factors have been applied into the predictive model for prediction of thickness loss in a pneumatic conveying pipeline.

The major achievements made in this study are summarized below:

1. The surface feature and erosive wear properties of aluminium and mild steel under the impingement of alumina or ilmenite were studied in order to establish the relationship between the wear mechanisms and wear rate. It was found that the wear rate and roughness of eroded surface is reflected in the severity of wear. The literature data has been used to support and explain the argument.

2. The determination of the energy factor for any wear situation requires understanding of the complex relationship of the constitutive energy equation. Once the energy factors are determined, the models can describe the wear situations based on the factors affecting the wear rates.

3. The measured erosion rate always underestimated the corresponding theoretically determined erosion rates based on the impact parameters and energy factors determined. Part of this difference might be attributed to the fact that during the wear studies, the particles were recirculated and energy factors determined using single pass of particles. Due to recirculation of particles, particle attrition occurred as well as blunted corners reduced the wear rate.

4. The performance particle characteristics showed that particle integrity plays a crucial role in determining the material removal mechanism. Particle fracture at impact reduces the particle's capacity to damage the surface and hence lower wear rates were obtained for alumina compared to ilmenite.

6.2 The Future Work

The performance of surface materials in specific wear conditions particularly with particle velocity and impact angles have been addressed in this thesis. A more general solution providing useful information for wear prediction of components, such as pneumatic pipeline bends, require further analysis of the effects of the particular wear parameter and micro-analysis of the surface features. Such an extension is possible if the erosion tests can be conducted with a larger variety of erodent and surface materials. The erosion conditions are likely to control erosion performance of surface materials. This erosion response permits us to determine the energy factors relating the variations with specific wear parameters.

The development of this approach requires the following additional work:

(1) Perform an erosion experiment using different particle flux suitably selected to represent industrial environmental conditions of interest.

(2) Select the range of particle and surface materials based on the industrial applications.

(3) Conduct experimental investigations using the particle velocities that can represent the range required of industrial applications.

4) Determine the energy factors and develop a constitutive relationship of the energy factors.

The database of energy factors can provide essential elements of the predictive wear model for any industry concerned with the wear of materials.

Reference

[1] A. Cenna, N. Page, K. Williams, W. McBride, S. Keys, S. Rajagopalan, J. Wang, D. Wu ,"Experimental test program for the validation of wear model", Prediction of material removal rate from the conveying pipeline and optimization of process parameters for maximum plant life, Cooperative Research Centre for Integrated Engineering Asset Management (CIEAM), 2006, pp. 107.

[2] I. M. Hutchings, "Wear by particulates." Chemical Engineering Science, 42 (1987), 869-878.

[3] Ambrish Misra and Iain Fnnie, "on the size effect in abrasive and erosive wear", wear 65 (1981) 359 – 373.

[4] I. M. Hutchings, "Deformation of metal surfaces by the oblique impact of square plates", Int. J. mech. Sci., 19 (1976), 45-52.

[5] J. H. Neilson, A. Gilchrist, "Erosion by a stream of solid particles", wear 11 (1968), 111-122.

[6] D. Mills and J.S. Mason, "Particle size effects in bend erosion", *Wear, 44*(1977), 311-328.

[7] Bitter, J.G.A. , "A study of erosion phenomena part I & part II ", wear , 6(1963), 5-21, 169-190.

[8] Ambrish Misra and Iain Finnie, "on the size effect in abrasive and erosive wear", wear 65 (1981) 359 – 373

[9] A. Levy, "Chapter 2 Mechanism of erosion", Solid Particle Erosion and Erosion-Corrosion of Materials, 1995, ASM International, ISBN: 0-87170-519-2, pp. 11-33.

[10] O.P. Modi,"Two-body abrasion of a cast Al-Cu (2014 Al) alloy-Al_2O_3 particle composite: influence of heat treatment and abrasion test parameters", wear 248 (2001) 100-111.

[11] E. Rabinowicz, L.A. Dunn and P.G. Russell, "A study of abrasive wear under three body conditions", wear 4(1961), 345-355.

[12] Liang Fang, Weimin Liu, Daoshan Du, Xiaofeng Zhang, Qunji Xue,"Predicting three-body abrasive wear using Monte Carlo methods", wear 256 (2004) 685-694.

[13] Y.I. Oka, T. Yoshida, "Practical estimation of erosion damage caused by solid particle impact Part 2: Mechanical properties of materials directly associated with erosion damage", wear 259 (2005), 102-109.

[14] Vispi Homi Bulsara, Srinivasan Chandrasekar and Thomas N. Farris, "Sliding Indentation Fracture of Brittle Materials", ASM Handbooks Online, vol 8, Scratch Testing, Sliding Indentation Fracutre.

[15] I. Finnie, Y.H. Kabil," On the formation of surface ripples during erosion", wear 8 (1965), 60-69.

[16] J.E. Talia, Y.A. Ballout, R.O. Scatergood, "Erosion ripple formation mechanism in aluminium and aluminium alloys", wear, 196 (1996), 285-294.

[17] M. Liebhard and A. Levy, "The effect of erodent particle characteristics on the erosion of metals", wear 151,(1991), 381-390.

[18] G.B. Stachowiak, G.W. Stachowiak, "The effects of particle characteristics on three-body abrasive wear", wear 294 (2001) 201-207.

[19] C.T. Morrison and R. O. Scattergood, "Erosion of 304 stainless steel", wear, 111 (1986) 1-13.

[20] Tilly, G. P., & Sage, W. ,"The interaction of particle and material behaviour in erosion processes. *Wear, 16*(1970), 447-465.
[21] G.P. Tilly, "Erosion caused by airborne particles", wear 14 (1969) 63-79.
[22] A. V. Levy and P. Chik ,"The effects of erodent composition and shape on the erosion of steel", wear (1983), 151-162.
[23] I. Finnie, "Erosion of surface by solid particles", wear, 3(1960), 87-103.
[24] P.H. Shipway, I.M. Hutchings, "Influence of nozzle roughness on conditions in a gas-blast erosion rig.", wear 162-164 (1993), 148-158.
[25] P.H. Shipway, I.M. Hutchings,"A method of optimizing the particle flux in erosion testing with a gas-blast apparatus", wear 174 (1994), 169-175.
[26] D.G. Rickerby, N.H. Macmillan,"The erosion of aluminum by solid particle impingement at normal incidence", wear 60 (1979), 369-382.
[27] P.S. Follansbee, G.B. Sinclair and J.C. Williams, "Modelling of low velocity particulate erosion in ductile materials by spherical particles", wear 74 (1981 – 1982) 107 – 122.
[28] S.K. Hovis, "Erosion mechanisms in aluminium and Al-Si alloys", wear 107 (1986) 175-181.
[29] K. Anand, S. K. Hovis, H. Conrad, "Flux effects in solid particle erosion", wear 118 (1987) 243 – 257.
[30] D.G. Rickerby, N.H. Macmillan,"The erosion of aluminum by solid particle impingement at oblique incidence", wear 79 (1982), 171-190.
[31] L. K. Ives and A. W. Ruff, "Transmission and scanning electron microscopy studies of deformation at erosion impact sites", wear 46 (1978) 149-162.
[32] A. Levy, "The platelet mechanism of erosion of ductile metals", wear, 108 (1986) 1 – 21.
[33] T. H. Kosel and K. Anand, "An optoelectronic erodent particle velocimeter", in V. Srinivasan and K. Vedula (eds.), Corrosion and Particle Erosion at High Temperature, The Minerals, Metals and Materials Society, 1989, pp. 349-368.
[34] T. Deng, M.S. Bingley, M.S.A. Bradley, "The influence of particle rotation on the solid particle erosion rate of metals", wear 256 (2004) 1037-1049.
[35] I. Kleis, I. Hussainova, "Investigation of particle – wall impact process", wear 233-235 (1999), pp. 168-173.
[36] A. W. Ruff, L. K. Ives, "Measurement of solid particle velocity in erosive wear", wear 35 (1975), 195-199.
[37] ASM handbooks Online.
[38] Ballout, Y. A., Mathis, J. A., & Talia, J. E. , "Effect of particle tangential velocity on erosion ripple formation. *Wear, 184*(1995), 17-21.
[39] Cenna, A. A., Williams, K. C., Jones, M. G., & Page, N. W. , "Generation of transfer film and its effects on wear mechanisms in alumina conveying pipeline of mild steel. *Wear, 267*(2009), 362-367.
[40] K. Adachi, I.M. Hutchings, "Wear-mode mapping for the micro-scale abrasion test", wear, 255 (2003), 23-29.